Theses and Dissertations   Student Graduate Works

9-2004

Electrostatic Radio Frequency (RF) Microelectromechanical Systems (MEMS) Switches With Metal Alloy Electric Contacts

Ronald A. Coutu Jr.

Follow this and additional works at: https://scholar.afit.edu/etd

Part of the Electrical and Electronics Commons, and the Electro-Mechanical Systems Commons

ELECTROSTATIC RADIO FREQUENCY (RF) MICROELECTROMECHANICAL SYSTEMS (MEMS) SWITCHES WITH METAL ALLOY ELECTRIC CONTACTS

DISSERTATION
Ronald A. Coutu, Jr., Major, USAF

AFIT/DS/ENG/04-05

DEPARTMENT OF THE AIR FORCE
AIR UNIVERSITY

AIR FORCE INSTITUTE OF TECHNOLOGY

Wright-Patterson Air Force Base, Ohio

AFIT/DS/ENG/04-05

ELECTROSTATIC RADIO FREQUENCY (RF) MICROELECTROMECHANICAL SYSTEMS (MEMS) SWITCHES WITH METAL ALLOY ELECTRIC CONTACTS

DISSERTATION

Presented to the Faculty of the

Graduate School of Engineering and Management

Air Force Institute of Technology

Air University

Air Education and Training Command

In Partial Fulfillment of the

Requirements for the Degree of

Doctor of Philosophy

Ronald A. Coutu, Jr., B.S.E.E., M.S.E.E., P.E.
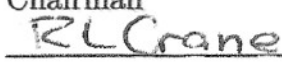
Major, USAF

September 2004
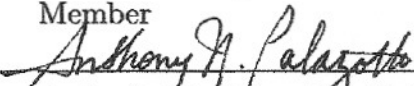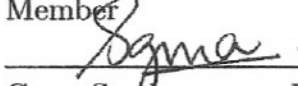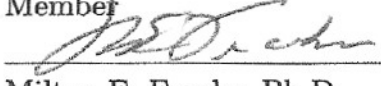
ELECTROSTATIC RADIO FREQUENCY (RF)

MICROELECTROMECHANICAL SYSTEMS (MEMS) SWITCHES

WITH METAL ALLOY ELECTRIC CONTACTS

Ronald A. Coutu, Jr., B.S.E.E., M.S.E.E., P.E.

Major, USAF

Approved:

_____   25 AUG 04
Captain Paul E. Kladitis, Ph.D.   Date
Chairman

R L Crane   20 AUG 04
Robert L. Crane, Ph.D.   Date
Member

_____   19 AUG 04
Kevin D. Leedy, Ph.D.   Date
Member

Anthony N. Palazotto   20 Aug 04
Anthony N. Palazotto, Ph.D., P.E.   Date
Member

_____   20 Aug 04
Guna Seetharaman, Ph.D.   Date
Member

_____   25 Aug 04
Milton E. Franke, Ph.D.   Date
Dean's Representative

Accepted:

_____
Robert A. Calico, Jr., Ph.D.
Dean, Graduate School of Engineering and Management

For Major Aaron C. "C-dot" George, Mr. Charles Clark, Mr. David "Laze" Lazeron, and Major Bill Wood, Ph.D.

Acknowledgements

I have many people to thank. First, a special thank you to my wife for letting me go back to school (again!) and my two boys for their constant encouragement and support during this program. Next, I thank the "Air Force" for selecting me for this wonderful opportunity, especially Howie Lewis (Col, USAF, Ret.), Col Bob Arbach, and Col Tom Buter, Ph.D., for their permission, encouragement, and guidance while applying for the Doctoral program.

Many thanks to my research committee for guiding me through the AFIT Ph.D. process, especially my sponsor, Dr. Bob Crane, for supporting all my endeavors. I also owe a debt of gratitude to Bill Cowan (Lt Col, USAF, Ret.) for his great advice on selecting committee members and also for supporting my research during his tenure as the AFRL/SND MEMS Team Leader.

In addition, I thank Capt Vern Starman, Ph.D., Dr. Rob Reid, Mr. Rick Webster, Mr. Bill Trop, Dr. Jeff Zabinski, Dr. Steve Patton, Dr. Steve Smallwood, Dr. Jose Nain, Mr. Chris Ryan, Mr. Ben Phillips, Dr. Rick Strawser, Dr. Becky Cortez, Dr. Jack Ebel, Mr. Steve Dooley, Dr. Shankar Mall, Dr. Hyukjae "Jay" Lee, Ms. LaVonne Allen, Ms. Mary Jane McCormick, Ms. Mary Susan Wellbaum, and my AFIT student friends. Thanks guys.

Thanks to Mrs. S.L.B Tow, my editor friend, Mr. Bernie Beveridge, my high school electronics teacher, and Mr. Andy Fingado, my Marine Corps buddy, each of whom graciously accepted my request to proof read the final draft of this document. And, as always, thanks Mom and Dad for teaching me the necessary ingredients for success: (1) a solid work ethic, (2) the drive for achievement, and (3) to always finish what you've started. Finally, I thank God for the grace to continue my journey.

Ronald A. Coutu, Jr.

Table of Contents

List of Figures

x

List of Tables

List of Symbols

List of Abbreviations

AFIT/DS/ENG/04-05

Abstract

Radio frequency (RF) microelectromechanical systems (MEMS) switches are paramount in importance for improving current and enabling future USAF RF systems. Electrostatic micro-switches are ideal for RF applications because of their superior performance and low power consumption. The primary failure mechanisms for micro-switches with gold contacts are becoming stuck closed and increased contact resistance with increasing switch cycles.

This dissertation reports on the design, fabrication, and testing of micro-switches with sputtered bi-metallic (i.e., gold (Au)-on-Au-(6.3at%)platinum (Pt)), binary alloy (i.e., Au-(3.7at%)palladium (Pd) and Au-(6.3at%)Pt), and ternary alloy (i.e., Au-(5at%)Pt-(0.5at%)copper (Cu)) contact metals. Performance was evaluated, in-part, using measured contact resistance and lifetime results. The micro-switches with bi-metallic and binary alloy contacts exhibited contact resistance between $1 - 2 \ \Omega$ and, when compared to micro-switches with sputtered gold contacts, showed an increase in lifetime. The micro-switches with tertiary alloy contacts showed contact resistance between 0.2-1.8 Ω and also showed increased lifetime. Overall, the results presented in this dissertation indicate that micro-switches with gold alloy electric contacts exhibit increased lifetimes in exchange for a small increase in contact resistance.

ELECTROSTATIC RADIO FREQUENCY (RF) MICROELECTROMECHANICAL SYSTEMS (MEMS) SWITCHES WITH METAL ALLOY ELECTRIC CONTACTS

I. Introduction

1.1 Motivation

Electrostatic radio frequency (RF) microelectromechanical systems (MEMS) metal contact switches are paramount in importance for future miniaturizations of RF and microwave circuitry and systems [14, 39, 17, 27, 109, 124, 125, 131, 160]. RF MEMS switches are needed building blocks for improving current (i.e., Phase shifter circuits, tunable RF filters, true-time delay networks, and phased array radar [53, 69, 70, 87]) and enabling future USAF and DOD systems like the space-based radar (SBR. SBR data will be used to support the intelligence, surveillance, and reconnaissance (ISR) missions.

Electrostatic RF MEMS switches, like that shown in Figure 1, are ideally suited for RF applications because of their small geometries, superior RF performance over current solid state switching devices like field effect transistors (FET) and positive-intrinsic-negative (PIN) diodes, and low power consumption [49, 124].

1.2 Problem Statement

Important performance criteria for micro-switch applications are low contact resistance ($< 1 - 2 \ \Omega$) and reliability (switch lifetimes $> 10^{11}$ "cold-switched" or $> 10^8$ "hot-switched" cycles). Hot-switching is defined as switch cycling with a signal or potential difference across the electric contacts while cold-switching is defined as device actuation with no signal or voltage potential across the contacts. The
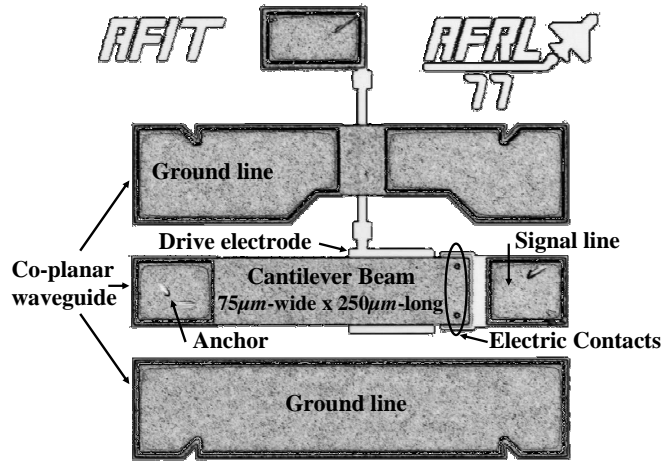
Figure 1   A captured video image of a cantilever-style, RF MEMS metal contact switch.

two primary failure mechanisms for MEMS metal contact switches are becoming stuck closed (i.e., sticking friction or stiction) and increased contact resistance with increasing switch cycles. Typically, micro-switches use gold-on-gold electric contacts to achieve low contact resistance. Gold (Au) is used due to its low resistivity and low susceptibility to oxidation and contaminant gettering. MEMS switches with Au electric contacts, however, are prone to stiction and wear due to Au's relative low material hardness of approximately 1-2 giga pascals (Pa).

Previous attempts to address these micro-switch failure mechanisms have concentrated on optimizing mechanical switch designs [101, 116]. In this study, different electric contact metallurgies, specifically metal alloys, were investigated to improve micro-switch performance.

1.3   Contributions

The novel contributions of this work, to the MEMS field, follow:

1. analytic contact force models for cantilever-style, electrostatic, micro-switches,

2. an analytic micro-switch contact resistance model for devices with sputtered contact metals,

3. a binary metal alloy selection methodology for micro-switch electric contacts,

4. measured thin film metal (i.e Au, Ag, Pd, and Pt) and alloy (i.e., Au-Pd, Au-Pt, and Au-Ag) material properties,

5. co-sputtering fabrication technique for depositing alloy contact metals,

6. an improved hemispherically-shaped upper electric contact geometry,

7. operational RF MEMS metal contact switches with bi-metallic, binary alloy, and ternary alloy electric contacts, and

8. contact resistance, RF measurements, and micro-switch lifecycle test results of micro-switches with metal alloy electric contacts.

1.4 Publications

The following papers, listed for the convenience of the reader, were published by the author during the course of this dissertation research:

Journal Articles:

1. "Modeling and Simulation of Classical Micro-Electro-Mechanical Systems (MEMS) Actuators" [34],

2. "A Comparison of Micro-Switch Analytic, Finite Element, and Experimental Results" [32],

3. "Selecting Metal Alloy Electric Contact Materials for MEMS Switches" [29],

Conference Papers:

4. "Finite Element Modeling and Simulation of Micro-Switch Pull-in Voltage and Contact Force" [31],

5. "Contact Force Models, including Electric Contact Deformation, for Electrostatically Actuated, Cantilever-Style, RF MEMS Switches" [28],

6. "RF MEMS Switches with Metal Alloy Electric Contacts" [30], and

7. "Micro-Switches with Sputtered Au, AuPd, Au-on-AuPt, and AuPtCu Alloy

Electric Contacts" [33].

1.5   Organization

This document is comprised of eight chapters and two appendices. Chapter one, the introduction, briefly introduces the topic of electrostatic RF MEMS metal contact switches. Chapter two is a comprehensive literature review of MEMS switches and related fields. Chapter three is a brief presentation of pertinent theory. Chapter four summarizes the methodology used to select alloy contact materials. Chapter five presents an analysis of micro-switch mechanical designs using analytic equations, a finite element method software tool (i.e., Coventorware), and experimental data. Chapter six is a discussion of the fabrication processes. Chapter seven presents the experiments and test results. Chapter eight details the overall conclusions including ideas for future research. Finally, a complete listing of the fabrication process checklists or process followers are provided in the appendices.

II. Background

This chapter is a presentation of background material pertinent to studying RF MEMS metal contact switches.

2.1 RF Switches

The ability to switch RF and microwave signals between components and systems is an important aspect of RF and microwave systems design [14, 120]. For example, phase shifter circuits can be realized by switching between different RF components or loads. There are two circuit configurations for RF switches, series and shunt [17, 160]. Series switches are placed within a transmission line and are used to physically open or close the signal path, while shunt switches are placed between the signal line and ground and used to pass or short microwave signals. RF switches can either be normally open (NO) and actuated closed or normally closed (NC) and actuated open.

2.1.1 Semiconductor. FETs and PIN diodes are currently used as switching elements in microwave circuitry. This is primarily because semiconductor devices are easily integrated with planar microwave devices (i.e., co-planar waveguides (CPW) and monolithic microwave integrated circuits (MMIC)) and have extremely fast switching times ($< 10 \; ns$) [120]. FETs and PIN diodes generally offer high isolation in the open state ($> 20 \; dB$) and low insertion loss (IL) in the closed state ($< 1 \; dB$), however, performance deteriorates rapidly at frequencies higher than a few giga hertz (Hz). For example, solid state devices operating above 1 GHz will typical have isolation and IL values of $20 - 25 \; dB$ and $1 - 2 \; dB$, respectively [160]. DC power consumption is relatively high with semiconductor switches ($> 10 \; mW$) [160] and signal bandwidth is limited by the mobility of the semiconductor carriers (i.e., electrons and holes). Also, intermodulation distortion in semiconductor devices

is prevalent due to their nonlinear current versus voltage (I-V) characteristics. These problems can all be alleviated by using mechanical switches.

  2.1.2 Electromechanical. Macro-size electromechanical switches, compatible with coaxial cabling or waveguide, can be also be used to switch microwave energy [49, 120]. Electromechanical RF switches offer excellent isolation ($> 70\ dB$) and IL ($< 0.07\ dB$) but have relatively slow switching speeds ($2 - 15\ ms$), are non-planar, and not easily implemented with planar RF circuitry [160]. Additionally, electromechanical switches have improved signal bandwidth and intermodulation performance over semiconductor switches. Bandwidth improvements result from using metals, not semiconductors, with higher carrier mobilities. Intermodulation distortion is minimized with mechanical switching elements because they exhibit linear I-V characteristics.

  Although, macro-switches and relays can be used effectively with RF signals, they have somewhat limited utility because of their slow switching speeds and bulky, non-planar fabrication processes. These issues can be addressed by using micro-sized or MEMS switching devices [17, 63, 172].

2.2 RF MEMS Switches

  MEMS is a unique technology that combines many of the advantages of solid state and electromechanical devices. High isolation ($> 40\ dB$), low IL ($\approx 0.1\ dB$), extremely low power consumption when electrostatically actuated , high bandwidth (DC-100 GHz), moderate switching speeds ($1 - 10\ \mu s$), superior intermodulation performance, and planar fabrication have all been realized using RF MEMS switches [124, 125, 123, 160, 170]. There are two classes of RF MEMS switches, capacitive and metal-to-metal contact. In general, capacitive switches are used in the shunt circuit configuration while metal contact switches are used in the series circuit configuration. Metal contact switches work well in the DC-40 GHz frequency range and capacitive

switches operate best from 5-100 GHz [124]. Table 1 summarizes some of the key parameters for PIN diodes, FETs, and RF MEMS switches [160, 170].

Table 1   PIN diode, FET, Electromechanical, and RF MEMS parameters.

Parameter	PIN diode	FET	Electromechanical	RF MEMS
Isolation	40 dB	20-40 dB	> 70 dB	> 40 dB
Insertion Loss	.5-1 dB	.5-1 dB	.07 dB	.1 dB
Switching Speed	650 ns	3 ns	2-15 ms	1-10 μs
Power Consumption	30-50 mW	5 mW	.2-.4 mW	$\approx$ 0 W
Bandwidth	20-2000 MHz	5-4000 MHz	DC-26 GHz	DC-100 GHz

A brief discussion on MEMS capacitive switches is presented next.

2.2.1   *Capacitive.*   MEMS capacitive switches are used to vary signal impedance when opened or closed. In the shunt configuration the upstate or unactuated switch will pass RF energy while the downstate or actuated switch will short RF signals to ground [124, 160]. The main problem with current electrostatic RF MEMS capacitive switches is charge accumulation in the switch's dielectric material. Dielectric charging causes variations in switch actuation voltage and corresponding changes in open and closed switch capacitance values. Dielectric charging effects are not usually present in metal contact micro-switches. A comprehensive literature review on MEMS metal contact switches and related topics is presented next.

2.2.2   *Metal Contact.*   Metal contact micro-switches are opened or closed to change circuit impedance and route electrical signals. In the series configuration an open switch behaves like a capacitor and blocks RF energy and when closed acts like a short and passes RF signals [124, 160].

Peterson theorized that contact force, metallurgy, and geometry were the key areas that needed further study before reliable electrostatic MEMS contact switches could be realized [118]. The primary failure mechanisms for RF MEMS contact

switches are stiction and wear. Many metal contact micro-switch studies have focused on mechanical switch designs with Au electric contacts [38, 94, 118, 173].

2.2.2.1 *Mechanical Designs.* Electrostatically actuated metal contact micro-switches are the most prevalent because they require virtually no power to operate [124]. Electrostatic devices, however, usually require high actuation voltages (60-120 V) to achieve low contact resistance. Consequently, innovative electrostatic mechanical switch designs exhibiting low actuation voltages have been studied extensively [6, 10, 22, 23, 110, 116, 124, 134]. Much of this work, however, boils down to an engineering trade off between beam spring constant and switch actuation voltage. A problem with this design approach is that by lowering the mechanical spring constant (i.e., the actuation voltage) the switch restoring force (i.e., through Hooke's law) is also lowered which may lead to increased stiction failures.

2.2.2.2 *Contact Metals.* Very few researchers have investigated using different electric contact metals or alloys to minimize stiction and improve micro-switch wear characteristics. Schimkat studied Au, Au-nickel (Ni) alloy (Au-(5%)Ni) and rhodium (Rh) macro-switch contacts (i.e., not MEMS switches) in a low-force test configuration. The macro-sized contacts were electrically "cleaned" using a "Schaltreinigung" technique that consisted of approximately 40 switch cycles with a $50\,VDC$ and $50\,mA$ electrical load in an nitrogen environment. Schimkat found that Au electric contacts required the lowest contact force to achieve the lowest contact resistance but also resulted in the highest contact adhesion force. The other contact metals (Rh and Au-(5%)Ni) resulted in lower contact adhesion but required higher contact force for low contact resistance [135, 136].

Despite this finding, metal contact micro-switch research has focused on the mechanical and RF design aspects for micro-switches with Au electric contacts [20, 44, 45, 52, 55, 61, 85, 103, 129, 150]. Notable exceptions are Majumder et al.'s and Duffy et al.'s utilization of a "platinum group" and Pt contact metals, re-

spectively [44, 92]. Additionally, Hiltmann et al. studied micro-switches fabricated with Au-cobalt (Co) alloy, Pd, and Rh electric contact materials [56]. These metals were chosen over Au for their increased hardness, lowered adhesion, and improved wear characteristics. In order to achieve acceptable contact resistance, Majumder et al.'s micro-switches required multiple (i.e., 4 to 8), parallel contacts and were packaged in a hermetic environment while Duffy et al.'s MEMS switches required actuation voltages approximately 45 V higher than the pull-in voltage. Hiltmann et al.'s switches were large, millimeter-sized micromachined membrane switches (i.e., not micro-switches) capable of generating several Newtons of contact force [56]. In addition, the alloy composition and specific details about the contact material deposition were not provided [56].

2.2.2.3 Lifecycle Results. Generally, micro-switches with Au electric contacts are limited to approximately 10^6 "hot-switched" cycles and greater than 10^9 "cold-switched" cycles, most likely, because evaporated Au is a soft metal prone to stiction and wear [10, 22, 55, 61, 90, 94, 95, 92, 173]. Zavracky et al. report $5 \cdot 10^8$ "hot-switched" cycles and over $2 \cdot 10^9$ "cold-switched" cycles for micro-switches packaged in nitrogen and fabricated with sputtered Au contacts [173]. Majumder et al. reports greater than 10^7 "hot-switched" cycles and approximately 10^{11} "cold-switched" cycles for micro-switches with a "platinum group" contact metal [92, 93]. Hiltman et al. reports greater than $20 \cdot 10^6$ "hot-switched" cycles for millimeter-sized micromachined membrane switches with Au-Co alloy, Pd, and Rh electric contacts [56].

2.2.2.4 Contaminant Films. Contaminant films are normally present on all electric contact surfaces. The composition and thickness of these films vary depending on the specific type of contact metal. Gold for example, is a noble metal that does not have a native oxide but readily adsorbs monolayers of hydrocarbons and oxygen (due to relative humidity). Silver, on the other hand, adsorbs monolayers

9

of hydrocarbons and oxygen and tarnishes (i.e., forming a robust surface film) in the presence of sulfur [54]. Gold adsorbed films, typically 20-40 Å thick, can be ruptured (i.e., fritting) with MEMS switches capable of producing hundreds of micro newtons of contact force [59, 79, 135]. Fritting is defined when contaminant films are "mechanically ruptured in some spots at contact make or are electrically broken down when enough voltage is applied" [59]. In some cases, the available contact force can not penetrate contaminant film layers and achieve good metal-to-metal contact. When contaminant films cause high contact resistance, electric contacts can be mechanically or electrically "cleaned" prior to use. Mechanical cleaning involves "wiping" the contacts together to physically puncture or move away contaminants and needs to be incorporated into the switch's mechanical design. Electrical contact cleaning involves using an electric potential across the switch contacts to induce a micro-arc and burn off contaminants prior to switch closure [59, 105]. Contaminant films are, most likely, a contributing factor to the wide variation in published lifecycle test results.

Controlling contaminant films is an important consideration for achieving high performance with MEMS switches. As previously discussed, carbonaceous films can inhibit metal-to-metal contact resulting in high contact resistance. Contaminant films, however, are useful in micro switches to help control the number of microwelds and limit contact stiction [62, 157]. Unfortunately, most "hot switching" or attempts to electrically clean micro-contacts have resulted in accelerated contact wear due to material transfer.

2.2.2.5 Electric Contact Wear. Other material wear mechanisms include abrasive, adhesive, fretting, and mechanical or strain-hardening. [59, 67, 71]. Abrasive wear results when one contact is harder or rougher than the other which causes micro metallic particles to break off. Adhesive wear results when the bonding energy due to surface free energy states is greater than the mechanical separation force [2, 4, 18]. Adhesion is further characterized by a force required to pull two

materials apart or a pull-off force [4]. The Johnson, Kendall, and Roberts (JKR) and the Derjaguin, Muller, and Toporov (DMT) contact models both consider free surface energy states while Hertzian mechanics does not [2]. The JKR and DMT contact models are most appropriate for characterizing nanonewton force interactions like those in atomic force microscopy (AFM). Fretting, is a result of excessive motion, caused by shock, vibration, or thermal cycling, at the interface of a closed electric contact [37, 48]. Temperature coefficient of expansion (TCE) mismatches between contact materials induce vibration through repeated thermal cycling. Strain-hardening is a result of repeated compression, heating, and plastic material flow between electric contacts [2, 83]. A result of these wear mechanisms is that microscopic pieces of material remain on the contact surfaces between switch cycles and create contamination layers composed of metal particles and hydrocarbons [163]. This situation can be modeled by a-spots completely surrounded by insulating rings of corrosion [147].

2.2.2.6 Modeling. In addition to designing, fabricating, testing actual MEMS switches, contact force, contact resistance, thermal effects, and RF modeling are useful for predicting and investigating micro-switch performance [49, 66, 82, 96, 154, 169]. Prior contact force modeling has primarily focused on the mechanical aspects of the micro-switch design to achieve the necessary contact force for low contact resistance connections [63, 95]. Majumder et al. modeled micro-switches as a cantilever beam with a fixed end and a free end and iteratively determined contact force as a function of the beam's actuation voltage [95]. Hyman et al. modeled contact force analytically using Euler-Bernoulli beam theory with Young's modulus replaced by the plate modulus [63].

When modeling micro-contact resistance, neglecting ballistic electron transport [16] and contaminant film resistance [95] underestimates contact resistance for low contact force applications. Majumder et al. developed a micro-contact resistance model [95] that considered ballistic and diffusive electron transport by using Wexler's

interpolation [167], contact material deformation by using Hertz's [59] elastic and Chang et al.'s [25] elastic-plastic (i.e., the CEB model) models, multi-asperity contact areas using Greenwood and Williamson's "asperity-based model" [51], and the single effective asperity contact area based on Holm's model [59]. Using these models, Majumder et al. predicted a lower contact resistance bound when using the multi-asperity model and an upper contact resistance bound when using the single effective a-spot model [95].

Majumder, et. al.'s model, however, does not account for a contact load discontinuity at the transition from elastic to elastic-plastic material deformation present in the CEB model. Kogut and Etison addressed this by using finite element methods and modeling the elastic-plastic region with normalized contact force and area equations based only on Hertzian elastic contact mechanics equations [72, 73]. Chang observed that ideal plastic behavior normally occurred at $3Y$, not $K_Y Y$, where K_Y is the yield coefficient, and updated the CEB model using a linear interpolation [24].

In addition, Majumder et al.'s model uses a gamma function, needed for Wexler's interpolation, that is not well defined ($\Gamma(K = \infty) \neq 0$). Majumder et al.'s Gamma function predicts ballistic and diffusive electron transport when the Knudsen number (K) goes to infinity which should be the completely ballistic region (i.e., $\Gamma(0) = 1$ and $\Gamma(\infty) = 0.694$). This choice of Gamma function is questionable because it does not predict the expected completely ballistic and completely diffusive electron transport when taking the limits of Wexler's interpolation equation. Mikrajuddin et al. derived from first principles a well behaved Gamma function that is used with Wexler's interpolation to determine size-dependent constriction resistance [104].

Kogut and Komvopoulos derived an electrical contact resistance (ECR) model for conductive rough surfaces based on a fractal geometry surface topography description, elastic-plastic deformation of contacting asperities, and size-dependent electrical constriction resistance of micro-contacts comprising the real contact area [75].

Additional work by Kogut and Komvopoulos resulted in an ECR model for conductive rough surfaces coated with a thin insulating layer based fractal geometry to describe the surface topography, elastic, elastic-plastic, and fully plastic deformation of surface asperities, and quantum mechanics considerations for the electric-tunnel effect through a thin insulating layer [76]. Kogut and Komvopoulos' ECR models are based Kogut and Etison's elastic-plastic normalized force and area model, Sharvin's resistance model, and Mikrajuddin et al.'s derived Gamma Function. In addition, both models (Kogut and Komvopoulos and Majumder et al.) are based on the assumption that surface asperities have sufficient separation and behave independent of each other.

Majumder et al. measured actuation voltage and contact resistance using MEMS switches and inferred micro-switch contact force through modeling [95]. Peroulis and Katehi measured device RF isolation using a MEMS device and inferred the contact force and resistance relationship [115]. Hyman and Mehrengany used a piezo-transducer and a precision balance to bring micro-contacts together and simultaneously measure contact force and resistance [62]. Vinci and Bravman reported on microcantilever beam testing that used a nanoindentor to manipulate micro-sized devices to determine thin film material properties [162]. Pruitt and Kenny evaluated micro-contacts using silicon cantilever beams with embedded piezoresistive force sensors [122]. They simultaneously measured contact resistance, using a four-wire test configuration, and contact force while testing evaporated, sputtered, and electroplated Au films [122]. Beale and Pease studied the effects of contaminant films on low force contacts by using atomic force microscopy (AFM) cantilevers and a two-wire resistance measurement scheme [8, 9]. Tringe et al. investigated the contact force and resistance of single asperity Au electric contacts using interfacial force microscopy (IFM) [157].

2.2.2.7 Other Approaches. Finally, several unique micro-switch studies have been accomplished. Oberhammer et al. studied a flexible membrane S-

shaped switch that was actuated between an upper and lower electrode [110, 111]. Surface micromachined flip switches with hinges at the beam root were investigated Cowan [36] and also by Kading [68]. Ertl et al. fabricated contacts switches with superior mechanical properties by using a diamond structural layer and electric contacts (i.e., P-doped diamond) [46]. Contact switches based on torsion actuators have also been studied for their increased restoring force [119, 134]. Electrothermal [165, 168] and electromagnetic [52, 153] switch actuation schemes have also been studied. Lateral contacts have been investigated as an alternative to vertical contacts [81, 88, 133, 143]. Lee et al. investigated using an integrated microrelay and power transistor surge suppression circuit to increase switch contact lifetime [86]. Peroulis et al. proposed a unique solution to the stiction problem by decoupling the contact and restoring forces with residual stress cantilever beams to generate the contact force and electrostatic actuation to generate the separation force [117]. Mercado et al. developed an approach to systematically characterize stiction force due to the contact metals. Their designs, based on this approach, consisted of micro-switches, with appropriate geometries, that used side placed (i.e., side versus end contacts) electric contacts to increase mechanical advantage to improve both contact and restoring forces [101].

2.2.2.8 *This Study.* Unlike any other work found in the open literature, metal contact micro-switches (i.e., DC-only and RF-testable) with metal alloy electric contacts were designed, fabricated, and tested during this dissertation [30, 33]. While Majumder et al. used "platinum group" contacts and Duffy et al. used Pt contacts in their micro-switches, in this research micro-switches with sputtered bi-metallic (i.e., Au-on-Au-(6.3at%)Pt), binary alloy (i.e., Au-(3.7at%)Pd and Au-(6.3at%)Pt), and ternary alloy (i.e., Au-(5at%)Pt-(0.5at%)Cu) electric contacts were developed for the first time [30, 33]. In addition, a binary alloy composition selection methodology was developed to avoid two-phase alloy regions, intermetallic compounds, the need for high actuation voltages, and also allow for the testing of

un-packaged devices [29]. These considerations helped ensure that device fabrication was consistent and repeatable.

In addition, no other previous micro-switch study has considered the benefits of using hemispherical-shaped upper and planar-shaped lower contact geometries and sputtered contact films [30, 33]. Figure 2 is a side view of contact area illustrating the improved hemispherical-shaped contact geometry and the placement and thicknesses of the electric contact metals.
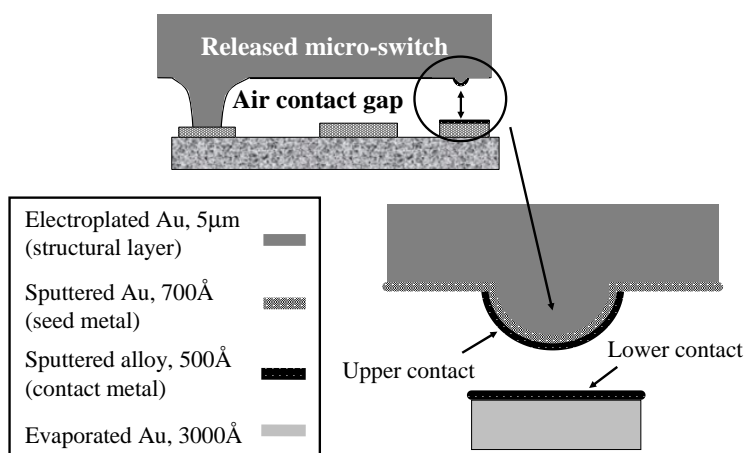
Figure 2   Depiction of the side view and magnified view of the proposed upper contact bump/dimple for the MEMS switch test structure.

Sputtered electric contact materials with low surface roughness and tightly packed material grain structures, used in this work, necessitate using the single effective a-spot contact area model because the surface asperity independence assumption, used by Majumder et al. and Kogut and Komvopoulos, was no longer valid [75, 95]. Improved contact force models that consider beam tip deflection, electric contact material deformation (i.e., elastic, plastic, and elastic-plastic), and utilize the single effective a-spot contact area model were developed [28, 34, 33]. An analytic micro-switch contact resistance model, based on the the single effective a-spot contact area model, was developed using Hertz's [59] elastic, Chang's [24] improvements to the CEB model, Mikrajuddin et al.'s [104] derived gamma function,

and Wexler's [167] interpolation from ballistic to diffusive electron transport [33]. Finally, a nanoindentor was used to manipulate actual MEMS devices to validate the improved contact force and contact resistance models. The necessary theory for understanding RF MEMS metal contact switches with regards to this work is presented in chapter III.

III.   Theory

Relevant theory for modeling, designing, and fabricating RF MEMS metal contact switches is presented in this chapter. The following section, with italicized keywords, provides the necessary connection between relevant theory and the micro-switches investigated in this study. Novel contributions to the MEMS field are presented in Sections 3.7 (analytic contact force models for cantilever-style, electrostatic, micro-switches) and 3.10 (an analytic micro-switch contact resistance model for devices with sputtered contact metals).

3.1   Micro-Switch Physical Description

Electrostatically actuated, cantilever-style, series, DC and RF-testable, MEMS metal contact switch test structures, shown in Figures 3 and 4, were designed, fabricated, and tested to evaluate using metal alloy electric materials.
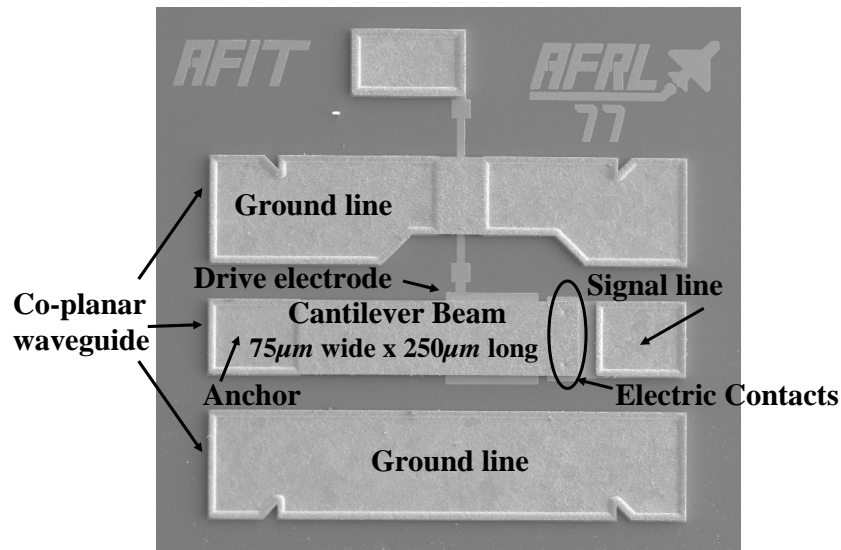
Figure 3   Top view SEM image of an SNM02 RF-testable micro-switch.

The micro-switch mechanical design was based on a *cantilever beam model* and the electrical design was based on a *parallel plate capacitor model*. In addition, *RF*
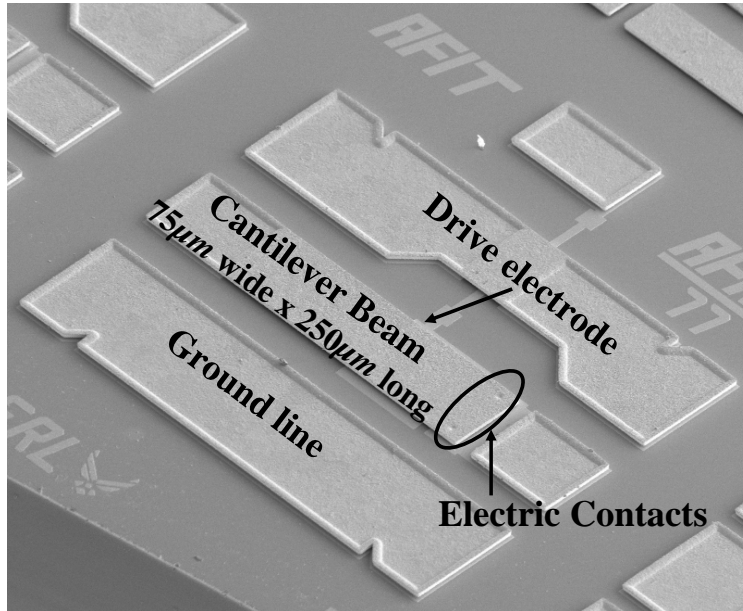
Figure 4   Isometric view SEM image of an SNM02 RF-testable micro-switch.

models and effects were considered by designing the micro-switches as part of a 50 Ω characteristic impedance CPW to facilitate RF testing [14]. The MEMS switches were *surface micromachined* with an electroplated gold structural layer on highly resistive sapphire substrates. The SNM02 micro-switch test structure, discussed in detail in section 5.3, was used to investigate sputtered *binary metal alloy* contact materials, hemispherical-shaped upper and planar lower electric contact geometries, and the effects of mechanical "cleaning" (i.e., "wiping") on *contact resistance* during beam bending. An overview of MEMS fabrication technologies are presented next.

3.2 MEMS Fabrication

MEMS fabrication consists of three basic technologies: bulk micromachining, micromolding, and surface micromachining. Bulk micromachining is a "substractive" process that is used to etch MEMS structures into the bulk substrate [80]. Micromolding uses electroplated materials to fabricate high-aspect ratio MEMS de-

vices [80]. Surface micromaching is an "additive" process and is used to construct MEMS structures from layers and films deposited onto the substrate [80].

3.2.1 Bulk Micromachining.   Bulk micromachining is used to form micro-sized structures in the bulk of single-crystal wafers by selectively removing or etching controlled amounts of material. Wet etching uses aqueous chemicals and dry etching uses vapor or plasma etchants. Wet etching is accomplished, isotropically or anisotropically, by dipping substrates into etchant baths. Often times isotropic etching, shown in Figure 5, results in defined structural and sacrificial layers being undercut.

Isotropic wet etching: agitation

SiO$_2$ mask

Isotropic wet etching: no agitation
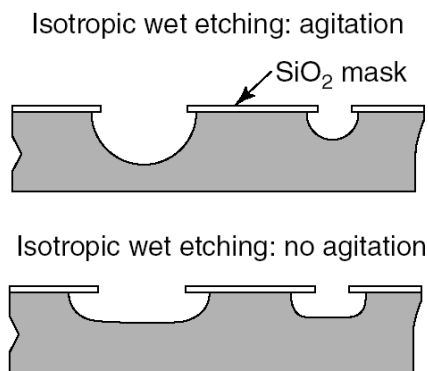
Figure 5   Isotropic bulk material etching [91].

When single-crystal material is anisotropically etched, the crystal orientation effects the etch time. For example, the (111) planes of crystalline silicon etches much slower than other crystal planes resulting in V-shaped or inverted pyramid-shaped structures (illustrated in Figure 6) depending on the masked area, the etch time, and the substrate thickness.

Anisotropic wet etchants like potassium hydroxide (KOH), ethylenediamine pyrocatechol (EDP), tetramethylammonium hydroxide (TMAH), and hydrazine-water are used for etching silicon substrates [80, 91].
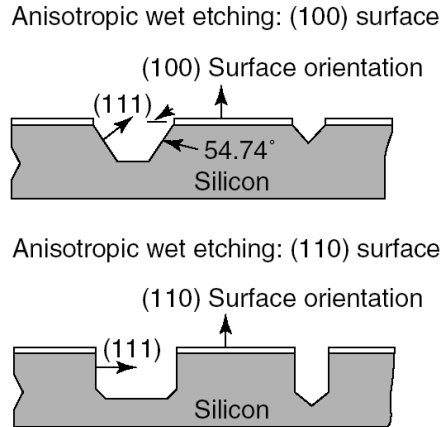
Figure 6   Anisotropic bulk material etching [91].

The etching process can be made selective when dopants (e.g., heavily doped regions tend to etch more slowly) are used to create "etch-stops" or even stopped electrochemically (e.g., etching stops when a region of different polarity is encountered and a pn junction is formed). An "etch-stop", illustrated in Figure 7, is a region where etching slows down or is stopped [80, 91].
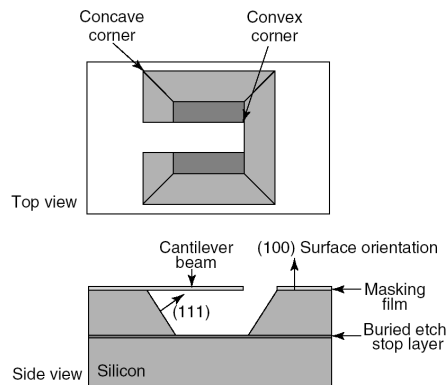
Figure 7   Etch stops [91].

Dry etching occurs through chemical or physical interactions between ions in the plasma or gas and atoms of the substrate. Reactive ion etching (RIE), where external energy drives chemical reactions in low-pressure reaction chambers, is commonly used to dry etch bulk silicon. A variety of chlorofluorocarbon gases, sulfur hexafluoride, bromine compounds and oxygen are commonly used as reactants.

Anisotropic dry etching processes are widely used in MEMS because chemical contamination is minimal and arbitrarily oriented features can be etched. Very deep silicon microstructures can be obtained by deep RIE or DRIE [80, 91].

Using bulk micromachining, high-aspect ratio structures can fabricated that range from submicron to full wafer thickness (i.e., $\approx 500~\mu m$) with lateral dimensions ranging from submicron to wafer diameter. Micromolding is another technology used to fabricate high-aspect ratio MEMS devices.

3.2.2 Micromolding (LIGA). LIGA (i.e., a German acronym for Lithographie, Galvanoformung, Abformung) is an example of a micromolding fabrication process. It was developed in the 1980s using X-ray lithography and electroplating to form micro-sized metallic parts or precision molds [91]. The LIGA process is detailed in Figure 8.
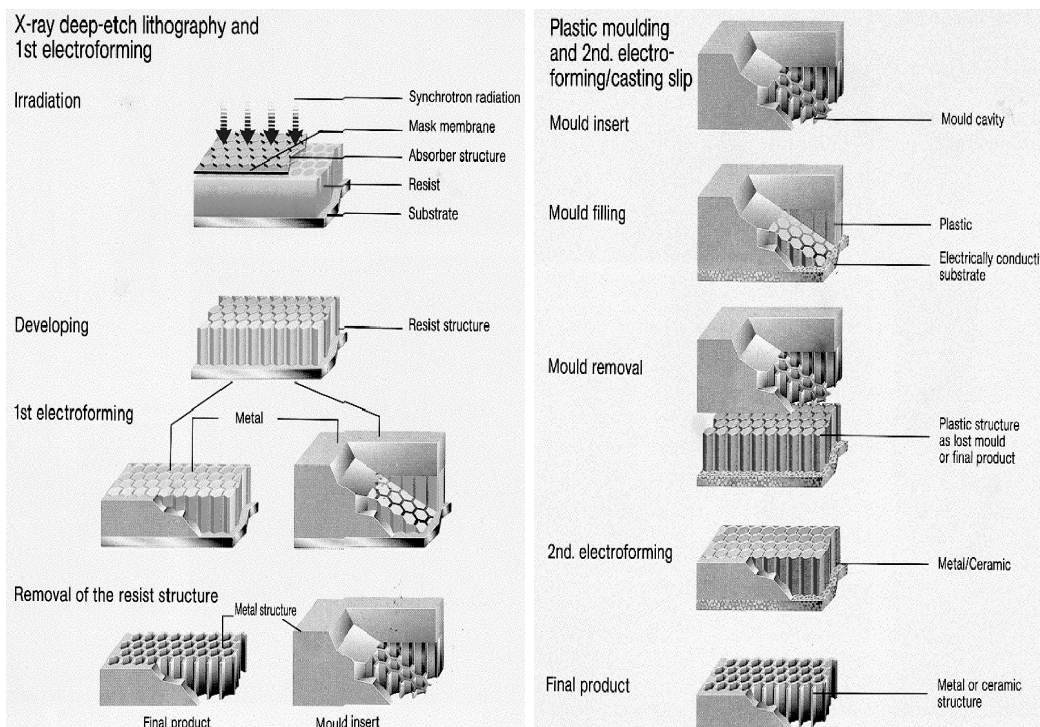
Figure 8   Detailed description of the LIGA process [91].

High-aspect ratio microstructures with heights ranging from hundreds of microns up to the centimeter scale and submicron lateral resolution are possible using thick photoresist layers and LIGA's X-ray lithography technique [91, 47]. In addition, various materials can be used with LIGA to allow many different device actuation schemes (i.e., electrostatic, magnetic, piezoelectric, etc.). A major drawback to using LIGA is the high production costs associated with using X-ray lithography. Surface micromachining, discussed next, was used to fabricate the devices investigated during this research.

3.2.3 Surface Micromachining. Unlike bulk micromachining, surface micromachining is used to build structures onto the substrate's surface by depositing, patterning, and etching thin "sacrificial" and "structural" layers. The MEMS devices are then "released" by removing sacrificial layers and leaving behind free standing mechanical structures. Figure 9 illustrates a silicon based process flow for a cantilever beam.
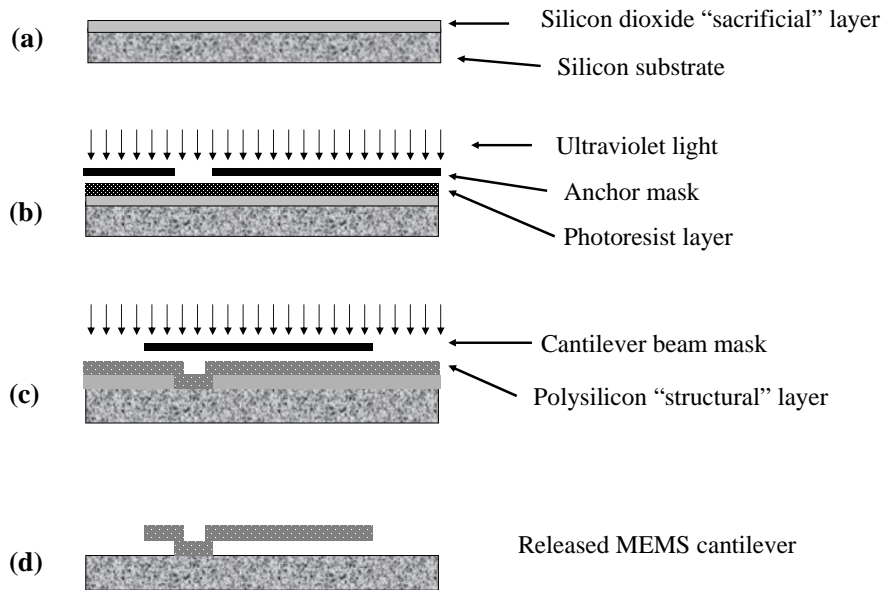
Figure 9   Example surface micromachining process flow for a cantilever beam.

Refer to Figure 9 for the following discussion. The sacrificial silicon dioxide layer is first deposited onto the silicon wafer (**a**) [91]. The cantilevers anchor is then patterned in the sacrificial layer using standard photolithography techniques (**b**) [91]. Next, the polysilicon structural layer, connected to the substrate at the anchor, is deposited onto the silicon dioxide sacrificial layer and the beam patterned using standard photolithography (**c**) [91]. Finally, the cantilever is released by etching away the sacrificial silicon dioxide layer (**d**) [91].

Surface micromachined structures are normally much smaller than bulk micromachined or LIGA structures and have an advantage of being more easily integrated with other solid state components. A drawback for some mechanical sensing and actuation applications is that surface micromachined devices have lower overall mass than bulk micromachined or LIGA structures.

Surface micromachining requires a compatible set of structural materials, sacrificial materials, and chemical etchants. The structural materials must have suitable mechanical properties (e.g., elastic modulus, yield point, melting temperature, etc.) that are suitable for the desired application. In addition, the sacrificial materials must have good mechanical properties (e.g., good adhesion and low residual stresses) to avoid device failure during fabrication. The etchants must have selectivity and be able to etch off sacrificial materials without affecting the structural layers. In addition the etchants must have proper viscosity and surface tension characteristics to avoid stiction during the release process. A common set of compatible materials used in surface micromachining are polysilicon structural layers and silicon dioxide sacrificial layers all deposited using low-pressure chemical vapor deposition (LPCVD). The oxide is readily dissolved in a hydrofloric acid (HF) solution with minimal effect on the polysilicon layer. The specific process and materials used to fabricate the device used in this dissertation are presented in chapter VI and in Appendices A and B.

Surface micromachined devices are normally two dimensional in the plane of substrate and other techniques have been developed to extend conventional surface micromachining into the third dimension. For example, when polysilicon flat plates are connected to each other and the substrate using hinges, three dimensional structures can be assembled after release. Once fabrication is complete, MEMS devices are actuated using various physical phenomena (e.g., electrostatic, magnetic, piezoelectric, etc.). Electrostatic actuation, based on beam and parallel plate capacitor models, is commonly used for RF MEMS switches. The beam and parallel plate capacitor models, used in this research, are discussed next.

3.3   Beam Models

3.3.1   Cantilever Beam.   Euler-Bernoulli beam bending theory, based on small deflection beam theory (i.e., linear analysis), and the principle of superposition, is used to develop the beam models in this study [142]. Additionally, the beams are assumed to be flat and not curled due to residual stresses from the fabrication process. This assumption is substantiated in Figures 3 and 4 and again in chapter VI.

Prior to micro-switch closure or pull-in, it is assumed that the cantilever behaves like a beam, as illustrated by Figure 10, with a fixed end at $x = 0$, a free end at $x = l$, and an intermediately placed external load (F_a) at $x = a$ [124, 142]. The externally applied load, modeled as a point source, is located above the center of the switch's drive electrode.

Using the method of moments, Equation 1 results and is used to determine maximum beam tip deflection with the intermediately placed load [142, 89]:

$$d = \frac{F_\mathrm{a} a^2}{6 E I_\mathrm{z}} (3l - a) \qquad (1)$$
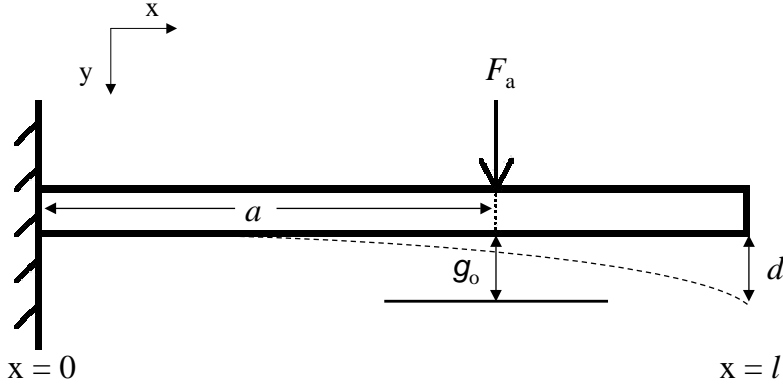
Figure 10   Cantilever beam model with a fixed end at $(x = 0)$, a free end at $(x = l)$, and an intermediately placed external load, F_a.

where, d is the maximum cantilever beam tip deflection, F_a is the externally applied load, a is the load position, l is the length of the beam, E is the elastic modulus, and I_z is the area moment of inertia about the z-axis defined in Equation 2:

$$I_z = \frac{t^3 w}{12} \tag{2}$$

where, t is the beam's thickness and w is the beam's width.

In equilibrium, the beam acts like a spring and the externally applied load is equal to the beam's mechanical restoring force resulting in a Hookes' law relationship [142, 89].

$$F_s = kd \tag{3}$$

where, F_s is the mechanical restoring or spring force of the cantilever beam, k is the spring constant, and d is the deflection distance at the tip of the cantilever.

The spring constant for the beam shown in Figure 10 is found by solving Equation 1 for the applied force and substituting Equation 2 for area moment of inertia, resulting in:

$$k_1 = \frac{Et^3w}{2a^2(3l - a)} \tag{4}$$

where, k_1 is the spring constant for the model depicted in Figure 10.

An improved beam model that accounts for anchor height is presented next.

3.3.2 Improved Beam Model. The effects of the anchor height on beam tip deflection were investigated using Meng et al.'s cantilever beam model, shown in Figure 11, that accounts for elastically restrained beam supports [100].
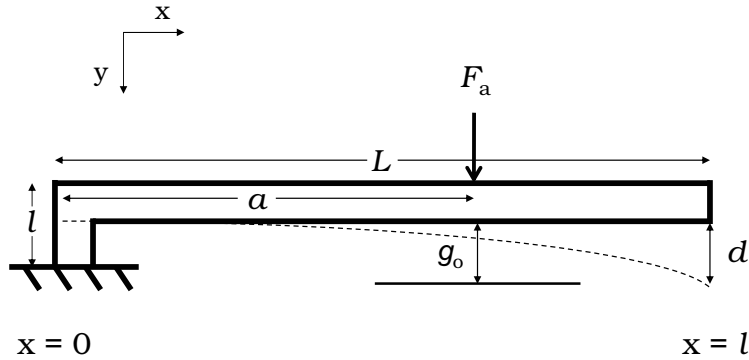
Figure 11   Improved beam model that is fixed to the substrate, has a free end at $(x = l)$, and an intermediately placed external load, F_a and considers the effects of the anchor height on beam tip deflection.

The improved beam model assumes the anchor support is fixed to the substrate, has a straight-edge, forms a 90° angle with long section of the beam, has a free end at $(x = l)$, and has an intermediately placed external load (F_a). In addition, the plate modulus is used instead of the elastic modulus since the beam's width is much greater than its thickness $(w > 5t)$. The externally applied load, modeled as a point source, is located above the center of the switch's drive electrode. The devices fabricated in this study adhere to the assumptions needed for Meng and Mehregany's improved beam model [100].

26

Using the method of moments, Meng and Mehregany derived Equation 5 (with a typographical error, which is corrected here) which analytically predicts the maximum beam tip deflection with an intermediately placed load [100].

$$d = \frac{2(1 - \nu^2)}{Ewt^3}[-L^3 + 3aL^2 + (L - a)^3 + 6aLl]F_a a^2 \tag{5}$$

where, L is the length of the beam, l is the height of the anchor, and ν is poisson's ratio.

The spring constant for the beam, shown in Figure 11, is found by solving Equation 5 for the applied force resulting in:

$$F_a = \frac{Ewt^3 d}{2(1 - \nu^2)a^2[-L^3 + 3aL^2 + (L - a)^3 + 6aLl]} \tag{6}$$

and then using Hookes' law to determine

$$k_{1a} = \frac{Ewt^3}{2(1 - \nu^2)a^2[-L^3 + 3aL^2 + (L - a)^3 + 6aLl]} \tag{7}$$

where, k_{1a} is the spring constant for the improved beam model.

Parallel plate capacitor models are presented next.

3.4 Parallel Plate Capacitor Models

The cantilever beam and the bottom electrode, shown in Figures 3 and 4, are modeled as a parallel plate capacitor.

3.4.1 First-Order Parallel Plate Capacitor.

The externally applied load (F_a), modeled as an electrostatic force, was first determined by neglecting fringing fields and using a simple, first-order parallel plate capacitor description. The charge on the parallel plate capacitor is as follows:

$$Q = CV \tag{8}$$

where, Q is the charge, C is the capacitance, and V is the voltage across the parallel plate capacitor. The capacitance of a parallel plate capacitor is given by

$$C = \frac{\epsilon_\mathrm{o} A_\mathrm{sa}}{g} \tag{9}$$

where, ϵ_o is the permittivity of free space, A_sa is the surface area of one parallel plate, and g is the distance or gap between the plates.

The work (W) required to slowly charge the capacitor from 0 to Q coulombs is given by:

$$W = \int_0^Q \frac{q}{C}\,\mathrm{d}q = \frac{Q^2}{2C} \tag{10}$$

where, q is a dummy variable of integration [140].

Substituting in Equation 8 for charge and Equation 9 for capacitance into Equation 10 results in:

$$W = \frac{\epsilon_\mathrm{o} A_\mathrm{sa} V^2}{2g}. \tag{11}$$

Once charged, the work is equated to the potential energy (U) stored in the capacitor [140, 171]. Equation 12 is the relationship that converts potential energy into force [140]. The slowly varying force is called an electrostatic force.

$$F_\mathrm{e} = \frac{-dU}{dg} \tag{12}$$

Finally, after substituting Equation 11 into Equation 12, the electrostatic force due to the charge on a parallel plate capacitor follows:

$$F_{\mathrm{e}} = \frac{\epsilon_{\mathrm{o}} A_{\mathrm{sa}} V^2}{2g^2}. \tag{13}$$

F_{e} is represented, on Figure 10, by the externally applied electrostatic load F_{a}.

A parallel plate capacitor model with a first-order fringing fields correction term is now presented.

3.4.2 First-Order Fringing Field Correction. Osterberg and Senturia developed a first-order fringing fields correction term for the well known first-order parallel plate capacitor model previously discussed [113]. The adjusted model, given by Equation 14, can be used to account for non parallel electric fields that develop outside the confines of the parallel plate capacitor (i.e., the cantilever beam and bottom electrode). This situation is often accentuated when oversized bottom actuation electrodes are used to electrostatically actuate MEMS devices.

$$F_{\mathrm{eFF}} = \frac{\epsilon_{\mathrm{o}} A_{\mathrm{sa}} V^2}{2g^2}[1 + 0.42\frac{g_{\mathrm{o}}}{w}] \tag{14}$$

where, F_{eFF} is electrostatic force adjusted with a first-order fringing fields correction term.

Electrostatic actuation equations, developed using the cantilever beam model and the first-order parallel plate capacitor model, are presented next.

3.5 Electrostatic Actuation

Electrostatically actuated MEMS switches are prevalent because they require virtually no power to operate and are easily modeled using analytic equations. The following electrostatic actuation derivation was accomplished using the cantilever beam model, presented in section 3.3.1, and the first-order parallel plate capacitor model, presented in section 3.4.1. The experimental data that justifies using the first-order parallel plate capacitor model is presented in chapter V, section 5.2.3.1

while the data justifying the cantilever beam model's use is given in chapter VII, section 7.1.1.

In equilibrium, F_e is equal to F_s through Hookes' law. Equating Equation 13 to Equation 3, letting $g = g_o - d$, $k = k_1$, and solving for V yields:

$$V_1 = (g_o - d)\sqrt{\frac{2k_1 d}{\epsilon_o A_{sa}}} \tag{15}$$

where, V_1 is the actuation voltage for the beam illustrated by Figure 10 and g_o is the initial gap under the beam.

The deflection distance when the applied electrostatic force overcomes the beam's mechanical restoring force and the beam snaps down is called the pull-in distance. The pull-in distance (d_{pi}) is determined by maximizing V_1 with respect to d resulting in:

$$d_{pi} = \frac{g_o}{3}. \tag{16}$$

The beam's pull-in voltage, defined the same as the pull-in distance (i.e., when the electrostatic force overcomes the cantilever's elastic restoring force and the beam snaps down), is found by substituting Equation 16 into Equation 15 resulting in:

$$
\begin{aligned}
V_{pi} &= (g_o - d_{pi})\sqrt{\frac{2k_1 d_{pi}}{\epsilon_o A_{sa}}} \\
&= \sqrt{\frac{8g_o^3 k_1}{27\epsilon_o A_{sa}}}
\end{aligned} \tag{17}
$$

where, V_{pi} is the pull-in or switch closure voltage.

The following pull-in voltage equation results when using Osterberg and Senturia first-order fringing fields correction term:

$$V_{\text{piFF}} = \sqrt{\frac{8g_\text{o}^3 k_1}{27\epsilon_\text{o} A_\text{sa}[1 + 0.42\frac{g_\text{o}}{w}]}} \qquad (18)$$

where, V_{piFF} is pull-in voltage adjusted with a first-order fringing fields correction term.

The electrostatic actuation models developed here assume small-angle beam bending and neglect electric field nonuniformity due to beam curvature [113]. During micro-switch operation, the switch's structural layer or beam is assumed to remain in the linear elastic region. As the actuation voltage is increased beyond the pull-in voltage, however, pressure in the electric contact region increases and results in contact material deformation and variations in electric contact area. Relevant contact physics, for micro-switches, is discussed next.

3.6 Contact Mechanics

An understanding of contact mechanics or the study of actual physical contact between two solid bodies is needed to gain insight about electric contacts and contact resistance [7, 67]. In many cases, the physics developed in Hertzian contact mechanics is directly applicable for designing micro switch contacts. There are two primary considerations; 1) how the contact materials deform and 2) the size of the actual contact area.

Contact material deformation is described as being elastic, plastic, or elastic-plastic while actual contact area dictates how electrons are transported through an electrical connection. Electron transport is described as being ballistic, quasi-ballistic, or diffusive. Each of these topics will be further discussed in the following sections. Contact force is discussed next.

3.6.1 Contact Force. Contact force (F_C) is a compressive force that causes material deformation similar to that predicted by conventional material tensile test-

ing. The difference being tensile loads cause material deformation by necking in and compressive loads cause deformation by bulging [21].

Generally, MEMS switches are electrostatic devices that produce low contact forces ranging from tens of μN's up to a few mN's. In micro-switches, contact force is defined by the mechanical switch design.

At pull-in, illustrated by the dashed line in Figure 10, physical contact between the switch's upper (i.e., dimples) and lower electric contacts is first established with minimal contact force. The resulting contact resistance is usually too high for most applications [124]. The contact force can be increased (thereby decreasing the contact resistance) by overdriving the device with increased actuation voltages above V_{pi}. As the micro-switch's actuation voltage is increased, the cantilever beam bends, contact force increases and material deformation causes the contact area to increase. Contact area friction, due to cantilever beam bending, tends to mechanically clean (i.e., "wiping") contaminant films from the electric contact's surface.

After pull-in, the switch was initially modeled as a beam with a fixed end at $x = 0$, a simply supported end at $x = l$, and an intermediately-placed external load (F_a) at $x = a$ as illustrated in Figure 12 [142].

Figure 12   Cantilever beam model with a fixed end at $x = 0$, a simply supported end at $x = l$, and an intermediately-placed external load (F_a) at $x = a$.

Equation 19 defines the spring constant for the model depicted in Figure 12 [142].

$$k_2 = \frac{-Et^3wl^3}{a^2b(3l(b^2 - l^2) + a(3l^2 - b^2))} \tag{19}$$

where, k_2 is the spring constant for a cantilever beam with fixed and simply supported ends.

Unlike the previous beam model, shown in Figure 10, this new beam model is statically indeterminate and an additional equation is needed to supplement the static equilibrium equations (i.e., $\sum F_x = 0, \sum F_y = 0$, and $\sum M = 0$) [89]. Using the principle of superposition, beam tip deflection in Figure 12 is represented by the sum of two statically determinate systems. The first is identical to Figure 10 and the second, depicted in Figure 13, is a beam with fixed end at $x = 0$, a free end at $x = l$, and an end load (R_2) at $x = l$.
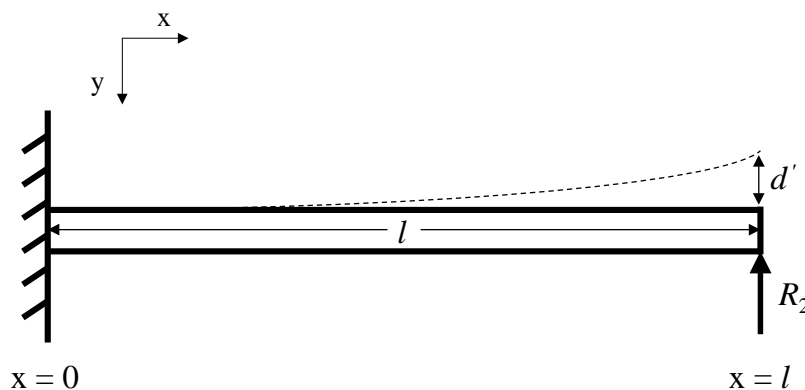
Figure 13   Cantilever beam model with a fixed end ($x = 0$), a free end ($x = l$), and an external end load (R_2).

Equation 20 is the resulting beam bending equation for maximum tip deflection for the beam model in Figure 13.

$$d' = \frac{-R_2l^3}{3EI_z} \tag{20}$$

33

where, d' is the tip deflection for an end-loaded beam and R_2 is the force at the beam's free end.

The final equation, needed to solve the indeterminate system in Figure 31, is found by assuming zero beam tip deflection and no electric contact material deformation (i.e., zero tip deflection), summing Equations 1 and 20, and solving for the reaction force (R_2) results in

$$R_2 = \frac{F_a a^2}{2l^3}(3l - a).$$ (21)

In micro-switches, the beam reaction force is equal to contact force and the externally applied load is equal to electrostatic force. The electrostatic force was modeled by neglecting fringing fields and using a simple, first-order parallel plate capacitor description. Substituting F_C for R_2, Equation 13 for F_a, and $g = g_o - d$, in Equation 21 results in:

$$F_C = \frac{\epsilon_o A_{sa} V^2 a^2}{4l^3 (g_o - d)^2}(3l - a).$$ (22)

where, F_C is the contact force. This simple, static model for micro-switch contact force does not account for beam tip deflection nor material deformation in the electric contacts after switch closure. A more detailed contact force model, presented in section 3.7, results when electric contact material deformation (elastic, plastic or elastic-plastic [24]) and beam tip deflection are considered [28]. Equation 22 is used to analytically determine switch contact force and is valid until the overdriven beam collapses onto the bottom electrode.

Equation 23, the beam collapse voltage, was found using the same procedure as the one used to find the beam's pull-in voltage in section 3.5.

$$V_{cpi} = (g_1 - g_c)\sqrt{\frac{2k_2 d_c}{\epsilon_o A_{sa}}}$$ (23)

34

where, V_{cpi} is the collapse voltage for the pulled-in beam, g_c is the collapse distance, k_2 is the spring constant for the beam depicted by Figure 12, and g_1 is the initial gap under the pulled-in beam. The initial gap under the pulled-in beam is found by equating the ratios of the opposite and adjacent sides of the similar right triangles formed after beam pull-in.

In metal contact micro-switches, device failure is defined by the collapse voltage. At collapse, illustrated by the dashed line in Figure 12, physical contact between the cantilever beam and the drive electrode is established and the device shorts out.

While micro-switch contact force is defined by the mechanical switch design, contact area is defined by contact geometry, surface roughness, elastic modulus, and material hardness. From this description two contact area models, presented next, have developed: 1) the multiple a-spot and 2) the single effective a-spot.

3.6.2 *Contact Area.* The multiple asperity model is based on Greenwood and Williamson's "asperity-based model" for elastic material deformation and Abbott and Firestone's "profilometric model" for plastic deformation [1, 12, 51]. The assumptions used by Greenwood and Williamson follow: 1) rough contact surfaces are isotropic, 2) all surface asperity peaks are spherical with the same radii of curvature, 3) asperity height is randomly distributed, 4) asperities are far apart and independent, 5) material deformation occurs only in the asperities, and 6) no heating occurs. McCool studied anisotropic rough surfaces with randomly distributed elliptical asperities which revealed exceptional agreement with Greenwood and Williamson's simpler model [99]. Greenwood and Tripp showed that two rough contacting surfaces could be modeled by an equivalent single rough surface contacting a flat, smooth surface [50].

In the single effective asperity model, the individual contact spots are close together and their interactions are not independent [11]. In this situation, the effective contact area is defined as the sum, not the parallel combination, of the individual

contact areas. Figure 14 illustrates the multiple a-spot and single effective a-spot models and the notions of apparent (r_a) and effective contact area radii (r_eff).

The contact area radius dictates how electrons are transported through electrical connections. A brief discussion about electric contact material deformation (elastic, plastic, and elastic-plastic) follows.

3.6.3   Contact Material Deformation.   Different regions of electric contact material deformation are highlighted on the generalized stress versus strain plot shown in Figure 15.

3.6.3.1   Elastic.   When two surfaces initially come together, with low contact force, surface asperities (i.e., a-spots) undergo linear elastic deformation. Equations 24 and 25 define contact area and force for a single a-spot as a function of vertical deformation [24].

$$A = \pi R \alpha \tag{24}$$
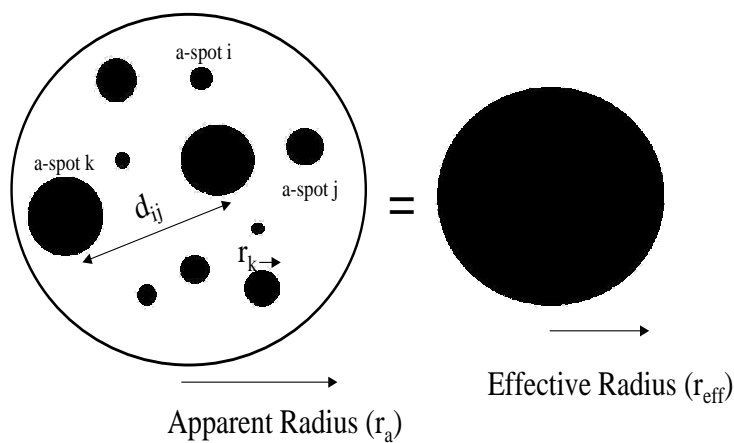
Figure 14   Top view of the multiple asperity (left) and single effective asperity (right) contact area models.
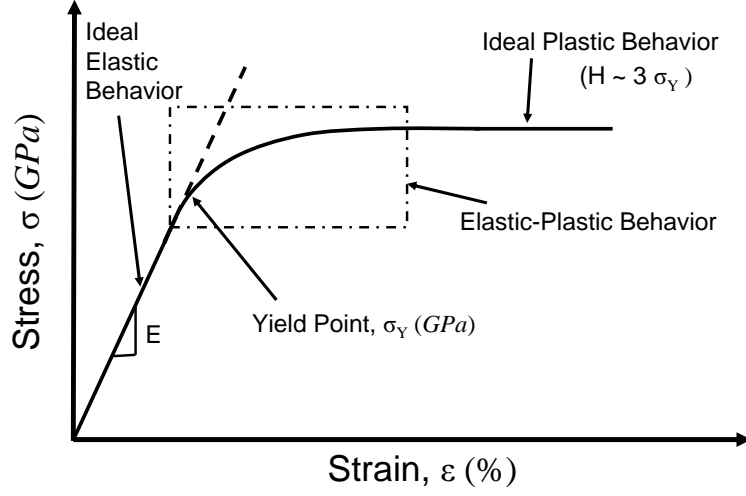
Figure 15   Generalized stress versus strain plot for typical electric contact materials.

where, A is contact area, R is asperity peak radius of curvature, and α is asperity vertical deformation.

$$F_{\mathrm{C}} = \frac{4}{3} E' \alpha \sqrt{R\alpha} \tag{25}$$

where, F_{C} is the normal contact force and E' is the Hertzian modulus derived from

$$\frac{1}{E'} = \frac{1 - \nu_1^2}{E_1} + \frac{1 - \nu_2^2}{E_2} \tag{26}$$

where, E_1 is the elastic modulus for contact one, ν_1 is Poisson's ratio for contact one, E_2 is the elastic modulus for contact two, and ν_2 is Poisson's ratio for contact two.

For circular contact areas (i.e., $A = \pi r^2$), Equations 24 and 25 are related to the contact area radius (r) through Hertz's model [59]:

$$r = \sqrt[3]{\frac{3 F_{\mathrm{C}} R}{4 E'}}. \tag{27}$$

Vertical deformation, in terms of contact force, is derived when $A = \pi r_{\text{eff}}^2$ is substituted into Equation 24, solved for R, and then substituted into Equation 25, resulting in:

$$\alpha = (\frac{3F_{\text{C}}}{4E'r_{\text{eff}}})$$ (28)

where, r_{eff} is the effective contact area radius.

3.6.3.2 Plastic. When deformation is no longer reversible and the applied load is approximately three times the yield stress (σ_Y) or yield point (Y), ideal plastic material deformation begins resulting in a permanent strain after unloading [59, 155]. Plastic material deformation is modeled using Abbott and Firestone's well-known model [1].

This model assumes that contact pressure is sufficiently large and has been applied long enough for all material creep to cease. Single asperity contact area and force are defined using Equations 29 and 30:

$$A = 2\pi R\alpha$$ (29)

$$F_{\text{C}} = HA$$ (30)

where, H is the Meyer hardness of the softer material [24].

Using Equation 30, circular contact area radius is related to contact force through Equation 31 [59]:

$$r = \sqrt{\frac{F_{\text{C}}}{H\pi}}.$$ (31)

Vertical deformation, in terms of contact force, results when Equation 29 is substituted into Equation 30 and solved for α, resulting in:

$$\alpha = \frac{F_{\mathrm{C}}}{2\pi HR}.$$ (32)

An area discontinuity at the transition from ideal elastic to ideal plastic behavior is revealed when the elastic model from section 3.6.3.1 and this plastic model are used together [59]. The CEB model, discussed next, addresses this issue by assuming volume conservation of deformed surface asperities [25].

3.6.3.3 Elastic-Plastic (The CEB Model). Elastic-plastic material deformation refers to when parts of the contact area are plastically deformed but encased by elastically deformed material [145]. The CEB model describes material deformation that occurs between the ideal elastic and ideal plastic regions [21].

Equations 33 and 36 are the CEB model's contact area and force equations, respectively [25].

$$A = \pi R\alpha(2 - \frac{\alpha_c}{\alpha})$$ (33)

where, α_{c} is the critical vertical deformation point, when elastic-plastic behavior begins, given as:

$$\alpha_{\mathrm{c}} = R(\frac{K_{\mathrm{H}} H\pi}{2E'})^2$$ (34)

where, K_{H} is the hardness coefficient (assumed to be equal to 0.6 at the initial onset of plasticity [25]) given as:

$$K_{\mathrm{H}} = 0.454 + 0.41\nu$$ (35)

where, ν is Poisson's ratio.

$$F_C = K_H H A \qquad (36)$$

In the CEB model, a contact load discontinuity exists at the transition from elastic to elastic-plastic material deformation. Kogut and Etison addressed this by using finite element methods to model the elastic-plastic region with normalized contact force and area equations based on Hertzian elastic contact mechanics equations [72]. Chang observed that ideal plastic behavior normally occurred at $3Y$, not $K_Y Y$, where K_Y is the yield coefficient, and updated the CEB model using a linear interpolation [24]. Chang's new force equation for elastic-plastic material deformation is given by Equation 37:

$$F_C = [3 + (\frac{2}{3}K_Y - 3)\frac{\alpha_c}{\alpha}]YA. \qquad (37)$$

where, $K_Y = 1.1282 + 1.158\nu$ [24].

The yield strength for most metals is related to its hardness through Equation 38 [24]:

$$Y = 0.354H. \qquad (38)$$

When K_Y and Equation 38 are substituted into Equation 37, Equation 39 results:

$$F_C = [1.062 + 0.354(\frac{2}{3}K_Y - 3(\frac{\alpha_c}{\alpha}))]HA. \qquad (39)$$

Equations 33 and 39 represent the new CEB model [25] updated with Chang's improvements [24].

For circular areas, Equation 39 is used to relate the contact area radius and the contact force through:

$$r = \sqrt{\frac{F_{\mathrm{C}}}{H\pi[1.062 + 0.354(\frac{2}{3}K_{\mathrm{Y}} - 3(\frac{\alpha_{\mathrm{c}}}{\alpha}))]}}. \qquad (40)$$

Vertical deformation, in terms of contact force, is derived when $A = \pi r_{\mathrm{eff}}^2$ is substituted into Equation 39 and then solved for α, resulting in Equation 41:

$$\alpha = \frac{(0.354)3\alpha_{\mathrm{c}}}{1.062 + 0.354K_{\mathrm{Y}} - (\frac{F_{\mathrm{C}}}{H\pi r_{\mathrm{eff}}^2})}. \qquad (41)$$

Using these material deformation models improved micro-switch contact force equations are derived next.

3.7 Improved Contact Force Equations

In the following section, contact force models that account for beam tip deflection and electric contact material deformation occurring after switch closure are developed. Previous work by this author showed that contact force, bounded by the pull-in and collapse voltages, could be analytically modeled using the beam illustrated in Figure 12 [31]. Equation 22 is the resulting analytic contact force equation. This simple model does not consider beam tip deflection or contact material deformation after the switch is closed.

The new analytic contact force equations, based on an improved cantilever beam model, are derived by accounting for tip deflection [31] and assuming elastic, plastic, and elastic-plastic electric contact material deformation [24]. Euler-Bernoulli beam bending equations, the principle of superposition, material deformation models, and the the single effective a-spot contact area model are used to derive the new equations.

41

In this study, the hemispherically-shaped electric contacts were covered by sputtered thin film contact metals with an average surface roughness of approximately 30 to 50 $\mathring{A}$. These low surface roughness values and the compact material grain structures (≈ 50 nm in diameter), typical of sputtered films, leads to the assumption that the individual contact surface a-spots are not independent and that the single effective a-spot contact area model best describes the contact areas studied here. Next an improved cantilever beam model is presented.

3.7.0.4 Improved Cantilever Beam Models.   In metal contact microswitches, initial switch closure is defined by the pull-in voltage. After pull-in, the switch is now modeled as a deflected beam with a fixed end, a simply supported end, and an intermediate external load (F_a), as illustrated in Figure 16.
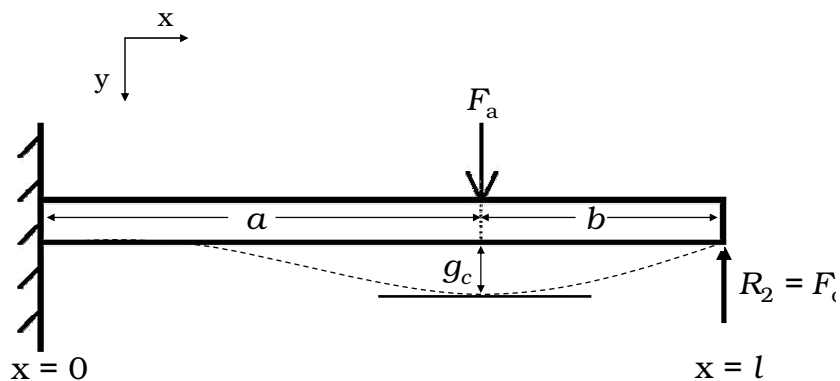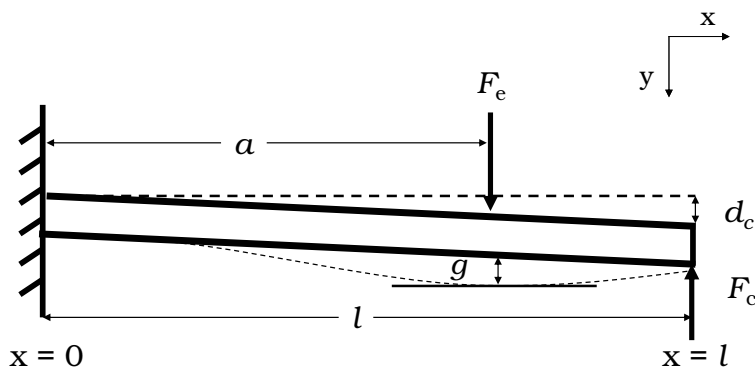

Figure 16   Deflected cantilever beam model with a fixed end at $x = 0$, a simply supported end at $x = l$, and an intermediately placed external load (F_a) at $x = a$.

The external load (F_a), modeled as electrostatic force, was found by neglecting fringing fields and using a first-order parallel plate capacitor description defined by Equation 13.

Like Figure 12, the beam in Figure 16 is statically indeterminate and another equation is needed to supplement the static equilibrium conditions. Using superpo-

sition, beam tip deflection is represented by the sum of two statically determinate systems shown in Figures 10 and 13. The final equation, needed to solve the indeterminate system is found by summing Equations 1 and 20, setting that sum equal to tip deflection (i.e., the distance between the electric contacts), and solving for the reaction force, R_2, resulting in:

$$R_2 = [\frac{F_a a^2}{2l^3}(3l - a)] - [\frac{3EI_z d_c}{l^3}]$$ (42)

where, d_c is the gap between the electric contacts. Substituting F_C for R_2, Equation 13 for F_a, and $g = g_o - d$, in Equation 42 results in:

$$F_C = [\frac{\epsilon_o A_{sa} V^2}{4l^3(g_o - d)^2}a^2(3l - a)] - [\frac{3EI_z d_c}{l^3}]$$ (43)

where, F_C is micro-switch contact force that accounts for beam tip deflection.

During micro-switch operation, the switch's structural layer or beam is assumed to remain in the linear elastic region shown on Figure 15. As the actuation voltage is increased, however, pressure in the electric contact region increases and the contact area changes due to contact material deformation (discussed in section 3.6.3). The effects of contact material deformation are accounted in the beam model shown in Figure 17.

Like Figures 12 and 16, the beam in Figure 17 is statically indeterminate and another equation was needed to supplement the static equilibrium condition. Equation 44 was developed with the same procedure used to determine Equation 43.

$$F_C = [\frac{\epsilon_o A_{sa} V^2}{4l^3(g_o - d)^2}a^2(3l - a)] - [\frac{3EI_z}{l^3}(d_c + \alpha)]$$ (44)
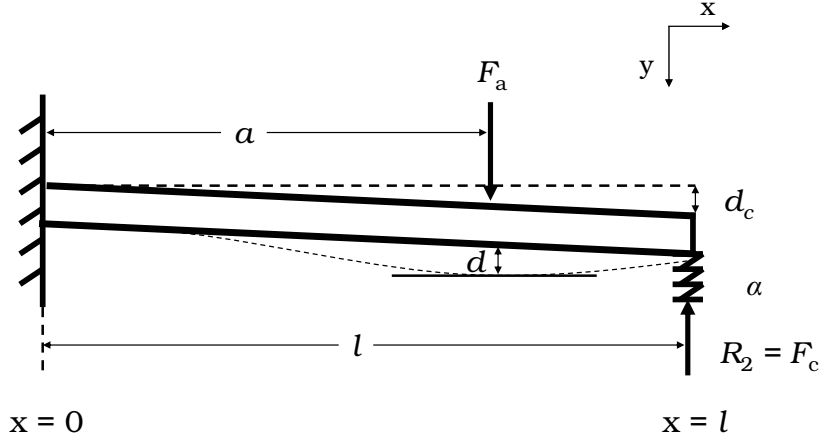
Figure 17   Deflected cantilever beam model with a fixed end at $x = 0$, a simply supported end at $x = l$, an intermediately placed external load (F_a) at $x = a$ and contact material deformation (α) at $x = l$.

The single effective a-spot contact area model and the material deformation models discussed in section 3.6.3 form the basis for the analytic contact force equations derived next.

3.7.0.5 Elastic.   When contact areas deform elastically or upon initial switch closure, a contact force model is derived by substituting Equation 28 into Equation 44 resulting in:

$$
\begin{aligned}
F_{CE} &= [\frac{\epsilon_o A_{sa} V^2}{4l^3(g_o - d)^2} a^2(3l - a)] - \\
&\quad [\frac{3EI_z}{l^3}(d_c + \frac{3F_{CE}}{4E'r_{eff}})].
\end{aligned}
\tag{45}
$$

Solving Equation 45 for F_{CE} results in:

$$
F_{CE} = 2E'r_{eff}[\frac{(\frac{\epsilon_o A_{sa} V^2}{2(g_o - d)^2})a^2(3l - a) - (6E'I_z d_c)}{(9EI_z + 4E'r_{eff}l^3)}].
\tag{46}
$$

44

3.7.0.6 Plastic.   For plastically deforming contact areas a contact force model is derived by substituting Equation 32 into Equation 44 resulting in:

$$
\begin{aligned}
F_{\mathrm{CP}} &= \ [\frac{\epsilon_{\mathrm{o}} A_{\mathrm{sa}} V^2}{4l^3(g_{\mathrm{o}} - d)^2} a^2(3l - a)] - \\
&\quad [\frac{3EI_{\mathrm{z}}}{l^3}(d_{\mathrm{c}} + \frac{F_{\mathrm{CP}}}{2\pi HR})].
\end{aligned}
\tag{47}
$$

Solving Equation 47 for F_{CP} results in:

$$
F_{\mathrm{CP}} = \pi HR[\frac{(\frac{\epsilon_{\mathrm{o}} A_{\mathrm{sa}} V^2}{2(g_{\mathrm{o}} - d)^2})a^2(3l - a) - (6EI_{\mathrm{z}} d_{\mathrm{c}})}{(3EI_{\mathrm{z}} + 2\pi HRl^3)}].
\tag{48}
$$

3.7.0.7 Elastic-Plastic.   For elastic-plastic deformation, a contact force model is derived by substituting Equation 41 into Equation 44 resulting in:

$$
\begin{aligned}
F_{\mathrm{CEP}} &= \ [\frac{\epsilon_{\mathrm{o}} A_{\mathrm{sa}} V^2}{4l^3(g_{\mathrm{o}} - d)^2} a^2(3l - a)] - \\
&\quad [\frac{3EI_{\mathrm{z}}}{l^3}(d_{\mathrm{c}} + \frac{(0.354)3\alpha_{\mathrm{c}}}{1.062 + 0.354K_{\mathrm{Y}} - (\frac{F_{\mathrm{CEP}}}{H\pi r_{\mathrm{eff}}^2})})].
\end{aligned}
\tag{49}
$$

Solving Equation 49 for F_{CEP} results in:

$$
F_{\mathrm{CEP}}^2 + C_1 F_{\mathrm{CEP}} = C_2
\tag{50}
$$

where

$$
C_1 = \frac{H\pi r_{\mathrm{eff}}^2}{2l^3}[\frac{\epsilon_{\mathrm{o}} A_{\mathrm{sa}} V^2 a^2}{2(g_{\mathrm{o}} - d)^2}(3l - a) - (1.062) - (0.354)K_{\mathrm{Y}}]
$$

and

45

$$\begin{aligned} C_2 &= \frac{H\pi r_{\text{eff}}^2}{2l^3}[6EI_{\text{z}}\{3(0.354)\alpha_{\text{c}} + (0.354)K_{\text{Y}}d_{\text{c}} + (1.062)d_{\text{c}}\} \\ &\quad -(\frac{\epsilon_{\text{o}}A_{\text{sa}}V^2a^2}{2(g_{\text{o}} - d)^2})(3l - a)\{1.062 + (0.354)K_{\text{Y}}\}]. \end{aligned}$$

The new contact force equations were derived by assuming elastic, plastic, and elastic-plastic electric contact material deformation [24] and by accounting for beam tip deflection. Beam bending equations, material deformation models, and the principle of superposition were used to derive the improved contact force equations.

Next, macro-switch contact resistance equations are derived using the material deformation models described in Sections 3.6.3.1 and 3.6.3.2.

3.8   Macro-Switch Contact Resistance

Contact resistance (R_{C}), defined by Equation 51, results from making electrical connections and considers the effects of constriction (R_{c}) and contaminant film (R_{cf}) resistances [59]:

$$R_{\text{C}} = R_{\text{c}} + R_{\text{cf}}. \tag{51}$$

Constriction resistance arises because electrical current can only flow through a-spots created during switch closure. When contaminant film resistance is neglected, constriction resistance is equal to contact resistance (i.e., $R_{\text{C}} = R_{\text{c}}$). Constriction resistance, based on diffusive electron transport, is modeled analytically using Equation 52 which is based on Maxwellian spreading resistance theory [59]:

$$R_{\text{c}} = \frac{\rho}{2r_{\text{eff}}} \tag{52}$$

where, ρ is electrical resistivity.

When considering circular contact areas, Equations 53 and 54 are the resulting, well known, macro-switch contact resistance equations that show $R_c \propto F_C^{(-\frac{1}{3})}$ for elastic deformation and $R_c \propto F_C^{(-\frac{1}{2})}$ for plastic deformation [59].

$$R_{cDE} = \frac{\rho}{2} \sqrt[3]{\frac{4E'}{3F_C R}} \tag{53}$$

where, R_{cDE} is contact resistance for diffusive electron transport and elastic material deformation and

$$R_{cDP} = \frac{\rho}{2} \sqrt{\frac{H\pi}{F_C}}, \tag{54}$$

where, R_{cDP} is the contact resistance for diffusive electron transport and plastic material deformation. A brief discussion about constriction size and the resistance resulting from ballistic, quasi-ballistic, and diffusive electron transport follows.

3.9 Electron Transport Theory and Resistance

Micro-switches produce low contact forces which leads to small contact areas. When contact area radius is compared to an electron's elastic mean free path (l_e), the following electron transport regions are defined: ballistic, quasi-ballistic, and diffusive [3]. The ballistic region is when the elastic mean free path is greater than the effective contact radius (i.e., $l_e > r_{eff}$), the quasi-ballistic region is when $l_e \sim r_{eff}$, and the diffusive region is when $l_e \ll r_{eff}$ [3, 95]. The mean free path for most metals is approximately 500 $\mathring{A}$ [3]. Figure 18 illustrates the ballistic and diffusive electron transport regions [3].

Equation 55 or the so-called Sharvin resistance is a semiclassical approximation for resistance when electrons exhibit ballistic transport behavior [95, 141].

$$R_S = \frac{4\rho K}{3\pi r_{eff}} \tag{55}$$
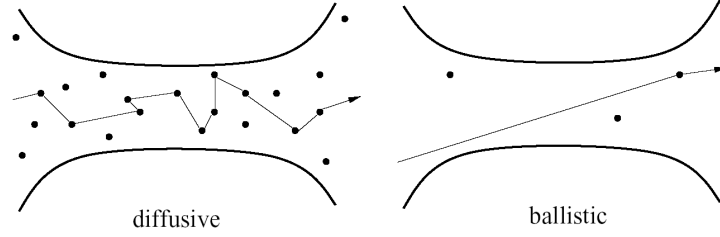
Figure 18   Schematic illustration of diffusive (left) and ballistic (right) electron transport in a conductor [3].

where, R_S is the Sharvin resistance and K is the Knudsen number given as:

$$K = \frac{l_\text{e}}{r_\text{eff}}.$$ (56)

Wexler derived Equation 57 as an interpolation between the ballistic (i.e., Sharvin resistance) and diffusive (i.e., Holm resistance) electron transport regions [167]:

$$
\begin{aligned}
R_\text{W} &= \frac{4\rho K}{3\pi r_\text{eff}}[1 + \frac{3\pi}{8}\Gamma(K)\frac{r_\text{eff}}{l_\text{e}}] \\
&= R_\text{S} + \Gamma(K)R_\text{c}
\end{aligned}
$$ (57)

where, R_W is the so-called Wexler resistance and $\Gamma(K)$ is a slowly varying Gamma function of unity order [167].

A detailed analysis of specific asperity size, spacing, and distribution is required to numerically determine $\Gamma(K)$, the Gamma function needed to interpolate between ballistic and diffusive electron transport. Mikrajuddin et al. derived a well behaved Gamma function that predicts completely ballistic and completely diffusive electron transport when taking the limits of Wexler's interpolation equation ($\Gamma(0) = 1$ and $\Gamma(\infty) = 0$) [104]:

$$\Gamma(K) \approx \frac{2}{\pi} \int_0^\infty e^{-Kx} Sinc(x)\, \mathrm{d}x \qquad (58)$$

where, Sinc(x) is defined as being equal to one when $x = 0$ and equal to $\frac{Sin(x)}{x}$ when $x \neq 0$ [104]. Figure 19 is a plot of Mikrajuddin et al.'s Gamma function that was solved using a recursive Newton-Cotes numerical integration formula.

Micro-contact resistance models, considered next, result when diffusive and ballistic constricted current flow is considered.

3.10   Micro-Switch Contact Resistance

Majumder et al. developed a comprehensive analytic micro-contact resistance model that considered: size-dependent constriction resistance (i.e., ballistic and diffusive electron transport) by using Wexler's interpolating equation, contact material deformation using Hertz's elastic [59], and Chang et al.'s elastic-plastic [25] (i.e., the CEB model) models, multi-asperity based contact areas using Greenwood and Williamson's "asperity-based model" [51], and Holm's single effective asperity contact area model [59]. Contaminant film resistance was neglected in Majumder et al.'s model.
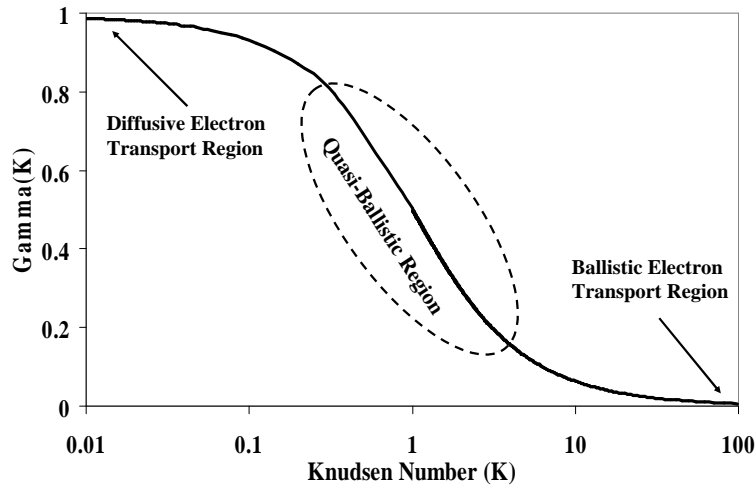
Figure 19   A plot of Mikrajuddin et al.'s derived Gamma function.

Majumder et al. accomplished a semi-qualitative contact surface analysis, based on scanning electron micrograph (SEM) images, to determine approximate asperity size, spacing, and distribution [95]. In addition, a slowly varying Gamma function with the following limits: $\Gamma(0) = 1$ and $\Gamma(\infty) = 0.694$, was used in Wexler's interpolation.

In this dissertation, an analytic micro-switch contact resistance model, based on the the single effective a-spot contact area model, was developed using Hertz's elastic [59], Chang's [24] improvements to the CEB model, Mikrajuddin et al.'s [104] derived Gamma function, and Wexler's interpolation from ballistic to diffusive electron transport [167]. The single effective a-spot contact area model was needed because sputtered electric contact materials with low surface roughness and tightly packed material grain structures were used and the surface asperity independence assumption was no longer valid.

For circular contact areas and elastic material deformation, a contact resistance equation is derived for the ballistic electron transport region by substituting Equation 27 into Equation 55 resulting in:

$$R_{\mathrm{cBE}} = \frac{4\rho K}{3\pi} \sqrt[3]{\frac{4E'}{3F_{\mathrm{C}}R}} \tag{59}$$

where, R_{cBE} is the contact resistance for ballistic electron transport and elastic deformation.

Equation 60, is a micro-switch contact resistance model for elastic deformation, results when Equation 59 and Equation 53 are substituted into Equation 57:

$$R_{\mathrm{cWE}} = R_{\mathrm{cBE}} + \Gamma(K)R_{\mathrm{cDE}} \tag{60}$$

where, R_{cWE} is the Wexler resistance for elastic material deformation.

Equation 61 is a contact resistance equation based on ballistic electron transport and elastic-plastic material deformation and is found by substituting Equation 40 into Equation 55.

$$R_{\text{cBEP}} = \frac{4\rho K}{3\pi} \sqrt{\frac{H\pi[1.062 + 0.354(\frac{2}{3}K_{\text{Y}} - 3(\frac{\alpha_{\text{c}}}{\alpha}))]}{F_{\text{C}}}} \tag{61}$$

where, R_{cBEP} is contact resistance for ballistic electron transport and elastic-plastic material deformation.

Equation 62 is a contact resistance equation based on diffusive electron transport and elastic-plastic material deformation and is found by substituting Equation 40 into Equation 52.

$$R_{\text{cDEP}} = \frac{\rho}{2} \sqrt{\frac{H\pi[1.062 + 0.354(\frac{2}{3}K_{\text{Y}} - 3(\frac{\alpha_{\text{c}}}{\alpha}))]}{F_{\text{C}}}} \tag{62}$$

where, R_{cDEP} is contact resistance for diffusive electron transport and elastic-plastic material deformation.

Equation 63, the new micro-contact resistance model for elastic-plastic deformation, results when Equation 61 and Equation 62 are substituted into Equation 57:

$$R_{\text{cWEP}} = R_{\text{cBEP}} + \Gamma(K)R_{\text{cDEP}} \tag{63}$$

where, R_{cWEP} is the Wexler resistance for elastic-plastic material deformation. The complete micro-switch contact resistance model consists of using Equation 60 for elastic deformation and Equation 63 for elastic-plastic deformation (i.e., after α_{c}). Contaminant films are discussed next.

3.11 Contaminant Films

Contaminant films are normally present on all electric contact surfaces and the resistance due to contaminant layers, depicted in Figure 20, can be modeled using Equation 64 [59, 156]:
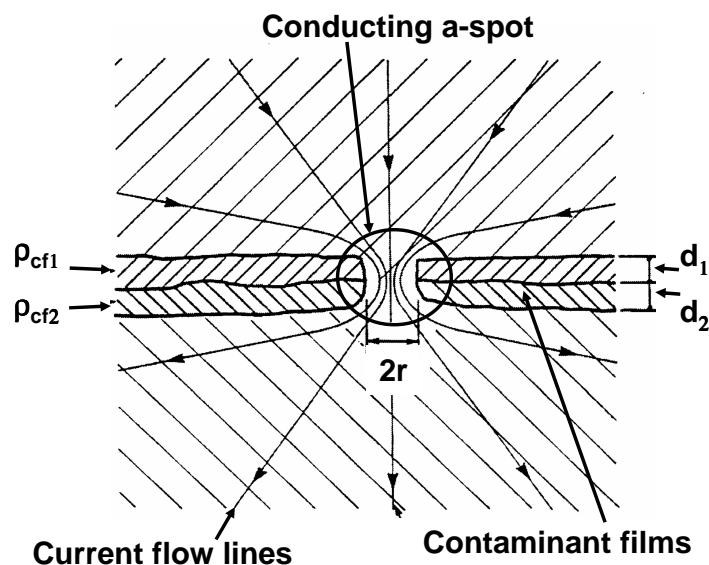
Figure 20   Illustration of contaminant films, surrounding a conducting a-spot, at the interface of a pair of electric contacts [156].

Figure 20 shows a single conducting a-spot at the interface of a pair of electric contacts. Each of the contacts has a surface film of known thickness and resistivity.

$$R_{\text{cf}} = \frac{d_1 \rho_{\text{cf1}} + d_1 \rho_{\text{cf2}}}{A_{\text{cf}}} \tag{64}$$

where, d_1 is the contaminant film thickness on contact one, ρ_{cf1} is the contaminant film resistivity on contact one, d_2 is the contaminant film thickness on contact two, ρ_{cf2} is the contaminant film resistivity on contact two, and A_{cf} is the effective area of the contact that is covered by the contaminant film.

Electric contacts can be mechanically or electrically "cleaned" prior to use. Mechanical cleaning involves "wiping" the contacts together to physically puncture

or move away contaminants and needs to be incorporated into the switch's mechanical design. Electrical contact cleaning involves using an electric potential across the switch contacts to induce a micro-arc and burn off contaminants prior to switch closure [59, 135].

Material transfer between the electric contacts can result from electrical cleaning with a micro-arc. Material transfer is normally in the direction of positive to negative contact [59, 54]. Under the influences of an arc, however the direction of material transfer is reversed and excess contact material left on the positive contact [54]. A hypothesis for material transfer in thin film electric contact systems is based on joule heating during current flow which causes pieces of softened contact material to pull away and break off resulting in material transfer. Contact materials should ideally have melting points high enough to avoid material transfer due to softening [54].

Next, a brief discussion about binary metal alloys and their effects on contact resistance.

3.12   *Binary Metal Alloys*

According to the Metals Handbook, "no metal has all the desired properties required to accomplish the objectives of different contact applications" [54]. Intuitively, this makes good sense because requirements (i.e., service life, load, etc.) change for different applications. Desired electric contact properties included: low resistivity, high thermal conductivity, no insulating oxides or sulfides, nominal hardness (i.e., higher than gold), and a high melting point.

Although most metals have been tried, silver and its alloys, because of their superior electrical, mechanical and thermodynamic properties, are the most widely used macro-switch electric contact materials [59, 144]. One drawback to using silver is that it tarnishes in the presence of sulfur and forms mechanically robust surface sulfide layers. Although not a big problem for macro-switches, where many newtons

53

of contact force are available to penetrate nonconductive surface layers, in micro-switches where contact force is often limited to hundreds of μNs, pure silver or alloys with high percentages of silver are not suitable electric contact materials.

Gold contacts, on the other hand, are widely used in micro-switches due to its low resistivity, high oxidation resistance and easy integration with available device fabrication processes. Gold, however, is a very soft metal, has a low melting point and adsorbs carbonaceous layers. These properties make gold electric contacts prone to erosion and wear [54]. Although gold is a soft metal, it can be hardened using alloying elements or solutes such as nickel (Ni), cobalt (Co), palladium (Pd), silver (Ag) or platinum (Pt) to help minimize contact wear and erosion [54]. The resulting alloys are best suited for low current applications because of their relatively low melting points [54]. Au-Pd, Au-Ag, and Au-Pt binary alloys, discussed in detail in chapter IV, were investigated during this dissertation.

Phase diagrams and bulk resistivity values were used to further investigate binary alloys and determine specific gold alloy compositions. A wealth of knowledge, pertinent for designing MEMS switches, is gained by using binary alloy phase diagrams [112]. Important considerations, specific for micro-switches, will be discussed. Using phase diagrams, single-phase alloys and miscibility regions are located. Single phase alloys (i.e both elements have the same crystal structure) are desired because metal alloy crystal structures in these areas do not physically change with elevated temperature. Miscibility gaps or two-phase regions (i.e., mixture of two different phases) should be avoided because the distribution of each phase, across the micro-contact, can not reliably predicted during device fabrication. Brittle, highly resistive, intermetallic compounds (i.e., crystal structure that may be different from either element) should also be avoided to ensure reliable device fabrication.

Most binary metal alloys obey Nordheim's rule where the relationship between resistivity and alloy composition is parabolic and a tradeoff situation exists between bulk resistivity alloy composition [54]. Often times, material hardness is also in-

creased with alloying [54, 137]. These engineering tradeoff situations lead to the idea of using Au alloy micro-switch contact metals.

Schimkat tested gold-nickel alloy (Au-(5%)Ni) macro-switch electric contacts under low contact force ($100 - 600 \ \mu N$) conditions [135]. He theorized that Au-Ni alloys were useful micro-relay contact materials. In Figure 21, however, the Au-Ni phase diagram shows two stable alloy phases across the entire composition range below $810.3°C$.
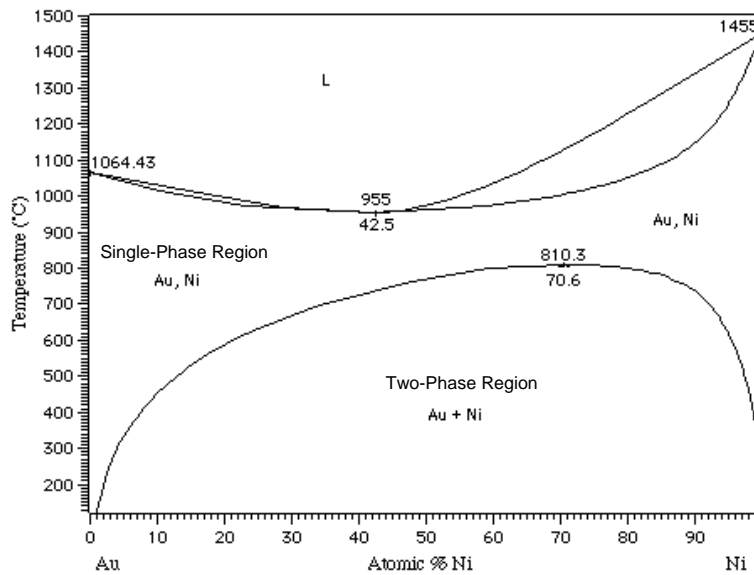
Figure 21   Equilibrium binary alloy phase diagram for gold-nickel alloys [112].

The two-phase region, shown in Figure 21, indicates that micro-switch electric contacts made from Au-Ni alloys will contain unpredictable amounts of each material phase. This is problematic because only certain percentages of each phase will result in low resistivity materials (i.e., the alloy Schimkat tested). This hypothesis is supported by erratic bulk resistance ratios for Au-Ni alloys, found in the CRC Handbook, that do not follow Norheim's rule [137]. The alloy composition that Schimkat tested was a stable, two-phase material. Due to variations in metal alloy deposition processes (i.e., temp, pressure, etc.), however, this precise two-phase Au-Ni alloy, with a predictable amount of each material phase, is difficult to reliably duplicate

(especially on micro-sized contact areas) and therefore incorporate into micro-switch fabrication. Next, a brief discussion about relevant RF modeling and RF effects.

3.13 S-Parameters

The ability to switch RF and microwave signals between components and systems is an important aspect of RF and microwave systems design. Important RF switch design considerations are isolation, insertion loss (IL), intermodulation distortion (IMD), bandwidth, and skin depth [14, 106, 120, 124].

The scattering matrix or S-parameters are used to define coefficients that relate incident and reflected voltage waves in networks and are used to quantify isolation and insertion loss [121]. In a non-reciprocal, linear, passive, 2-port network there are four elements in the S-parameter matrix. Element S_{11} is called the input reflection coefficient, S_{12} the reverse transmission coefficient, S_{21} the forward transmission coefficient, and S_{22} the output reflection coefficient [14, 120]. Insertion loss and isolation can be defined using either S_{12} or S_{21} (depending on which port is defined as the input) when the micro-switch is open or closed, respectively.

Using a simple, first order model with port 1 as the input and port 2 as the output, isolation and IL can be found for series contact switches using Equations 65 and 66, respectively [49].

$$S_{12} = \frac{j\omega C_{\text{off}} 2Z_{\text{o}}}{1 + j\omega C_{\text{off}} 2Z_{\text{o}}} \tag{65}$$

where, $\omega = 2\pi f$ and f is the signal frequency in hertz, C_{off} is the off or open switch capacitance, and Z_{o} is the transmission line characteristic impedance.

$$S_{21} = \frac{2Z_{\text{o}}}{R_{\text{o}} + 2Z_{\text{o}}} \tag{66}$$

where, R_{o} is the closed switch resistance.

For open or unactuated RF switches, high isolation or minimal coupling of signal from the input to the output port is desirable. For a closed or actuated switch, low insertion loss or maximum coupling from the input to the output ports is needed to minimize signal loss.

S-parameters are usually expressed in decibels using Equation 67 [120].

$$S_{\text{dB}} = 20 Log |S_{\text{xx}}| \tag{67}$$

where, S_{dB} is an S-parameter expressed in dB and S_{xx} is an S-parameter expressed as the ratio of incident and reflected voltage waves.

More detailed S-parameter and high frequency constriction resistance models have been developed by Rebeiz [124], Lavers and Timsit [84], Malucci [97], Dervos [43], and Kwiatkowski et al. [82]. For example, Equation 68 is a constriction resistance equation, derived by Kwiatkowski et al., based entirely on S-parameters [82].

$$R_{\text{c}} = 2Z_{\text{o}} \sqrt{\frac{|S_{11}||S_{22}|}{|S_{12}||S_{21}|}} \tag{68}$$

3.14 Summary

A review of the necessary theory for an overall understanding of RF MEMS metal contact switches and the direction of this research was presented. Specifically, MEMS fabrication, electrostatic actuation, contact physics, contact force and resistance models, contaminant films, and S-Parameters were discussed. After completing the design, fabrication, and some limited testing, the improved beam model (section 3.3.2) [100], the parallel plate capacitor models (section 3.4.2) [113], the contact force models (section 3.7) [28], and the contact resistance models (section 3.10) [33] were investigated further. The results of this investigation are presented in chapter VII. Chapter IV presents a binary alloy selection methodology and the

specific binary alloy compositions investigated in this dissertation. The ternary alloy is discussed in chapters VI and VII.

IV. Electric Contact Materials Study

This chapter outlines the methodology for selecting binary metal alloy electric contact materials suitable for RF MEMS switches. The general steps of this procedure follow: 1) select candidate alloys by reviewing binary metal alloys, utilizing equilibrium binary alloy phase diagrams and tabulated binary alloy bulk material resistivity data, 2) pick an appropriate thin film deposition method and fabricate test specimens, 3) measure important thin film material properties and 4) predict contact resistance performance using a suitable model. The novel contributions to the MEMS field, discussed in this chapter, are the overall binary metal alloy selection methodology for micro-switch electric contacts, a co-sputtering fabrication technique for depositing alloy contact metals, and the measured thin film metal (i.e Au, Ag, Pd, and Pt) and alloy (i.e., Au-Pd, Au-Pt, and Au-Ag) material properties.

4.1 Candidate Alloys

The following hypothesis for incorporating metal alloy contacts was developed: 1) use single-phase, miscible (i.e., alloy elements are completely soluble in each other) binary alloys, 2) avoid intermetallic compounds, 3) avoid materials combinations that tarnish, oxidize, or form robust surface films, 4) choose an alloy deposition technique compatible with available micro-switch fabrication processes. A careful study of available binary alloy phase diagrams [112] and bulk material resistivity values, found in the CRC Handbook of Electrical Resistivities of Binary Metallic Alloys, indicated that Au-Pd, Au-Ag, and Au-Pt alloys were viable micro-switch electric contacts candidates [137].

Figures 22, 23, and 24 are the equilibrium binary alloy phase diagrams for Au-Pd, Au-Ag and Au-Pt alloys, respectively. The Au-Pd phase diagram shows one stable alloy phase below $1064.43°C$ and three known regions where intermetallic

compounds form. Single phase Au-Pd alloys normally result when using Pd concentrations of less than $\approx 10at\%$.
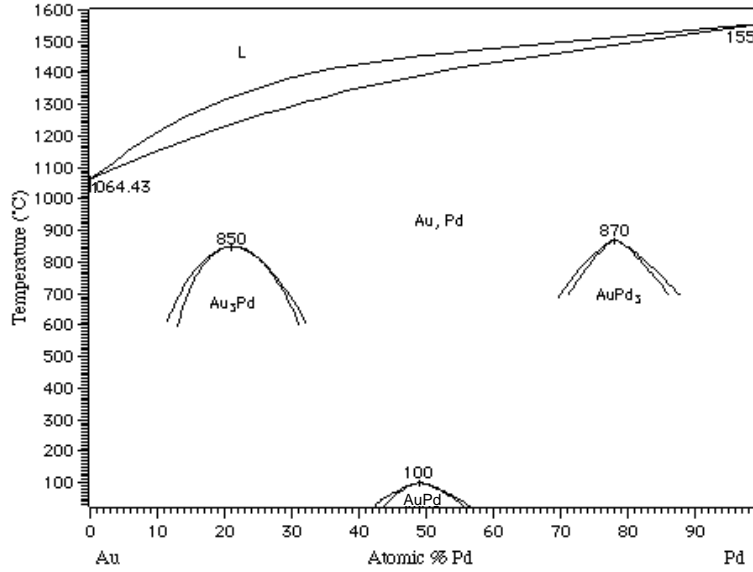
Figure 22   Equilibrium binary alloy phase diagram for gold-palladium alloys [112].

The Au-Ag phase diagram shows one stable material phase for all alloy compositions. The melting temperature for Au-Ag alloys increases from $961.93°C$ to $1064.00°C$ as the the Au concentration increases from 0 to 100at%. Miscible Au-Ag alloys with Ag concentrations less than $\approx 30at\%$ are less likely to tarnish in the presence of sulfur [54]. Based on this decreased likelihood of tarnishing, only Au-Ag alloys with less than $\approx 15at\%$ silver content were investigated in this study.

The Au-Pt phase diagram shows two stable phases below $1260°C$ but only with platinum (Pt) concentrations greater than $\approx 15at\%$. Single-phase Au-Pt alloys result for Pt concentrations of less than $\approx 15at\%$.

There were several other possible metals that could potentially be alloyed with gold, platinum, or palladium to form binary alloys useable in micro-switch electric contacts. The most notable are rhenium (Re), ruthenium (Ru), Rhodium (Rh), iridium (Ir), copper (Cu), Ni, and Co [124]. Gold-rhenium (Au-Re) and gold-iridium (Au-Ir) alloys were not considered, in this study, because alloy phase di-
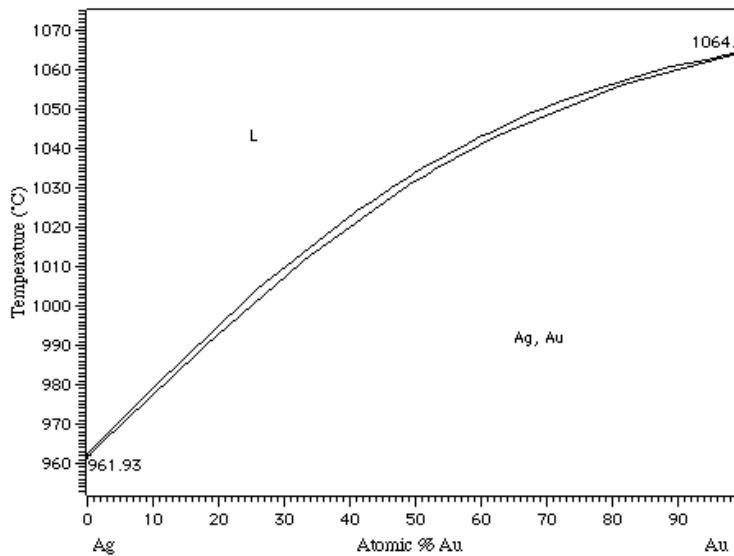
Figure 23   Equilibrium binary alloy phase diagram for gold-silver alloys [112].
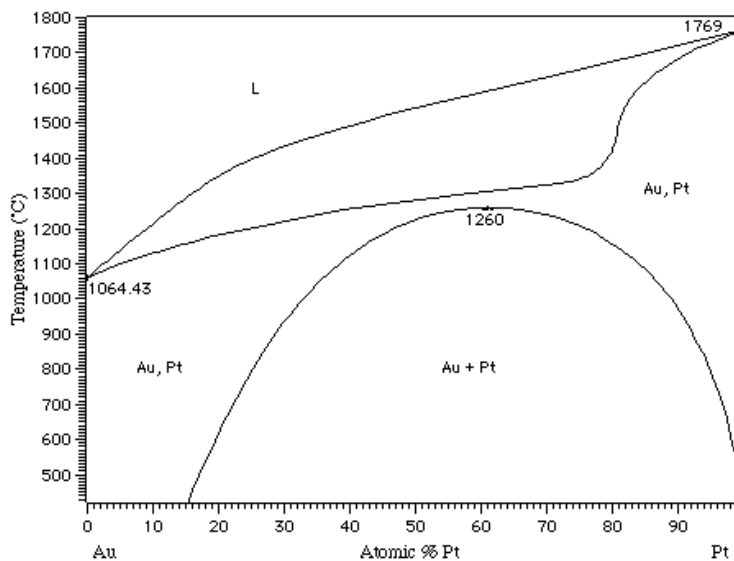
Figure 24   Equilibrium binary alloy phase diagram for gold-platinum alloys [112].

agrams were not available for these material combinations [112]. Phase diagrams for gold-rhodium (Au-Rh), platinum-rhodium (Pt-Rh), platinum-iridium (Pt-Ir), palladium-ruthenium (Pd-Ru), and platinum-palladium (Pt-Pd) alloys were available, however, the bulk material resistivities, found in the CRC Handbook, were

much greater than those for the Au-Pd, Au-Ag and Au-Pt alloys [137]. Phase diagrams were also available for gold-ruthenium (Au-Ru), platinum-rhenium (Pt-Re), platinum-ruthenium (Pt-Ru), palladium-rhenium (Pd-Re), palladium-rhodium (Pd-Rh), palladium-iridium (Pd-Ir), rhenium-ruthenium (Re-Ru), ruthenium-iridium (Ru-Ir), and rhodium-iridium (Rh-Ir) alloys, however, bulk material resistivities were not available for these alloys [137]. Gold-copper (Au-Cu) binary alloys were not considered, in this study, because alloys with high concentrations of Cu have a tendency to form surface films while alloys with low concentrations of Cu are known to form intermetallic compounds [112]. A gold-platinum-copper (Au-Pt-Cu) ternary alloy was investigated and the details are discussed in chapter VII. Gold-cobalt (Au-Co) alloys were also not considered, in this study, because, like gold-nickel (Au-Ni) alloys, the two-phase region extends across the entire alloy composition spectrum making reliable, repeatable thin film deposition difficult [112].

In addition, gold-titanium (Au-Ti) alloys were not used as contact metals in this study. Although titanium (Ti) is a popular adhesion metal for gold, particularly for lower micro-switch contacts, it is not a suitable electric contact metal due to the numerous miscibility gaps and intermetallic compounds, shown on Figure 25, that are always present whenever Au is deposited directly onto Ti.

For example, with a composition of 49at% Au and 51at% Ti, the material physically changes from the β-Au-Ti alloy to the γ-Au-Ti alloy when the temperature increases above $\sim 590°C$. Similar metallurgical changes can occur when the gold top layer is mechanically worn away due to material transfer resulting from contact area heating (i.e., joule heating due to current flow).

Binary metal alloy literature [65, 105, 164], equilibrium binary alloy phase diagrams [112], and bulk material resistivity values [137] are important tools for evaluating potential material combinations for MEMS switch electric contacts. In addition to using single-phase binary alloys, avoiding intermetallic compounds, and materials that tarnish, oxidize, or form robust surface films, the alloy deposition
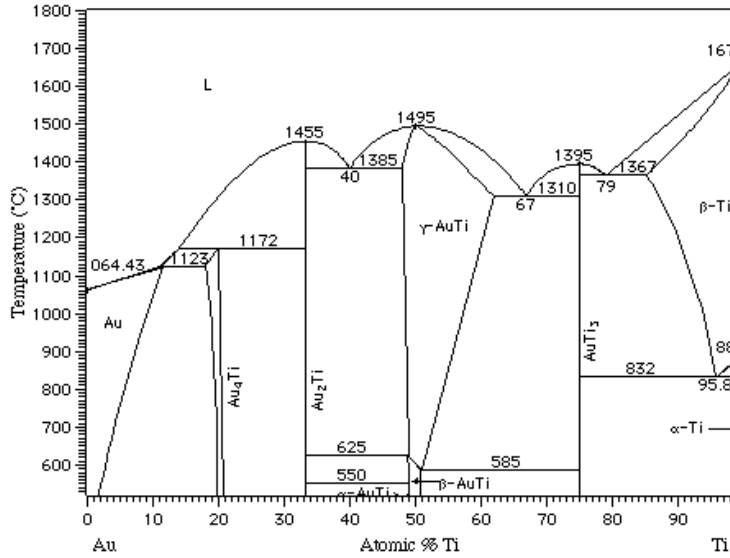
Figure 25   Equilibrium binary alloy phase diagram for gold-titanium alloys [112].

method must be compatible with the micro-switch fabrication process [128]. This is discussed next.

4.2   Thin Film Deposition

Thin metal films are routinely deposited using either physical vapor deposition (PVD) or chemical vapor deposition (CVD) methods [128, 64, 91]. The PVD techniques of sputtering and evaporation, accomplished under vacuum, can be used for depositing metal alloy thin films. Alloy deposition using CVD is more difficult because of its precise stoichiometric dependence.

In general, evaporative metal deposition involves heating a material to its melting point and allowing the vaporized atoms, traveling in straight lines, to impinge and condense on a target substrate. Alloys are deposited by using either a single alloyed material container or by using co-evaporation where two different materials are heated simultaneously. Precise composition control is difficult when evaporating a single container alloy because different metals have different vapor pressures and therefore different evaporation rates. When using co-evaporation obtaining uniform

alloy composition, across the target substrate, is difficult because of straight line evaporation patterns and vapor phase material scattering [128].

Sputtering is a process where inert gas ions (i.e., Argon (Ar)) are used to bombard a material target in the presence of an electric field. Once the ions hit the target with sufficient energy, material is dislodged due to an exchange of momentum. The dislodged material is then transported to the substrate ballistically [91]. Like evaporation, alloys can be sputter deposited using either alloyed material targets or by co-sputtering individual materials. For alloyed targets, the sputtered vapor corresponds to the target's composition. When co-sputtering, the individual target vapors correspond to the composition percentages of the deposited alloy. Unlike evaporation, target deposition rates (i.e., and therefore alloy compositions) are controlled by cathode power settings and are not dependent on the partial pressure of each alloying element.

In this work, a Denton Discovery-18 sputtering system was used to co-sputter the thin metal alloy films. Standard operating procedures were followed to characterize the deposition rates for each of the sputter targets needed to deposit alloys. Deposition rates were determined through an iterative process of choosing a chamber pressure (to minimize film stress), setting the cathode power for an estimated film thickness, verifying film thickness using a Tencor P-10 surface profiler, and finally adjusting the cathode power level. With this data, deposition rate versus cathode power was plotted and and curve fitted. The curve fit equations were then used to find a quiescent cathode power level setting for depositing each alloy film. Three different miscible Au-Pd, Au-Ag and Au-Pt alloy test specimens (≈ 500 $\text{\AA}$-thick) were co-sputtered onto three inch silicon (100) test wafers using this procedure. Table 2 summarizes the predicted alloy compositions, cathode power settings, and chamber pressures used when depositing the thin film alloys.

Material property testing was accomplished next to verify that miscible single-phase alloys were deposited and that two-phase regions and intermetallic compounds

64

Table 2   Predicted alloy compositions, cathode power settings, and chamber pressures used for depositing the thin film alloys.

Predicted	Power Settings (W)	Pressure ($millitorr$)
Au-(1at%)Pt	Au/250 - Pt/5	5.24
Au-(2at%)Pt	Au/250 - Pt/10	5.24
Au-(5at%)Pt	Au/250 - Pt/26	5.22
Au-(1at%)Pd	Au/250 - Pd/2	2.54
Au-(3at%)Pd	Au/250 - Pd/9	2.56
Au-(5at%)Pd	Au/250 - Pd/15	2.55
Au-(5at%)Ag	Au/250 - Ag/7	2.36
Au-(7at%)Ag	Au/250 - Ag/10	2.36
Au-(10at%)Ag	Au/250 - Ag/15	2.34

were avoided. Thin film material properties, not available in the open literature, were measured directly to ascertain important electrical and mechanical properties.

4.3   Material Property Testing

A premise of this study was that suitable MEMS switch electric contacts were realizable when using miscible, single-phase alloys and avoiding two-phase regions and intermetallic compounds. X-ray photoelectron spectroscopy (XPS) and X-ray diffraction (XRD) were used to evaluate microstructure and composition of co-sputtered metal alloy films ($\approx$ 500 $\mathring{A}$ thick). A detailed crystallography study and compositional analysis were not performed. XPS was used to compare actual atomic composition percentages to those predicted prior to deposition and XRD was used to measure 2θ peaks (θ is the angle of the incidence and 2θ is the measured angle of diffraction) which correspond to d-spacing or interatomic spacing for specific materials. Nanoindenting and four-point probe resistance measurements were used to assess thin film hardness and resistivity, respectively and a surface profiler was used to evaluate surface roughness.

Using standard operating procedures, XPS was used to verify the alloy composition of each test specimen and investigate the contaminant layers. For example,

the composition of the Au-(1at%)Pt alloy film was approximately 97.8at% Au and 2.2at% Pt. The alloy composition measurements for the remaining candidate alloys are presented in Table 3.

Table 3   XPS composition measurements for the Au-Pt, Au-Pd, and Au-Ag alloy test specimens.

Predicted	XPS measured
Au-(1at%)Pt	Au-(2.2at%)Pt
Au-(2at%)Pt	Au-(6.3at%)Pt
Au-(5at%)Pt	Au-(10.1at%)Pt
Au-(1at%)Pd	Au-(0.7at%)Pd
Au-(3at%)Pd	Au-(1.5at%)Pd
Au-(5at%)Pd	Au-(3.7at%)Pd
Au-(5at%)Ag	Au-(2.1at%)Ag
Au-(7at%)Ag	Au-(5.2at%)Ag
Au-(10at%)Ag	Au-(6.4at%)Ag

All of the candidate alloy test specimens were within the single-phase ranges shown on the phase diagrams (Figures 22, 23 and 24).

A contaminant layer approximately 20 to 40 Å-thick, consisting of carbon (C) and oxygen (O), was present on each of the test specimens. This contaminant layer was consistent for all the samples exposed to laboratory ambient and is not indicative of contamination introduced during deposition or sample mishandling. XPS depth profiling (i.e., calibrated sputter cleaning) was used to determine the thickness and composition of the contaminant layer. Sulfur (S) was not present on any of the samples.

Using standard operating procedures, XRD was used to measure the crystal orientations (i.e., 2θ peaks) of all the polycrystalline test specimens and evaluate whether single-phase alloy, two-phase alloy, or intermetallic compounds were deposited. The (111) 2θ peaks, for sputtered Au, Pt, and Au-(2.2at%)Pt films, were approximately 38.30 °, 39.92 ° and 38.40 °, respectively. Since the alloy film had only a single (111) 2θ line (versus a single (111) peak for each alloy element or one peak

for each alloy phase), shifted slightly toward the Pt line, intermetallic compounds were not present. The (111) 2θ peaks, used to evaluate all of the candidate alloys, are presented in Table 4.

Table 4 XRD (111) 2θ peaks for the Au-Pt, Au-Pd, and Au-Ag alloy test specimens.

Predicted	XRD 2θ peaks (°)
Au	38.30
Pt	39.92
Pd	40.32
Ag	38.42
Au-(2.2at%)Pt	38.42
Au-(6.3at%)Pt	38.36
Au-(10.1at%)Pt	38.46
Au-(0.7at%)Pd	38.36
Au-(1.5at%)Pd	38.40
Au-(3.7at%)Pd	38.42
Au-(2.1at%)Ag	38.39
Au-(5.2at%)Ag	38.40
Au-(6.4at%)Ag	38.40

All of the polycrystalline thin film alloy specimens were tested using XRD and showed no signs that two-phase alloy or intermetallic compounds were deposited. The measured Au-Ag alloy 2θ peaks, however, were only slightly offset from the Ag sample's 2θ peak and difficult to distinguish between. This was most likely due to Au and Ag having very close d-spacings and also due to the complete miscibility of Au-Ag alloys as shown in Figure 23.

Using standard operating procedures, material hardness was measured with an MTS Nanoindentor IIs. Ten indents were measured on each of the test specimens. Substrate effects were minimized by limiting the indent depth to approximately 10-15at% of film's overall thickness [158]. Table 5 presents the hardness data for the sputtered Au-Pt, Au-Pd, and Au-Ag alloy test specimens. Au, Pt, Pd, and Ag measurements are provided for comparison.

Table 5   Nanoindentor IIs hardness (H) measurements for Au, Pt, Pd, Ag, Au-Pt, Au-Pd and Au-Ag test specimens.

Material	H (GPa)	StdDev (GPa)
Au	1.77	0.18
Pt	3.55	0.25
Pd	2.87	0.22
Ag	1.31	0.09
Au-(2.2at%)Pt	1.69	0.11
Au-(6.3at%)Pt	2.19	0.26
Au-(10.1at%)Pt	1.98	0.10
Au-(0.7at%)Pd	1.64	0.07
Au-(1.5at%)Pd	1.87	0.21
Au-(3.7at%)Pd	1.96	0.13
Au-(2.1at%)Ag	1.82	0.10
Au-(5.2at%)Ag	1.68	0.14
Au-(6.4at%)Ag	1.73	0.16

A standard four-point probe system consisting of an Alessi (Cascade) CPS-06 probe station, a Fluke 8842A multimeter, and an HP 6181B DC current source was used to collect thin film voltage measurements using standard operating procedures. The applied current was set to 0.05 mA and the resulting voltage measurements were converted to resistivity using Equations 69 and 70:

$$R_\mathrm{s} = 4.53\frac{V}{I} \tag{69}$$

where R_s is the sheet resistance, V is the measured voltage, and I is the applied current,

$$\rho = \frac{R_\mathrm{s}}{t_\mathrm{film}} \tag{70}$$

where t_film is the film's thickness [15].

Ten evenly spaced measurements were collected, across each of the three inch metal and alloy test wafers, to ensure uniform material deposition. Table 6 summa-

rizes the resistivity data for the Au, Pt, Pd, Ag, and the Au-Pt, Au-Pd, Au-Ag alloy films.

Table 6   Resistivity measured using the four-point probe method for the Au, Pt, Pd, Ag, and the Au-Pt, Au-Pd, Au-Ag alloy test specimens.

Material	Resistivity ($\mu\Omega - cm$)	StdDev ($\mu\Omega - cm$)
Au	3.93	0.0004
Pt	13.88	0.0015
Pd	13.75	0.0006
Ag	1.78	0.0001
Au-(2.2at%)Pt	5.83	0.0006
Au-(6.3at%)Pt	7.17	0.0001
Au-(10.1at%)Pt	10.60	0.0015
Au-(0.7at%)Pd	5.14	0.0005
Au-(1.5at%)Pd	5.70	0.0003
Au-(3.7at%)Pd	6.37	0.0002
Au-(2.1at%)Ag	5.28	0.0006
Au-(5.2at%)Ag	5.69	0.0015
Au-(6.4at%)Ag	6.20	0.0004

Lastly, surface roughness root mean square (RMS) values between 30 - 50 $\overset{\circ}{A}$, typical of sputtered metal films, were measured for each of the test specimens using a Tencor P-10 surface profiler and standard operating procedures [128].

Once miscible alloy deposition was verified and the hardness and resisivity measurements accomplished, a contact resistance metric, described next, was used to determine which alloy was best suited for incorporation into the micro-switch fabrication process.

4.4   Contact Resistance Performance Prediction

Holm's contact resistance model based on plastic material deformation, presented in chapter III, Section 3.8, was used as the performance metric for selecting the top alloy candidates. Table 7 is a summary of predicted contact resistance, calculated using Equation 54, measured hardness (Table 5) and measured resistivity (Table 6) values, for the candidate alloy electric contact materials. A contact resis-

tance prediction for sputtered gold electric contacts is also provided for comparison. The contact surfaces were assumed to be "clean" (i.e., free of contaminate film layers) with a normally applied contact force of 50 μN.

Table 7   Minimum contact resistance (R_c) predictions for candidate electric contact materials.

Metal/Alloy	Predicted Min R_c (Ω)
Au	0.21
Au-(2.2at%)Pt	0.30
Au-(6.3at%)Pt	0.42
Au-(10.1at%)Pt	0.59
Au-(0.7at%)Pd	0.26
Au-(1.5at%)Pd	0.31
Au-(3.7at%)Pd	0.35
Au-(2.1at%)Ag	0.28
Au-(5.2at%)Ag	0.29
Au-(6.4at%)Ag	0.32

Observe from Table 5 that Au-(6.3at%)Pt, Au-(3.7at%)Pd, and Au-(2.1at%)Ag alloys have the highest measured hardness values for each of the alloy groups (i.e., Au-Pt, Au-Pd, and Au-Ag). In addition, each of these compositions have higher measured hardness than Au and have predicted contact resistance (Table 7) that is comparable to Au. Based on this, the harder alloys (Au-(6.3at%)Pt and Au-(3.7at%)Pd) were used as contact materials in MEMS test structures (i.e., micro-switches) to investigate the feasibility of using alloy electric contacts to validate the procedure for selecting alloy contact metals.

4.5   Summary

A selection methodology for binary metal alloy micro-switch electric contact materials was presented in this chapter. Specifically, candidate binary alloys were investigated, thin film deposition systems reviewed, and thin film material property testing was accomplished. Using this information and a contact resistance performance metric specific binary alloy contact alloys were selected. In chapter V, the

mechanical design aspects of DC-only micro-switches with Au electric contacts were analyzed using analytic equations, finite element method (FEM) design tools, and experimental results.

V. Modeling and Design

The following chapter outlines the design analysis of an electrostatic, cantilever-style, DC-only micro-switch using analytic equations, Coventorware (i.e., a finite element methods design tool), and measured results. The results of this analysis were used to model and design RF-testable cantilever-style micro-switches. The contribution of this study is the validation of using simple analytic equations as micro-switch design tools.

5.1 Background

Initial test structures, for this dissertation, were fabricated using an Air Force Research Laboratory (AFRL) first generation metal contact photolithography mask set (i.e., SNM01 designs) and a modified AFRL/SND baseline fabrication process. The details of the modified fabrication process are discussed in chapter VI. A comparison of micro-switch pull-in voltage, collapse voltage, contact force, and contact resistance, discussed next, was accomplished using SNM01 DC-only micro-switch test structures with sputtered Au electric contacts. The results of this study validated using analytic equations to design micro-switches for the second generation mask set (i.e., SNM02 designs) which is discussed in section 5.3.

5.2 SNM01 Micro-Switch Analysis

In this section, DC-only micro-switches with Au electric contacts were analyzed using analytic equations, FEM design tools, and experimental results. Figure 26 is a captured video image of a representative micro-switch fabricated using the modified SNM01 fabrication process similar to that outlined in Table 8.

Analytic equations and FEM modeling and simulation design tools are useful for evaluating MEMS switch designs prior to device fabrication [130, 139]. In this study, pull-in voltage, collapse voltage, and contact force of cantilever-style,
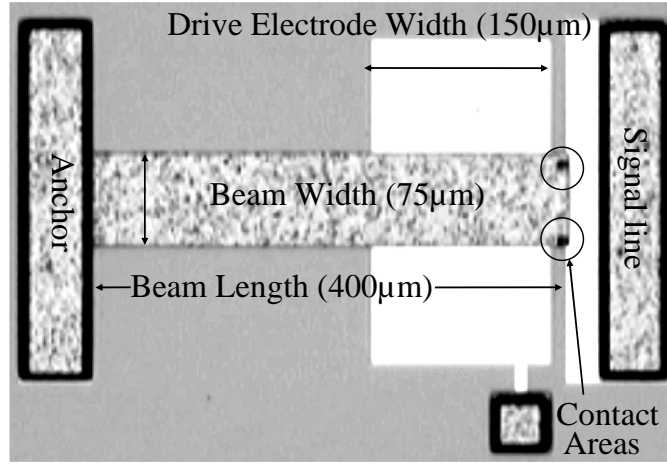
Figure 26   A captured video image of an SNM01 micro-switch with a 150 μm wide drive electrode.

electrostatically actuated, micro-switches were modeled and simulated, using simple equations and the Coventorware [35] finite element software package. Contact resistance was modeled using Holm's well known plastic material deformation model [59]. Simulated pull-in voltage, collapse voltage, and contact resistance were compared to experimental results. Contact force measurements were not collected directly but a useful contact force range, bounded by pull-in and collapse voltages, was predicted. Useful contact force range, contact resistance, and mechanical contact cleaning were further investigated by varying the dimensions of the micro-switch's drive or actuation electrode.

   5.2.1   FEM Design Tool: Coventorware.   The SNM01 cantilever-style micro-switch layout is shown in Figure 27. The beam is 75 μm wide and 400 μm long and the drive electrode width was varied from 50 - 350 μm. The apparent contact area is defined by two upper contact dimple areas. Each dimple was approximately 8 μm in diameter and the contact metallurgy was gold-on-gold.

   The micro-switch design was drawn using a 2D layout editor [151], converted to GDS format, and imported into Coventorware [35]. Next, the device foundry process

73
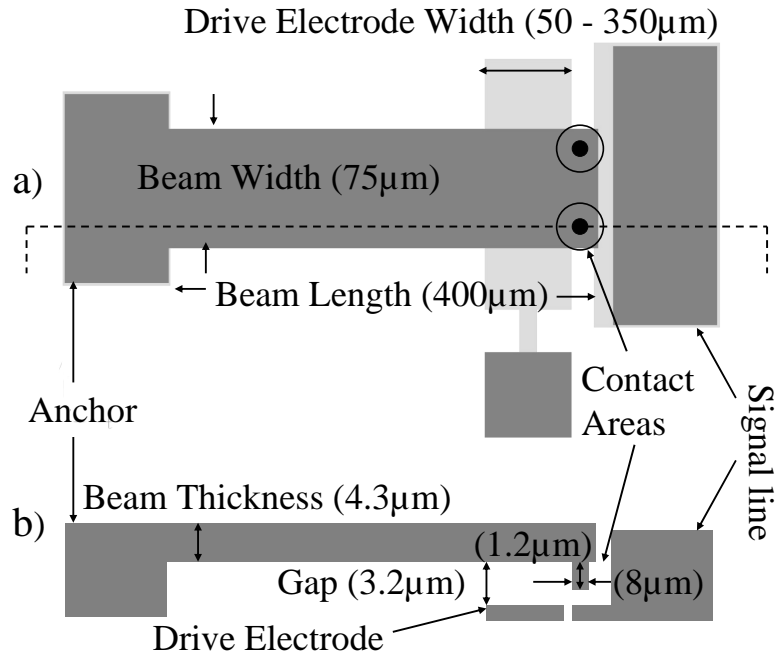
Figure 27   Micro-switch layout (a) top view (b) side view.

(Table 8) required by Coventorware to construct the solid model, was defined. The format of Table 8 is similar to Coventorware's graphical user interface.

Table 8   Summary of the foundry process defined in Coventorware.

Step	Action	Material	Layer/Mask	Type	Thickness/Depth (μm)
0	Base	GaAs	Substrate		20.0
1	Deposit	Evaporated Au	Contact	Stacked	0.3
2	Deposit	Air Dielectric	Dielectric	Stacked	0.001
3	Etch		Electrode		0.301
4	Deposit	Photoresist	Sacrificial	Conformal	3.2
5	Etch		Anchor		3.2
6	Etch		Dimple		1.2
7	Deposit	Plated Au	Structural	Conformal	4.3

The elastic modulus and Poisson's ratio, needed for the simulations, for the Au structural layers were 80 GPa and 0.42, respectively. Residual stresses due to

the fabrication process were assumed to be zero and the released cantilevers were modeled as perfectly flat beams.

The solid model, generated by combining the 2D layout, the material properties, and the foundry process, was meshed using Coventorware's "Free (Tetrahedra)" and "Manhattan (Brick)" elements. Tetrahedra elements were used to mesh the conformal geometry of the structural layer while brick elements were used to mesh the planarized geometry of the drive electrode. These meshes, created separately, were combined into a single mesh prior to running each simulation. This procedure provided the best overall nodal coverage and ensured reliable, repeatable results.

Additionally, linear or parabolic elements can be used with each of these meshing options. Linear elements consist of 4 node tetrahedrons while parabolic elements consist of 10 node tetrahedrons [35]. Because they have fewer nodes, linear elements are "stiffer" than parabolic elements and are suited device parts that do not bend or flex. Parabolic elements, however more accurately represent bending structures because of their increased number of nodes. A careful mesh analysis was accomplished to ensure accurate and timely simulation results.

The mesh analysis used here consisted of establishing realistic boundary conditions, creating a mesh, and then running a Coventorware "pull-in" simulation. The simulation was iterative and required both voltage and deflection tolerances to achieve solution convergence. The voltage and deflection tolerance values used here were 0.5 volts and $10^{-3}\mu m$, respectively. When the software tool calculated a result within the specified tolerance band the simulation ended. "Default" Coventorware meshes with linear elements (i.e., minimum number of nodes) were used initially for both the structural and drive electrode layers. After each mesh analysis simulation, the relative mesh quality (i.e., the number of nodes in the structural layer) was compared to the resulting beam collapse voltage to determine if increased structural layer mesh quality was needed. Parabolic elements were used on the device's structural layer while "default" linear element meshes were used for all the

drive electrode geometries. Higher quality drive electrode meshes were not needed because they are stationary, non-moving parts of the device.

A thin dielectric layer, not present in the actual device, was defined on top of the drive electrode to avoid crashing the simulation upon reaching the beam's collapse voltage. The dielectric layer was meshed the same way as the drive electrode. Figure 28 shows that structural layer meshes greater than about 650 nodes did not change the collapse voltage by more than one volt. Structural layer meshes created with 664 nodes and "default" drive electrode and dielectric meshes were used for all simulations runs. This iterative procedure of comparing simulation results with mesh quality ensured adequate mesh size while minimizing simulation run times.

Collapse Voltage vs Number of Nodes
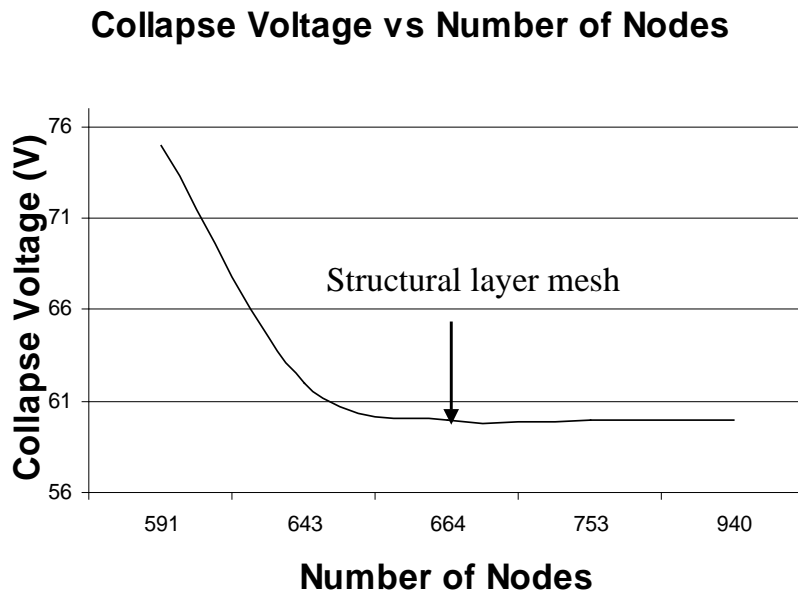
Figure 28   Mesh analysis results using a micro-switch with a 200 μm wide drive electrode.

The FEM simulations were accomplished using Coventorware's mechanical (MEMMech) and combined solution solvers (CoSolveEM). The mechanical solver was used to set the "fixed end patch" with the "fix all" boundary condition to simulate the effects of the actual anchor. The "contact area patches" on the bottom of

76

the switch's upper contacts or dimples were also set using MEMMech [35]. Figure 29 is a close-up of a dimple contact surface, located underneath the cantilever beam, at the bottom of the upper contact.

Beam Side

Free End

Cantilever's underside
(top electrode voltage patch)

Dimple Upper Contact
(contact area patch)
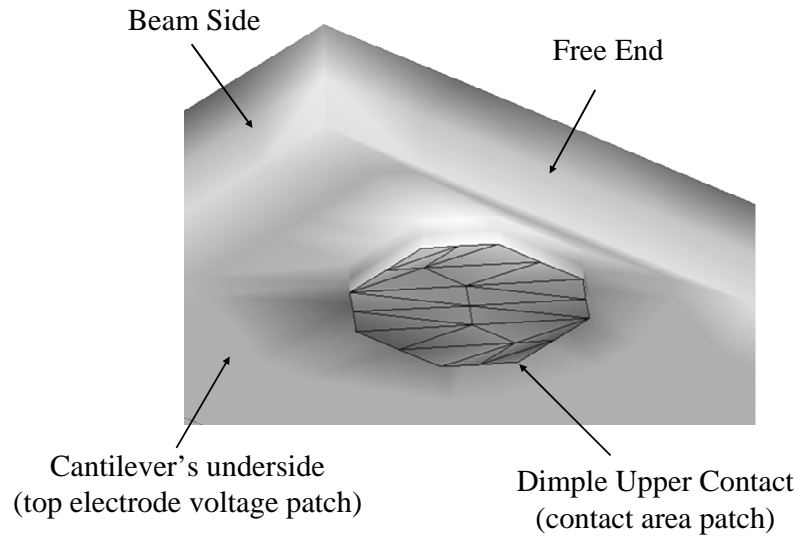
Figure 29   Close-up view of a Coventorware contact surface defined as the bottom patch an upper dimple contact.

The "fix all" boundary condition held all mechanical degrees of freedom (i.e., displacements and rotations) fixed at the beam's anchor end. The combined solver was used to generate electrostatic actuation force by applying a constant voltage between the bottom drive electrode and the cantilever beam.

Properly defined boundary conditions greatly simplify the device's 3D model and also help reduce simulation times by reducing the overall number of elements. For example, in Figure 30 the beam's anchor or fixed end are not present in the 3D model because they have minimal influence over beam deflection.

Once an adequate mesh size was defined a Coventorware "pull-in" simulation with a voltage trajectory ranging from 0 to 75 volts with one volt increments was run. The resulting Coventorware output file contained the beam's pull-in voltage, collapse voltage, and contact force. Contact forces, between the dimple and landing pad surfaces, were calculated by Coventorware after the beam reached the pull-in voltage
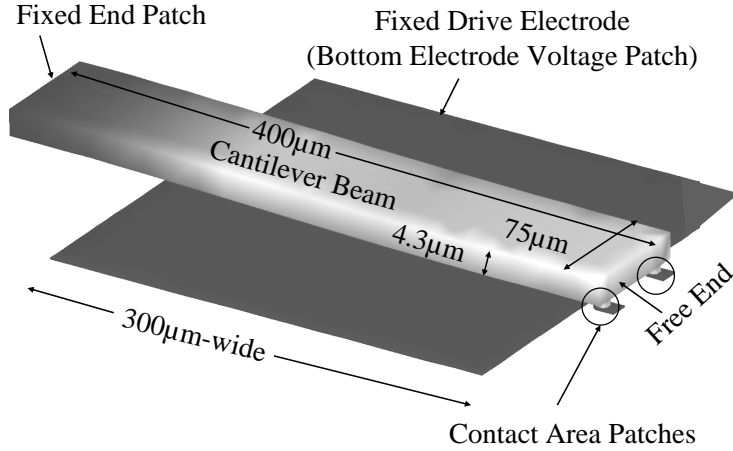
Figure 30   Coventorware simulation results for micro-switch deflection with pull-in voltage applied. The cantilever beam's free end has been deflected approximately 2 μm, illustrated by the lighter color, and the dimples are in physical contact with the lower landing pads. The device has a 300 μm-wide drive electrode.

and up to the beam's collapse voltage. As the collapse voltage was approached significant stress was induced near the anchor and contact ends of the beam as shown in Figure 31.

Also shown in Figure 31 is the leading edge (near the beam's tip) of the electric contacts tending to lift off the planar lower contacts as the beam bends and the collapse voltage is approached. This observation highlights some important design considerations, discussed by Mercado et al., about the placement of micro-switch electric contacts. For example, electric contacts not placed near the beam's tip and located on the side of the cantilever exhibit increased contact and restoring forces due to mechanical advantage [101].

5.2.2 *Analytic Equations.*   For comparison, the cantilever-style micro-switches were modeled analytically. The pull-in voltage (V_{pi} and V_{piFF}), contact force (F_C), collapse voltage (V_{cpi}), and contact resistance (R_{cDP}) were found using Equations 17, 18, 22, 23, and 54, respectively. The hardness, elastic modulus, and bulk
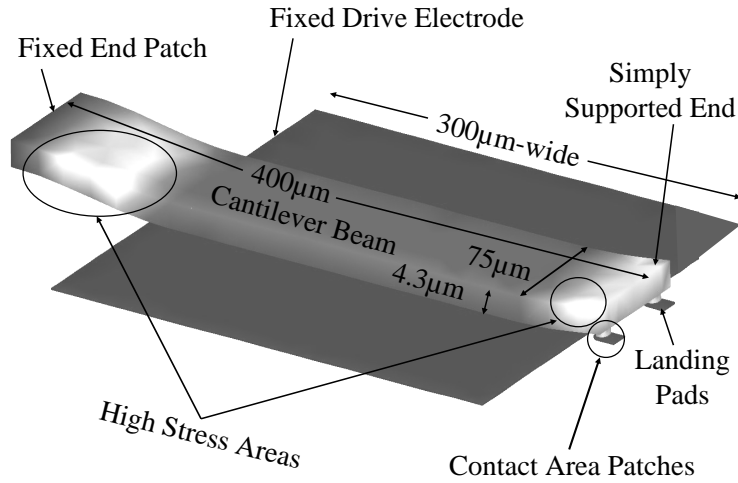
Figure 31 Coventorware simulation results for micro-switch stress with collapse voltage applied. The cantilever beam has been overdriven with an applied electrostatic force until it collapsed onto the drive electrode. The light areas near the anchor and the electric contact ends qualitatively illustrate the location of high stress areas due to actuation and beam bending. The device has a 300 μm wide drive electrode.

resistivity values used for the calculations were 2 GPa, 80 GPa, and 2.2 $\mu\Omega - cm$, respectively [59]. The beam dimensions are listed in Table 8.

   5.2.3 Experiment.   A series of 75 μm wide by 400 μm long micro-switches, like that shown in Figure 26, were tested to characterize pull-in voltage, collapse voltage, and closed switch resistance. The devices were fabricated with drive electrode widths varying from 50 - 350 μm. During operation a bias voltage was applied between the cantilever beam and the drive electrode. The metal contact micro-switch closes when the magnitude of the bias voltage exceeds the pull-in voltage, V_{pi}. As the applied bias is increased beyond the pull-in voltage, the contact force increases and a second threshold is reached when the cantilever beam collapses onto the drive electrode at V_{cpi}. The maximum contact force is determined by the maximum voltage that can be applied before the beam collapses at the second threshold. Once the second threshold is reached, the switch shorts out and is no longer operable. The

79

voltage range between when the switch initially pulls in and when the beam collapses onto the drive electrode is the useful operating range of the switch:

$$V_{\mathrm{pi}} \leq V < V_{\mathrm{cpi}}. \tag{71}$$

The switch operating range is characterized experimentally by measuring the resulting closed switch resistance as the applied drive voltage is increased above the pull-in voltage.

The switches in this study were experimentally tested at AFRL/SNH by wafer probing using a Cascade Summit 9000 Microprobe Station with standard microprobes. The bias or actuation voltage was applied using an HP 3245A universal source. Beam resistance measurements were accomplished using an HP 34401A multimeter in a four-point probe configuration. All of the instruments were controlled with a PC using an IEEE-488 bus. During testing, the applied bias from the source was swept from 5 to 75 volts in 1 volt increments. Beam deflections were measured using a Burleigh Horizon interferometric microscope (BHIFM). Figure 32 is a schematic of the experimental setup used to measure closed switch resistance. Results are discussed next.

5.2.3.1 Results Comparison. The data shown in Figure 33 was obtained from a micro-switch like the one shown in Figure 26. The plot shows the measured resistance as a function of the applied actuation voltage. The two operational voltages, shown on Figure 33, are when the beam pulls in (V_{pi}) and when the beam collapses (V_{cpi}). At pull-in, the resistance drops when electrical contact is first initiated, while at collapse the measured resistance increases sharply indicating that the beam has collapsed onto the bottom electrode. Once pull-in is achieved, the resistance gradually decreases from approximately 3.0 Ω to approximately 0.3 Ω. The initial decrease in closed switch resistance is due to contaminant film fritting (i.e., the mechanical rupture or electrical break down when enough voltage is applied [59])

80
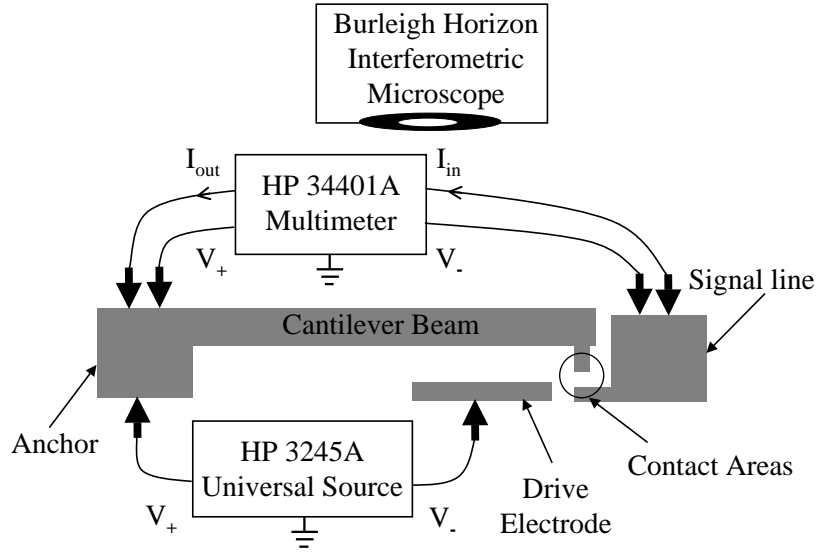
Figure 32   Schematic illustration of the circuit used to actuate the micro-switches and measure the closed switch resistance.

and quasi-metallic contact as the contact force is increased [59]. As metal-to-metal ohmic contact areas increases with increased contact pressure the contact material plastically deforms resulting in increased contact area and decreased contact resistance [59]. Maximum contact force (minimum resistance) occurs just prior to the beam collapsing onto the bottom electrode. Once collapse occurs, the voltage drops to approximately zero and the resistance rapidly increases because of current flowing from the drive electrode through the micro-switch. This additional current corrupts the beam's four-point probe resistance measurement depicted in Figure 32.

To confirm that the measured voltage going to zero is due to beam collapse and not a surface breakdown current, an optical profile was taken of two switches. The first was measured prior to any testing. The second was measured after it had been tested through collapse. The measured profiles of the two cantilevers are shown in Figure 34.

The profiles, captured using the BHIFM, show that the unactuated beam has a slight downward curl. This curvature follows the profile of the sacrificial layer that

81
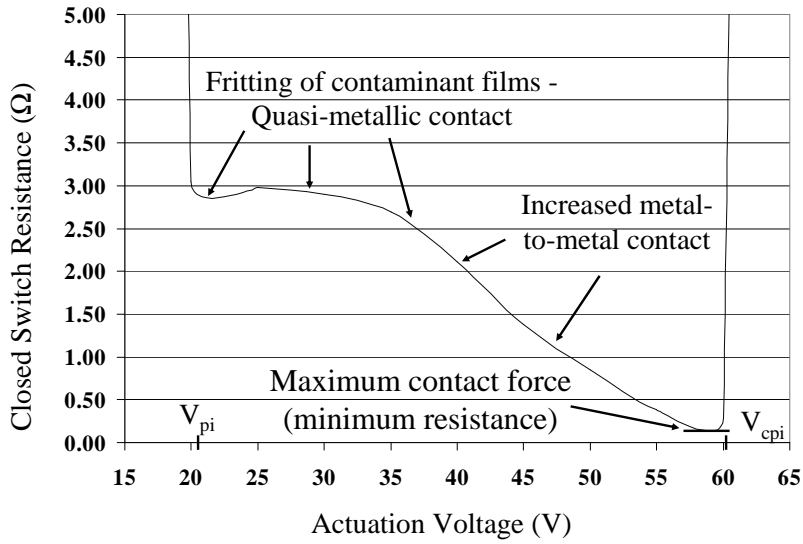
Figure 33   Representative plot of measured switch resistance versus applied actuation voltage for a switch with a drive electrode 150 μm wide. The initial drop in the measured resistance occurs at the pull-in voltage and and sharp increase in resistance occurs at the collapse voltage.
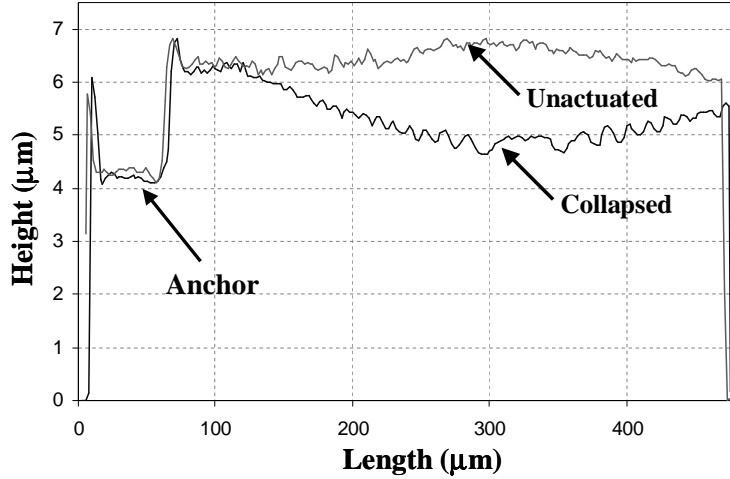
Figure 34   Measured beam deflections obtained using an interferometric microscope illustrating the curvature of an unactuated and collapsed cantilever beam.

conforms to the underlying electrode layer. The beam that has been collapsed shows an upward curvature with the lowest point over the drive electrode. This profile is consistent with the beam having collapsed onto the bottom electrode.

Table 9 is a summary of the FEM-based pull-in voltage, collapse voltage, and maximum contact force simulation results produced using Coventorware. The simulated pull-in and collapse voltages decrease as the drive electrode width increases. Also, the maximum contact force, defined as the force one solution step (i.e., one volt) prior to beam collapse, has a parabolic relationship with the drive electrode width. A maximum contact force of 35.5 μN, found using Coventorware, occurs with a drive electrode 150 μm-wide. The corresponding useful contact force range is between 21 V and 66 V.

Table 9   Coventorware simulation results for pull-in voltage, collapse voltage, and maximum contact force (F_C) for devices with drive electrodes ranging from 50 - 350 μm wide.

Width (μm)	Pull-in (V)	Collapse (V)	Max. F_C (μN)
50	32	>75	11.0
100	24	>75	27.5
150	21	66	35.5
200	21	59	29.9
250	21	56	29.8
300	20	54	25.4
350	20	53	25.1

Table 10 is a summary of the analytical-based pull-in voltage, collapse voltage, maximum contact force, and minimum resistance simulation results. Again, the simulated pull-in and collapse voltages decrease as the drive electrode width increases. Also, the maximum contact force, defined as the force one volt prior to beam collapse, has a parabolic relationship with the drive electrode width. A maximum contact force of 45.4 μN, found using Equation 22, also occurs with a drive electrode 150 μm wide. The corresponding useful contact force range is between 20.3 V and 64.6 V. The minimum contact resistance, found using Equation 54, was 0.14 Ω. For all the contact resistance calculations, contaminant film resistance (i.e., R_{cf}) was assumed equal to 0 Ω.

Table 10   Analytically calculated pull-in voltage, collapse voltage, maximum contact force (F_C), and minimum resistance (R_c) for devices with drive electrodes ranging from 50 - 350μm wide.

Width (μm)	Pull-in (V_{pi})	Collapse (V_{cpi})	Max. F_C (μN)	Min. R_{cDP} (Ω)
50	31.4	>75	13.2	0.25
100	23.4	>75	27.3	0.17
150	20.3	64.6	45.4	0.14
200	18.8	46.9	27.9	0.17
250	18.1	37.7	18.8	0.21
300	18.0	32.8	14.2	0.24
350	18.3	30.3	11.7	0.26

Using Equations 17 (V_{pi}) and 18 (V_{piFF}), pull-in voltage predictions were compared to measured values. The measurements (from Table 11) were obtained using SNM01 DC-only devices similar to that shown in Figure 26. The pull-in data from this style micro-switch was used (versus data collected using an SNM02 micro-switch like the one shown in Figure 35) because the oversized bottom electrodes provided a worse case scenario for the first-order parallel plate capacitor model derived in chapter III, section 3.5. Table 11 is a comparison of pull-in voltage predictions, based on a simple parallel plate capacitor model and a model that accounts for fringing fields, and measurements.

Table 11   A summary of pull-in voltage predictions, based on a simple electrostatic force model (V_{pi}) and a model that accounts for fringing fields (V_{piFF}), measurements, and the percent difference for SNM01 micro-switches with drive electrodes ranging from 50 - 350 μm wide.

Width (μm)	Measured	(V_{pi})	% diff.	(V_{piFF})	% diff.
50	25.9	31.4	19.2	32.0	21.1
100	24.3	23.4	3.8	23.8	2.1
150	22.7	20.3	11.2	20.7	9.2
200	22.8	18.8	19.2	19.1	17.7
250	22.8	18.1	23.0	18.4	21.4
300	22.6	18.0	22.7	18.3	21.0
350	21.3	18.3	15.2	18.6	13.5

The percent difference data, presented in Table 11, shows an $1-2\%$ improvement (the difference between columns 4 and 6) in predicted pull-in voltage, when fringing fields are considered using Osterberg and Senturia's model, for SNM01 micro-switches with bottom electrodes ranging from 100 - 350 μm-wide. The pull-in voltage prediction for devices with 50 μm wide drive electrodes, however, was approximately 2% worse. Based on these small differences in predicted pull-in voltage, the simpler first-order parallel plate capacitor model was used for all analytic derivations.

Table 12 is a summary of pull-in voltage, collapse voltage, and minimum contact resistance measurements. Contact resistance was found by subtracting the measured beam bulk resistance (0.03 Ω) from the resistance value found using the experimental setup shown in Figure 32. The measured pull-in and collapse voltages decrease as the drive electrode width increases. Minimum contact resistance values were measured for devices with 100 μm wide and 150 μm wide drive electrodes. The useful contact force range was between 24.3 V and 61.0 V for devices with 100 μm wide drive electrodes and between 22.7 V and 58.3 V for devices with 150 μm wide drive electrodes.

Table 12   Experimental pull-in voltage, collapse voltage, and resistance measurements for devices with drive electrodes ranging from 50 - 350 μm wide.

Width (μm)	Pull-in / StdDev (V_{pi})	Collapse / StdDev (V_{cpi})	Min. R_{C} / StdDev (Ω)
50	25.9 / 2.3	61.8 / 4.0	0.35 / 0.06
100	24.3 / 2.7	61.0 / 1.8	0.25 / 0.02
150	22.7 / 0.9	59.7 / 0.1	0.26 / 0.07
200	22.8 / 1.2	59.5 / 0.6	0.30 / 0.08
250	22.8 / 1.4	59.3 / 1.0	0.39 / 0.23
300	22.6 / 0.4	57.9 / 0.9	0.45 / 0.14
350	21.3 / 0.7	58.8 / 1.6	0.79 / 0.12

The FEM and analytically derived relationship between drive electrode width and pull-in voltage, shown in Tables 9 and 10, agree with the experimental pull-in voltage measurements found in Table 12. The collapse voltages found using Coven-

torware (Table 9) agree with the collapse voltage measurements (Table 12). As the drive electrode width increases, however, the collapse voltage calculated using analytic equations, agree less and less with Coventorware or the measurements. This is due to the changing beam shape as the electrostatic force increases and the deformed beam becoming less accurately represented by Figure 12.

The FEM and analytic contact force calculations have the same trend and both predict that maximum contact force is generated by overdriving switches with 150 μm wide drive electrodes. Contact force measurements were not available. The resistance measurements have a similar trend as the the analytically calculated resistance with the minimum resistance measurements corresponding to devices with 100 μm wide drive electrodes. Although the resistance measurements for switches with a 100 μm wide drive electrodes were slightly lower than for devices with 150 μm wide drive electrodes the corresponding collapse voltages were higher. This indicates that more applied voltage was needed with 100 μm wide drive electrode devices than in the 150 μm wide drive electrode devices to generate the same contact force (and resulting resistance).

Electrostatically actuated, metal contact, micro-switches depend on having adequate contact force to achieve desired, low contact resistance [59, 62, 94]. Using simple analytic equations and Coventorware, micro-switches were simulated and approximate pull-in voltage, collapse voltage, and maximum contact force were predicted. Higher simulated contact force resulted from overdriving the cantilever beams after initial switch closure or pull-in. Experimentally, overdriving the cantilever beams, beyond the pull-in voltage, resulted in higher contact force and correspondingly lower switch resistance measurements. The difference between the pull-in voltage and beam collapse voltage was defined as the useful contact force range.

The simulation results show that MEMS switches, with this geometry, and a 150μm wide actuation electrode, can achieve the highest contact force when overdriven and operated within the useful contact force range. Pull-in voltage, collapse

voltage, and contact resistance measurements agree with simulated results obtained from analytic equations and Coventorware. Based on this analysis, SNM02 micro-switch test structures with hemispherical-shaped upper and planar lower electric contacts were designed utilizing analytic equations.

5.3 SNM02 Test Structures

Electrostatically actuated, cantilever-style, DC and RF-testable micro-switch test structures, shown in Figure 35, were designed using Equations 17 (pull-in voltage), 22 (contact force), 3 (restoring force), 23 (collapse voltage), and 54 (contact resistance). The devices were designed as part of a CPW pad frame for RF-testability and therefore were limited in length and width (250 μm long by 80 μm wide) to preserve a 50 Ω RF characteristic impedance. Based on this design constraint and electric contact cleaning considerations (i.e., friction between the electric contacts caused by beam bending), contact force was calculated for structures with bottom electrodes ranging from 50 - 200 μm wide (in 50 μm increments). Micro-switches with 100 μm wide bottom electrodes were found to maximize contact force.
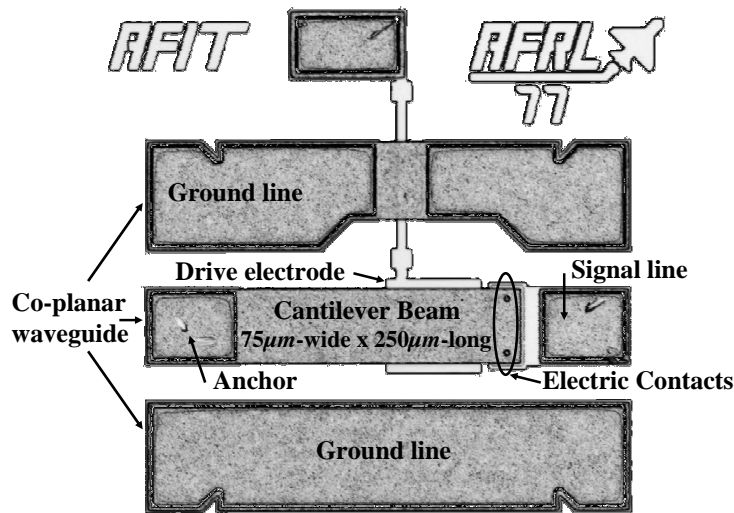
Figure 35   A captured video image of a cantilever-style, RF MEMS metal contact switch with contacts at the beam's end (D77 design).

Table 13 summarizes the pull-in voltage, maximum contact force, minimum restoring force, beam collapse voltage, and minimum contact resistance predictions using analytic equations for micro-switches with 100 μm wide drive electrodes like that shown in Figure 35.

Table 13   Pull-in voltage, contact force, beam collapse voltage, and contact resistance design predictions for SNM02 cantilever-style test structures shown in Figure 35.

Pull-in voltage	47.2 V
Contact force per contact	28.7 μN
Restoring force per contact	17.5 μN
Collapse voltage	95.7 V
Contact resistance for two contacts	0.074 Ω

In addition, a cantilever-style, micro-switch, shown in Figure 36, with a topography similar to Northeastern University's micro-switch [95, 173] was designed in collaboration with the AFRL [166] and was also used to evaluate alloy electric contact materials studied in this dissertation. The device had two electric contacts (≈ 8 μm in diameter) symmetrically placed at each side of the cantilever beam (vice being located at the end of the beam) and 20 μm back from the beam's tip. The electrostatic and contact forces were co-located near the beam's end which increased the beam's collapse voltage to greater than 120 V. Mechanical cleaning, however, was not effective with the side contact design due to the placement of the electrostatic and contact forces in the vicinity of the contact bumps (i.e., the co-located forces minimized beam bending and mechanical contact wiping).

5.4   Summary

A design analysis of an SNM01 micro-switch was presented in this chapter. The AFRL/SND baseline micro-switch fabrication process and two other processes (i.e., the modified SNM01 process and the SNM02 process) for fabricating SNM01
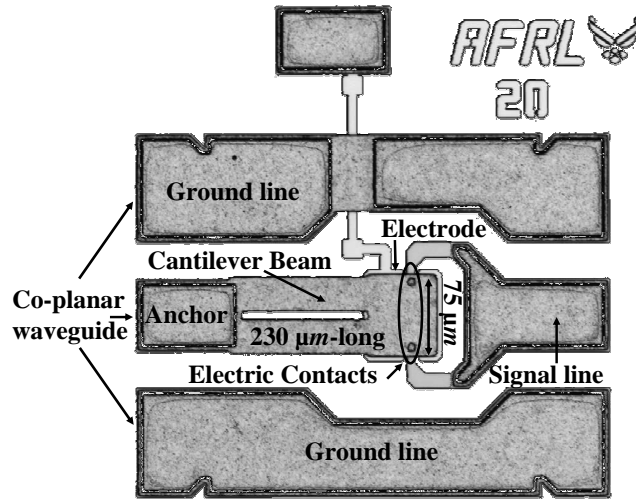
Figure 36   A captured video image of a cantilever-style, RF MEMS metal contact switch with symmetric side contacts (D20 design).

and SNM02 designs with alloy contact materials and hemispherically-shaped upper contact geometries are discussed in the chapter VI.

VI. Device Fabrication

The following chapter outlines three fabrication process needed to accomplish this research. The novel contributions to the MEMS field, discussed in this chapter, are an improved hemispherically-shaped upper electric contact geometry and operational RF MEMS metal contact switches with sputtered bi-metallic (i.e., Au-on-Au-(6.3at%)Pt), binary alloy (i.e., Au-(3.7at%)Pd and Au-(6.3at%)Pt), and ternary alloy (i.e., Au-(5at%)Pt-(0.5at%)Cu) contact metals.

6.1 Background

The three fabrication processes needed to complete this research follow: 1) the AFRL/SND baseline process developed for the SNM01 mask set, 2) the modified SNM01 process, and 3) the SNM02 process. The AFRL/SND baseline fabrication process, discussed in section 6.2 resulted in a protruding ridge around the perimeter of the upper electric contact and did not allow for using novel contact metals. The modified SNM01 fabrication process, discussed in section 6.3, was developed (based on the AFRL/SND baseline fabrication process) to incorporate a hemispherically-shaped upper contact geometry and to allow for novel contact materials. Next, an SNM02 process, discussed in section 6.4, was developed (based on the modified SNM01 process) to utilize the additional SNM02 mask mask layers for inserting novel contact metals only on the contact areas.

6.2 Baseline Process

Figure 37 is a SEM image of an example RF MEMS metal contact switch, with gold electric contacts, that was fabricated on a gallium arsenide wafer using the AFRL/SND baseline process and the SNM01 mask set.

The cantilever beam, shown in Figure 37, appears relatively flat and not curled up or deformed due to residual stress resulting from device fabrication [5, 47, 148].
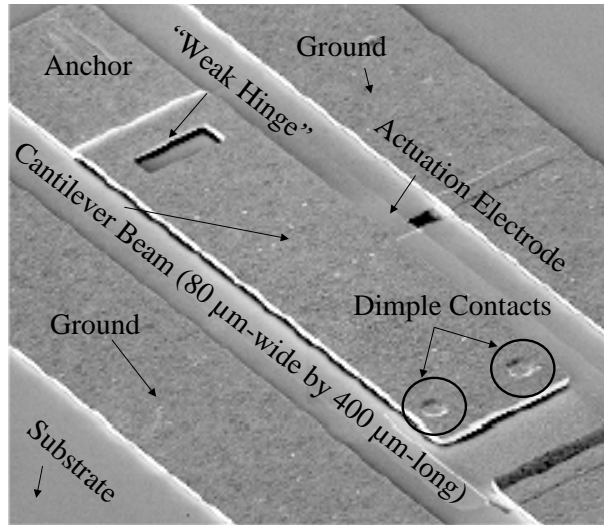
Figure 37   SEM image of an RF MEMS metal contact switch with gold electric contacts fabricated using AFRL/SND's baseline process and the SNM01 mask set.

This process feature was made possible because relatively thin (≈ 700 Å) sputtered Au seed layers were used in conjunction with relatively thick (≈ 5 μm) low-stress, electroplated Au mechanical structural layers.

Refer to Figure 38 for the following discussion.

The actuation electrode and lower electric contact layers were approximately 3000 Å of evaporated Au patterned using a standard metal lift-off technique (**a**) [91]. A thin (200 Å-thick) chromium (Cr) or Ti layer was used under the evaporated Au layer to help the Au remain adhered to the sapphire substrate. The beam's gap or sacrificial layer was approximately 3 μm-thick and created using MicroChem's poly-dimethylglutarimide (PMGI) based photoresist (**b**) [102]. The micro-switch's hinge geometry was defined in the sacrificial photoresist using standard photolithography techniques (**c**) [64]. A timed re-flow in an air oven (without flowing nitrogen) was used to reform the hinge geometry (**d**). The upper contact geometry, shown in Figure 37, was defined by a partial expose, while rotating the wafer, and develop of the sacrificial photoresist layer (**e**).
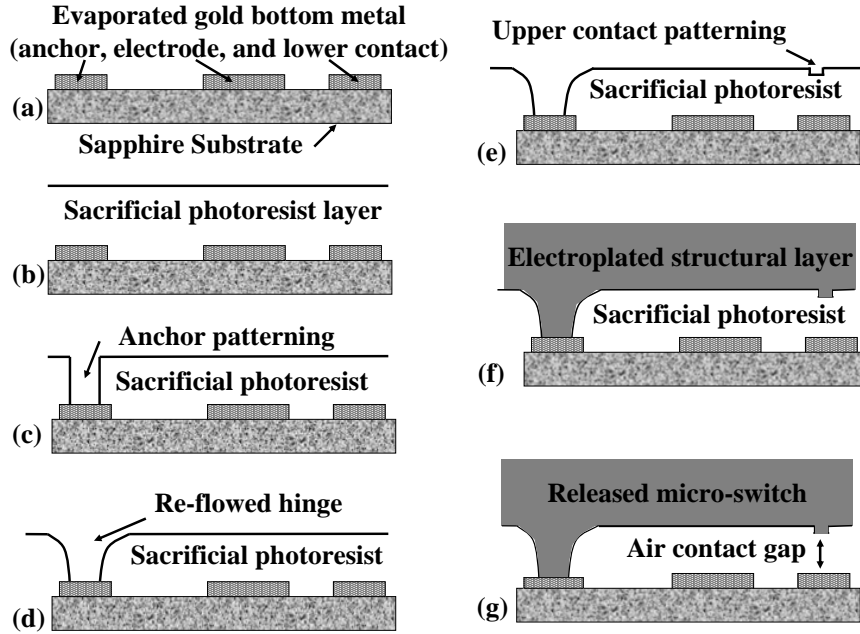
Figure 38   Illustration of AFRL/SND's baseline fabrication process (DC-only devices).

After electroplating the cantilever's gold structural layer (≈ 5 μm-thick) (**f**), the devices were released using a CO_2 critical point dryer (**g**).

Table 14 summarizes the layer thicknesses resulting from the AFRL/SND baseline fabrication process.

Table 14   Summary of layer thicknesses for the AFRL/SND baseline fabrication process.

Layer	Material	Thickness
Structural (beam)	Plated Gold	$5.0\mu m$
Sacrificial (gap)	Polymethylglutarimide (PMGI)	$3.0\mu m$
Electrode & Lower Contact	Evaporated Au	$0.3\mu m$
Dimple/Upper Contact	Electroplated Au	$1.0\mu m$

Although the SND process was repeatable a number of issues needed resolution before MEMS switches with metal alloy electric contacts could be successfully fabricated. For example, the upper contacts for micro-switches fabricated using the SNM01 baseline process exhibited a protruding ridge, shown in Figure 39, around
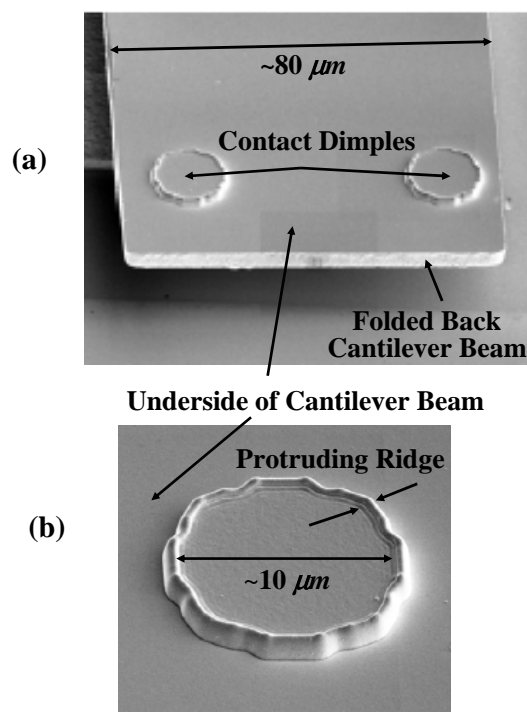
Figure 39   Scanning electron micrographs: (a) Folded back AFRL/SND metal contact micro-switch (b) Magnified view of an upper contact bump. Notice the protruding ridge along the perimeter of the contact area.

the outer perimeter of the dimple contact. The process modifications needed to fabricate SNM01 devices with metal alloy electric contacts and hemispherical-shaped upper contacts are presented next.

6.3   Modifications for SNM01 Processing

The SNM01 baseline fabrication process was modified to enable fabrication of micro-switches with sputtered metal alloy electric contacts. First, the processing step of sputtering the lower contact alloy was added. Since the SNM01 mask set does not allow selective placement of electric contact metals, the lower contact alloy was deposited on top of all the evaporated Au base layers (i.e., the anchor and bottom electrode). The layer thicknesses for the Cr adhesion, the evaporated Au, and the metal alloy contacts were adjusted to maintain the original SNM01 layer thicknesses

summarized in Table 14. Also, a Ti lower contact adhesion layer was not used to avoid problems, discussed in section 4.1, associated with using Au-Ti alloys electric contact metals.

Due to the conformal nature of the sputtered contact materials, "wings" or raised metal "edges," shown in Figure 40, remained after performing metal lift-off. Ultrasonic treatments and high pressure (40 psi) acetone sprays were helpful but did not eliminate this problem.
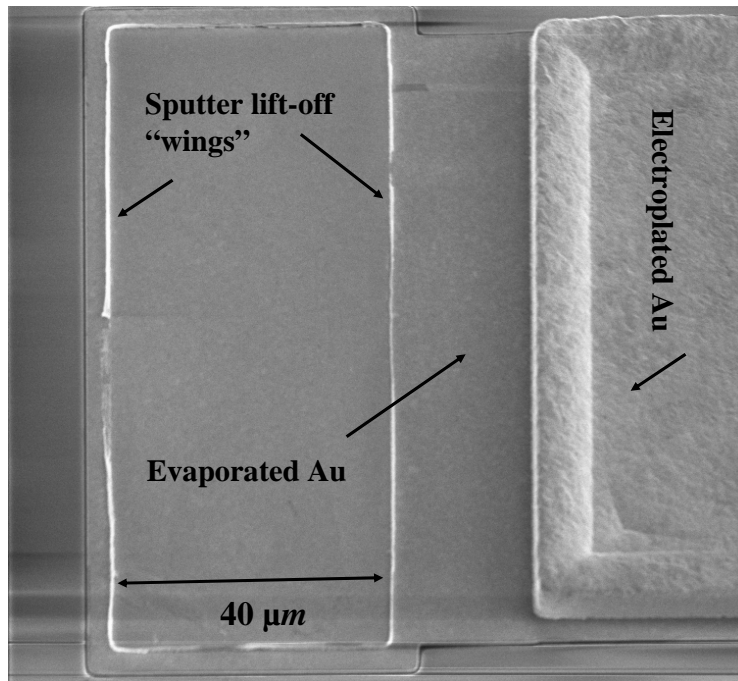
Figure 40   SEM image of "wings" resulting from sputtered metal lift-off.   The cantilever beam was removed to clearly view the bottom contacts.

Next, the wafer rotation step, used during baseline dimple area processing, was eliminated and the timed reflow, originally used to reform only the hinge geometry, was accomplished after the partial exposure and develop of the upper contact areas. By removing the wafer rotation step, only the bottom of the upper contact "well" was exposed (i.e., Deep UV travels in nearly straight lines in photoresist) and not the outer walls of the upper contact "wells" which helps minimize the protruding ridge problem associated with the baseline process. Also, the length of the timed reflow for

both the hinge and upper contact geometries was investigated. For example, SNM01 SEM images showed an approximate 3 μm shift in the hinge geometry at the corner of the beam and anchor well. For a 10 μm upper contact diameter, the hypothesized geometry, assuming that all corners shift by the same amount (i.e., 3 μm), was a nearly symmetric hemispherical shape with a 3 μm radius. For contact geometries less than 10 μm in diameter, the upper contact depth was hypothesized to "shrink-up," resulting in smaller upper contact bumps. Figure 41 is an SNM01 upper contact test structure with an array of dimple diameters. From the figure observe that all the reflowed dimples are hemispherically-shaped and that small diameter upper contacts result in shorter dimples.
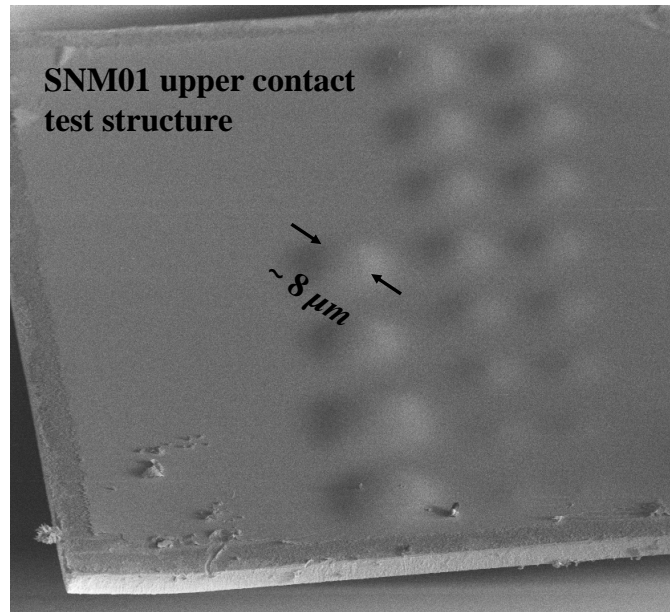
Figure 41   SEM of an SNM01 upper contact test structure showing an array of dimple diameters.

In addition, an oven with flowing nitrogen was used to help minimize contamination from other processes. The resulting reflow times were approximately double the times needed for the baseline process which used an air oven without flowing nitrogen.

Once again, since the SNM01 mask set did not allow for the selective placement of contact metals, the upper contact materials were deposited prior to the seed layer needed for the electroplated Au structural layer. The contact alloy was deposited first, followed by the Au seed layer and a thin Ti layer needed to define the electroplating mold. The layer thickness were chosen to be similar to the baseline process to avoid fabrication induced stress (and device curling) caused by using thicker sputtered layers.

The electroplating system, used to deposit the micro-switch structural layer, was a semi-automated electroplating bath with continuous solution filtering. Four electrical connections, one in each quadrant of the wafer, was used to bias the wafer. The resulting electroplated Au films were non-uniform across the wafer. The approximately shape of the the electroplated Au thickness, across a target wafer, was paraboloid with the vertex located at the wafer's center. The edges of the wafer were approximately 1-1.25 μm thicker than the center of the wafer. The effects of this non-uniformity are discussed further in chapter VII.

The modified process flow, for the DC-only devices, is summarized in Figure 42. The RF-testable devices, like that shown in Figure 37, were not designed with an evaporated Au adhesion layer under the electroplated Au CPW or the cantilever beam's anchor and resulted in device delamination from the sapphire wafers. Refer to Figure 42 for the following discussion.

The actuation electrode and lower electric contact layers were approximately 3000 Å of evaporated Au patterned using a standard metal lift-off technique (**a**) [91]. A thin (200 Å thick) chromium (Cr) layer was used under the evaporated Au layer to help the Au remain adhered to the substrate. The lower electric contact metal was sputter deposited (500 Å thick) and patterned using a metal lift-off technique (**b**).

The beam's gap or sacrificial layer was approximately 3 μm thick and created using MicroChem's polydimethylglutarimide (PMGI) based photoresist (**c**) [102].
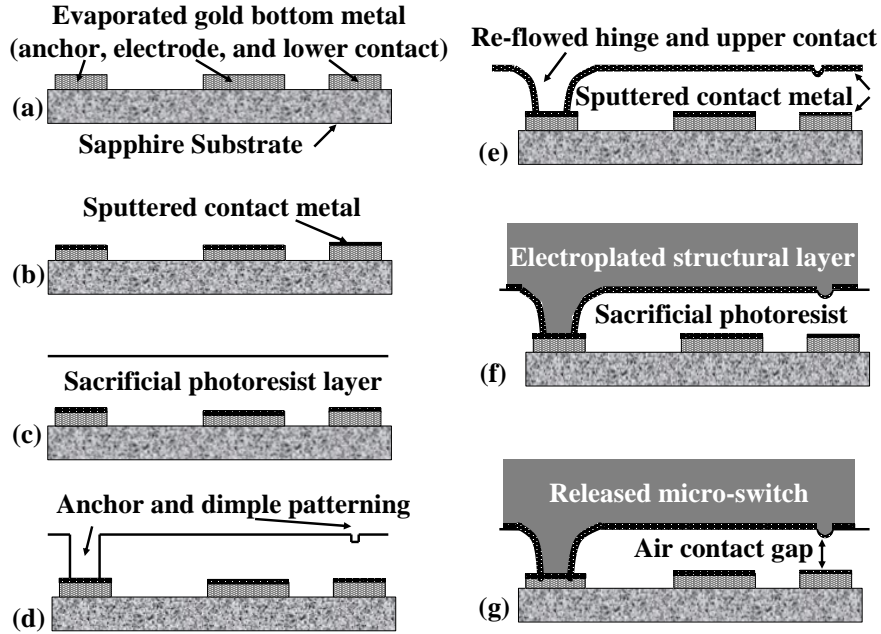
Figure 42   Illustration of the modified SNM01 fabrication process.

The micro-switch's hinge geometry was defined in the sacrificial photoresist using standard photolithography techniques while the upper contact geometries were defined by a partial expose and develop of the sacrificial photoresist layer (**d**). A timed re-flow in an oven with flowing nitrogen was used to reform the hinge and dimple areas into hemisphere-shaped upper contact bumps (**e**). The upper contact metals (500 $\mathring{A}$ thick) were also sputter deposited, and patterned using standard photolithography techniques (**e**) [64]. The upper contact material, located on the underside of the cantilever beam, is highlighted in Figure 43.

After electroplating the cantilever's gold structural layer ($\approx 5~\mu m$ thick) (**f**), the devices were released using a CO_2 critical point dryer and tested to ensure proper operation and performance (**g**).

Figure 44 is a SEM image of an example metal contact micro-switch that was fabricated using modified SNM01 fabrication process.

In addition to fabricating micro-switches with binary alloy (discussed in section 4.1) electric contacts, a single wafer of SNM01 micro-switches with Au-on-Au-

97
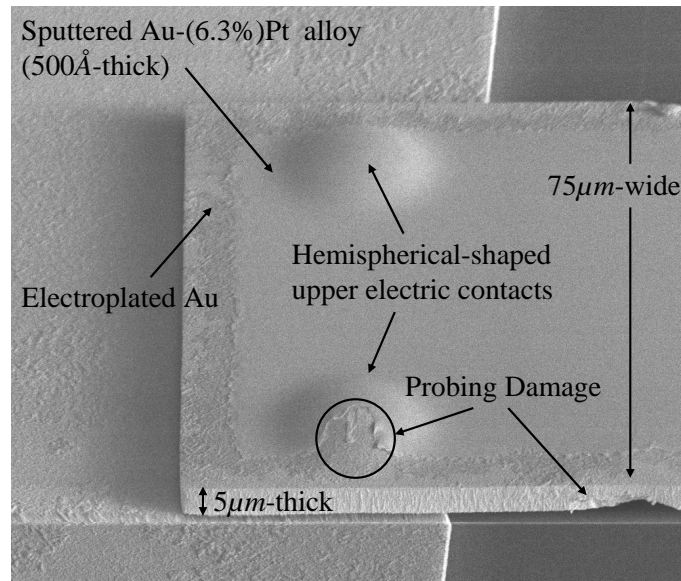
Figure 43   SEM image showing the SNM01 hemisphere-shaped upper contacts and the sputtered electric contact metal. Probing damage occurred while flipping the cantilever beam for imaging.
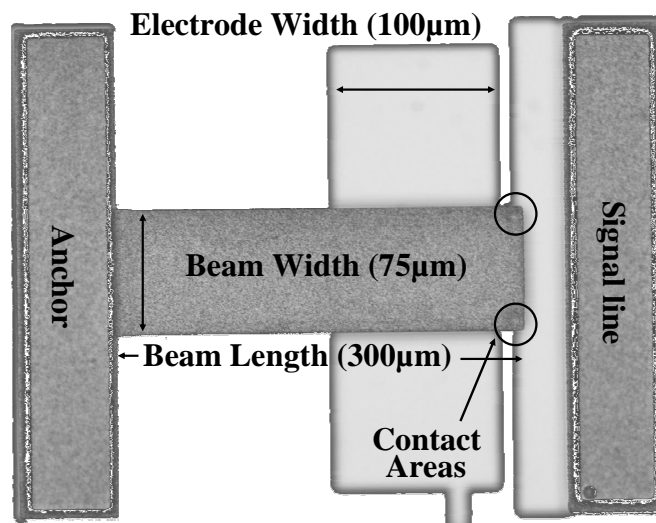
Figure 44   A captured video image of an SNM01 DC-only metal contact micro-switch with gold electric contacts fabricated using the modified SNM01 process.

(6.3at%)Pt (i.e., bi-metallic) electric contacts and a single wafer of SNM01 micro-switches with Au-(5at%)Pt-(0.5at%)Cu (i.e., ternary alloy) electric contacts were also fabricated to briefly investigate the effects of bi-metallic and ternary alloy con-

tact metals. A ternary alloy phase diagram was not available for the Au-Pt-Cu alloy [112]. The wafers successfully fabricated using the modified SNM01 process are summarized in Table 15.

Table 15   Wafers fabricated using the modified SNM01 process.

Wafer ID	Contact Metal/Alloy	Contact Geometry	Gap (μm)
SNM01-17	Au-on-Pd	Flat	3
SNM01-18	Au-(3.7at%)Pd	Flat	3
SNM01-19	Au-(5at%)Pt-(0.5at%)Cu	Hemisphere	3
SNM01-20	Au	Hemisphere	3
SNM01-21	Au-(3.7at%)Pd	Hemisphere	3
SNM01-22	Au-on-Au-(6.3at%)Pt	Hemisphere	3

The modified SNM01 fabrication process followers, developed for this work, are provided in the Appendix A. The process modifications needed to fabricate SNM02 devices with metal alloy electric contacts and hemispherical-shaped upper contacts are presented next.

6.4   Modifications for SNM02 Processing

The SNM02 mask set contained additional photolithography mask layers needed to selectively deposit novel materials onto the electric contacts. The sputtered metal lift-off issue remained but was compensated for with properly designed upper and lower electric contact pairs that kept the "wings" away from the actual contacting areas. The effect of having "wings" is addressed in more detail in chapter VII. The hinge and upper contact reflow procedure, developed during SNM01 processing, was also used during SNM02 processing. The upper contact materials were sputter deposited and excess metal (outside of the dimple area) was removed using an etch-back technique. Etchants, normally used to etch away Au seed layers (i.e., Technistrip), were ineffective in removing the Au contact alloys used in this work. Aqua regia, diluted with deionized water (DIW), was needed to cleanly etch away excess alloy materials. Since the upper contact materials were located only on the contact bumps,

fabrication induced stress (and device curling) normally associated with relatively thick sputtered layers, was not observed. The issue of electroplating non-unform Au structural layers was still present. Refer to Figure 45 for the following discussion.
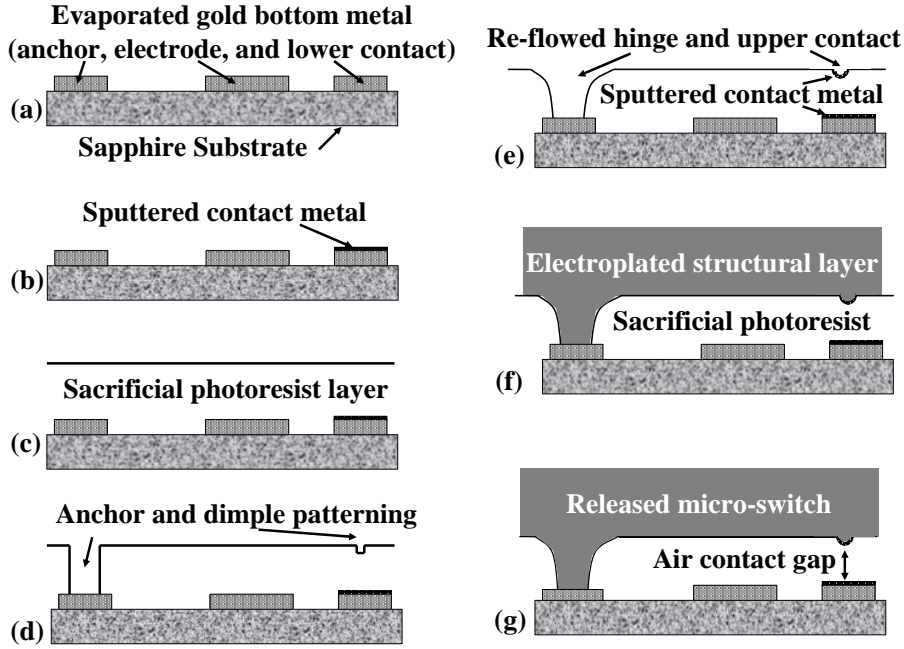
Figure 45   Illustration of the SNM02 fabrication process.

The actuation electrode and lower electric contact layers were approximately 3000 $\mathring{A}$ of evaporated Au patterned using a standard metal lift-off technique (**a**) [91]. A thin (200 $\mathring{A}$ thick) Cr layer was used under the evaporated Au layer to help the Au remain adhered to the substrate. The lower electric contact metal (500 $\mathring{A}$ thick) was sputter deposited and patterned using a metal lift-off technique (**b**). Due to the conformal nature of sputtered materials, "wings" or raised metal "edges" remain after performing sputtered metal lift-off.

The beam's gap or sacrificial layer thickness was 2 or 3 μm thick and was created using MicroChem's polydimethylglutarimide (PMGI) based photoresist (**c**) [102]. The different gap thickness were used to investigate its effect on pull-in voltage. The micro-switch's hinge geometry was defined in the sacrificial photoresist using standard photolithography techniques while the upper contact geometries were de-

fined by a partial expose and develop of the sacrificial photoresist layer (**d**). A timed re-flow in an oven with flowing nitrogen was used to reform the hinge and dimple areas into hemisphere-shaped upper contact bumps (**e**).

The upper contact metals (500 $\overset{\circ}{A}$ thick) were also sputter deposited, and patterned into the switch's dimple area using standard photolithography techniques (**e**). The excess metal (outside of the dimple area), however, was removed using an etch-back technique, instead of lift-off, to avoid damaging the sacrificial photoresist layer. The upper contact material, located only on the hemispherical-shaped upper contact, is highlighted in Figure 46.
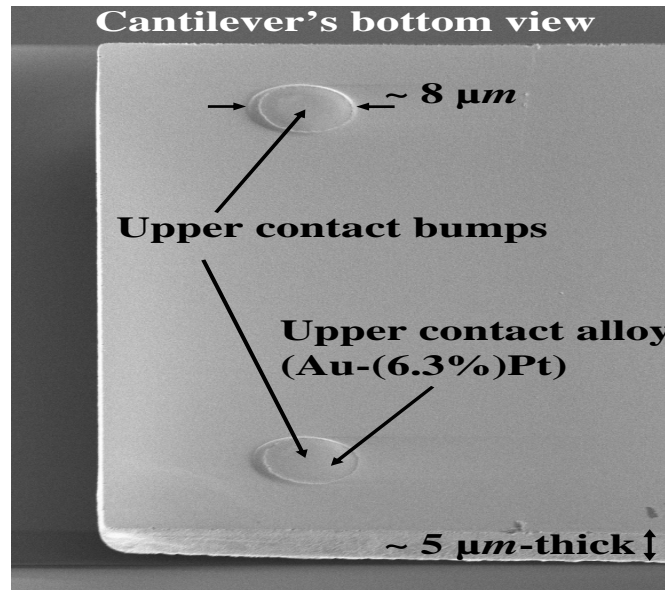
Figure 46   SEM image of a "flipped" over cantilever showing the alloy contact material on the hemisphere-shaped upper contact bumps located underneath the beam.

After electroplating the cantilever's gold structural layer (≈ 5 μm thick) (**f**), the devices were released using a CO_2 critical point dryer and tested to ensure proper operation and performance (**g**).

Figure 47 is a SEM image of an example metal contact micro-switch that was fabricated using the SNM02 fabrication process. Notice that the micro-switch

fabricated using this process is not curled or deformed, which indicates that the desirable, low stress attribute of the baseline process was maintained.
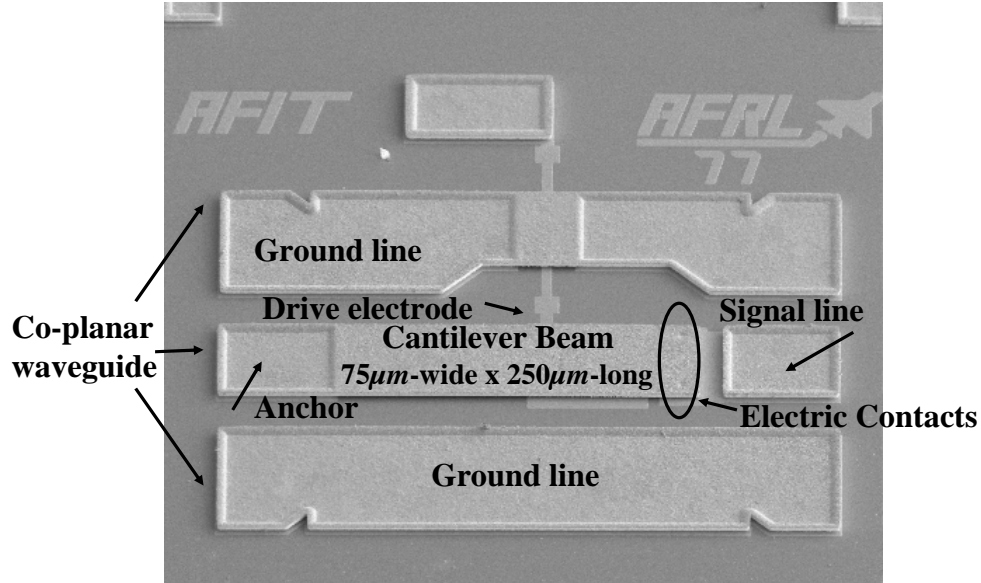
Figure 47   SEM image of an RF MEMS metal contact switch fabricated using the SNM02 process.

The wafers successfully fabricated using the SNM02 process are summarized in Table 16

Table 16   Wafers fabricated using the SNM02 process.

Wafer ID	Contact Metal/Alloy	Contact Geometry	Gap (μm)
SNM02-1	Au	Hemisphere	3
SNM02-2	Au	Hemisphere	2
SNM02-5	Au-(3.7at%)Pd	Hemisphere	3
SNM02-6	Au-(3.7at%)Pd	Hemisphere	2
SNM02-7	Au	Hemisphere	3
SNM02-8	Au	Hemisphere	2
SNM02-9	Au-(6.3at%)Pt	Hemisphere	3
SNM02-10	Au-(6.3at%)Pt	Hemisphere	2
SNM02-12	Au	Hemisphere	2

The SNM02 fabrication process followers, developed for this work, are provided in the Appendix B.

6.5 Summary

The AFRL/SND baseline fabrication process was a valuable starting point for this research. From this starting point, process modifications for incorporating sputtered metal alloy electric contacts and hemispherically-shaped upper contacts while using the SNM01 and SNM02 mask sets were developed. After fabrication, testing was accomplished to assess the performance of micro-switches with metal alloy electric contacts and to validate contact force and contact resistance models. The experiments and test results are discussed in chapter VII.

VII. Experiments and Results

Once the MEMS switch test structures with metal alloy electric contacts were designed and fabricated, micro-switch performance was assessed by conducting contact resistance, RF (insertion loss and isolation), and lifecycle tests. In addition, a nanoindentor was used to actuate micro-switches and validate contact force and contact resistance models. The same experimental setup was used to collect the contact resistance and lifecycle test data to ensure the results were comparable and that errors due to changes in the experimental set up were minimized. RF data, collected at AFRL/SND and AFRL/SNH, was used to substantiate the contact resistance data. Test results were affected by the non-uniformity of the electroplated Au structural layer discussed in Section 6.3. The non-uniform structural layer only allowed comparisons between similar or otherwise "comparable" devices. "Comparable" devices were defined as having the same micro-switch design and roughly the same pull-in voltage (and therefore approximately the same beam thickness). In addition to testing, micro-switch contact wear was assessed by investigating switched and un-switched electric contact pairs. The novel contributions to the MEMS field, discussed in this Chapter, are contact resistance, RF measurements, and micro-switch lifecycle test results of micro-switches with metal alloy electric contacts.

7.1 Nanoindentor Tests

Force versus deflection measurements were collected using an MTS Nanoindentor XP to manipulate actual micro-switches, like those shown in Figure 35. Figure 48 is an illustration of the experimental setup.

Prior to running the experiment the nanoindentor's piezoelectric indentor head was calibrated using the MTS calibration procedure. The indentor tip was then aligned with the optical microscope to ensure that the tip was accurately positioned over the center of the micro-switch during each test run. Nanoindentor test runs
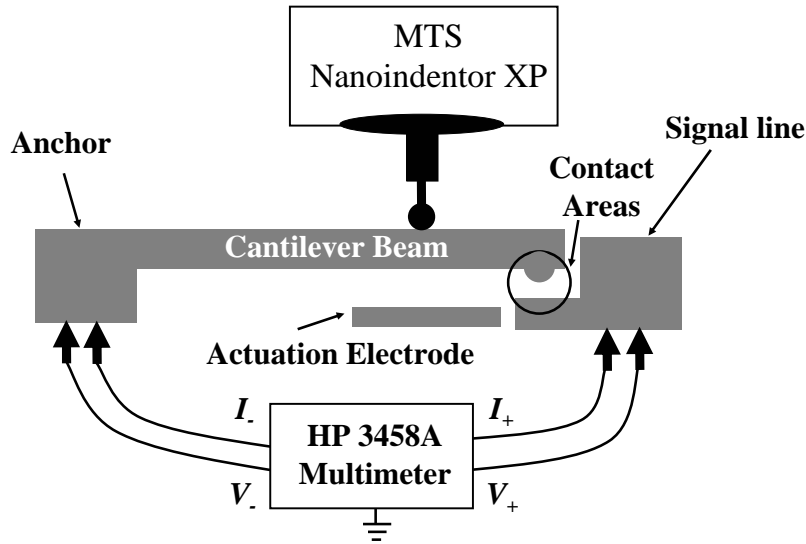
Figure 48   Experimental test setup used to simultaneously measure applied actuation force and contact resistance using a micro-switch.

were automated and could not be viewed in real-time optically. During each experiment, the nanoindentor's tip was positioned over the cantilever beam and used to push it down a fixed distance (i.e., the gap distance), at a constant rate, while measuring applied force. After reaching the fixed distance, a short hold segment (3-5 sec) was initiated prior to unloading the indentor head. The unload segment was set at a constant rate twice that of the load segment. This timing was needed in order to actuate the micro-switch slowly enough to collect stable resistance data and also avoid the nanoindentor's pre-programmed time limit for individual indents. A multimeter was used to measure resistance while the micro-switch closed.

The nanoindentor's surface-finding algorithm was set to a low sensitivity value (5 %) to ensure that the micro-switch being tested was not destroyed by the relatively high indentation forces associated with locating a surface. Consequently, a false prediction of the beam's surface was routinely observed during each experimental run. Engineering judgement was needed, during data reduction, to determine when the nanoindentor's tip impacted the beam surface and began to actuate the device. A spherical indentor tip with a 25 μm radius of curvature was used to ensure

minimum material indentation of the top surface of the cantilever beam. Minimum indentation was verified by performing a test indent, using the same parameters as the experiment, on an unused portion of the micro-switch's CPW which is made of the same material as the beam (i.e., electroplated Au).

The micro-switch test samples (6 individually wired micro-switches) were prepared by wire bonding the anchor and signal lines to a printed circuit board test fixture. The leads from the test fixture where connected to an HP3458A multimeter to measure closed switch resistance, in-situ, while actuating the device with the nanoindentor. The test equipment was connected to an IEEE 488 bus and the resistance measurements were collected using a PC. The nanonindentor's control computer was used to collect the force versus deflection measurements. The time of first measured resistance was noted while conducting the experiment and used to sync the nanoindentor and resistance data during data reduction. Contact resistance was found by subtracting the measured beam resistance (1.0 Ω) from the closed switch resistance measurements.

7.1.1 Beam Models. Figures 49 and 50 are representative plots of indentor tip deflection versus applied force and contact resistance data. Standard error bars are plotted on the measured data. The data shown on Figure 49 was collected while actuating a beam with an intermediate load positioned above the center of the actuation electrode. The data shown in Figure 50 was collected while actuating a beam with an end-load positioned between the upper contacts.

For comparison, Euler-Bernoulli models for a beam with fixed and free ends (Figure 10) and a beam with fixed and simply supported ends (Figure 12) are also plotted on Figures 49 and 50 [142]. From zero to approximately 1400 nm the beams are being actuated through an air gap and the measured spring constants are approximately 11.4 $\frac{N}{M}$ for the intermediately loaded beam and 11.3 $\frac{N}{M}$ for the end loaded beam. This compares to 16.3 $\frac{N}{M}$ and 13.0 $\frac{N}{M}$ from the intermediate and end

106
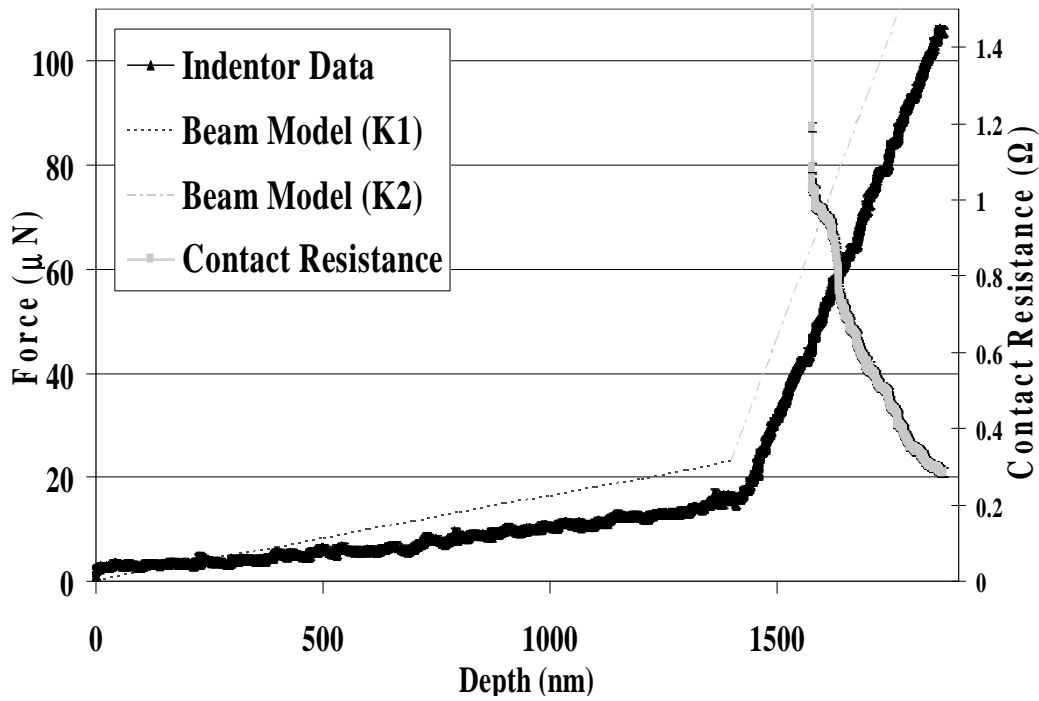
Figure 49   Representative plot of modeled and measured force versus indentor tip deflection and contact resistance data with the beam (i.e., D77 design) being actuated with an intermediate load using a nanoindentor (i.e., center of the beam and center of the bottom electrode).

loaded beam models, respectively. From approximately 1400 nm to approximately 1900 nm the micro-switch's upper and lower electric contacts are touching and once ohmic contact is established, at approximately 1600 nm, contact resistance is measured. The slope change at approximately 1400 nm indicates that the beam tip had traversed the air gap and that the micro-switch was closed. The force and contact resistance measurements will be compared to a contact resistance model in Section 7.1.4. The measured spring constant for a closed micro-switch with intermediate and end loads were approximately 202.1 $\frac{N}{M}$ and 217.0 $\frac{N}{M}$, respectively. This compares to 233.3 $\frac{N}{M}$ and 176.8 $\frac{N}{M}$ from the intermediate and end loaded beam models, respectively.

Overall, the measured and modeled spring constant data agree. Differences are primarily attributed to the models predicting beam tip deflection while the mea-

107
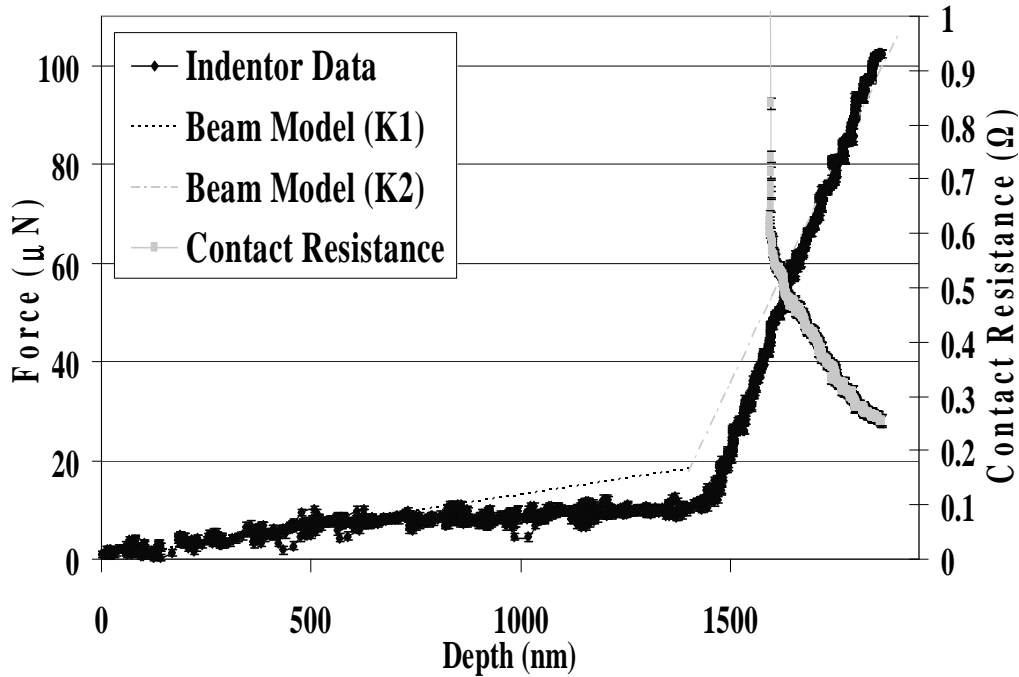
Figure 50   Representative plot of modeled and measured force versus indentor tip deflection and contact resistance data with the beam being actuated with an end load using a nanoindentor (i.e., center of the beam between the upper contacts).

surements were of the nanoindentor's tip movement. This claim is substantiated by the end load models, plotted on Figure 50, agreeing more closely with data than the intermediate load models, plotted on Figure 49. Variations in Young's modulus for Au (80 GPa was used in all the calculations), variations in micro-switch geometry (i.e., gap thickness, beam length, width, and thickness due to fabrication), variations in nanoindentor tip placement during each indent (i.e not located precisely at the beam's center) may also be contributing factors.

7.1.2   Improved Beam Model.   Figure 51 is a representative plot of modeled and measured indentor tip deflection versus applied force data.

For comparison, the model for intermediately loaded cantilever beam with a fixed end and a free end (Figure 10) is plotted along with the the improved beam model (Figure 11). The improved beam model's spring constant is approximately
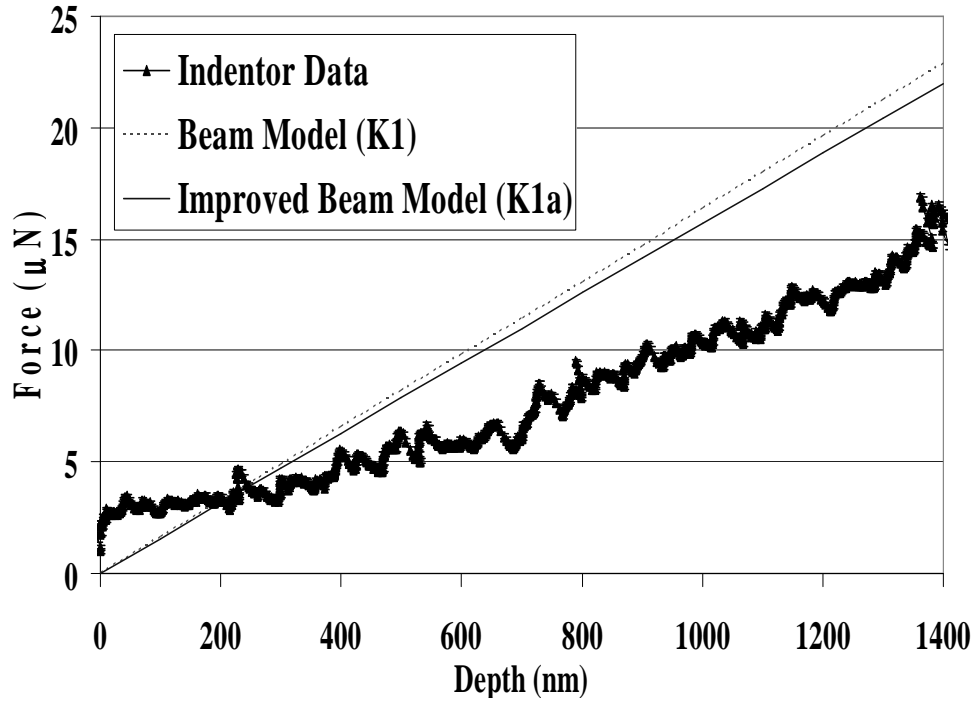
Figure 51   Representative plot of modeled and measured force versus indentor tip deflection data with the beam being actuated with an intermediate load using a nanoindentor (i.e., center of the beam and center of the bottom electrode).

15.7 $\frac{N}{M}$. Recall that the measured and simple cantilever spring constants were approximately 11.3 $\frac{N}{M}$ and 16.3 $\frac{N}{M}$, respectively. The percent difference between the simple cantilever model and the improved beam model spring constants was approximately 3.8%. Based on this small difference, Meng and Mehregany's improved beam model was not used. In addition, Rayleigh and Timoshenko beam theories were not invoked and the simple cantilever model using Euler-Bernoulli beam bending theory was used for all the analytic derivations [145, 155].

7.1.3   Contact Force Models.   In Section 3.7, contact force models that account for beam tip deflection and electric contact material deformation occurring after switch closure were developed. Previous work by this author, showed that contact force could be analytically modeled using the beam illustrated in Figure 12 [31]. Equation 22 is the resulting analytic contact force equation.

The new analytic contact force equations, based on an improved cantilever beam model (Figure 17), are derived by accounting for tip deflection [31] and assuming elastic, plastic, and elastic-plastic electric contact material deformation [24]. Euler-Bernoulli beam bending equations, the principle of superposition, material deformation models, and the single effective a-spot contact area model are used to derive the new equations.

Figure 52 is a representative nanoindentor tip deflection versus contact force plot (normalized for two contacts) that compares measured data and modeled values found using Equations 22, 43, and 47. Contact resistance data is plotted on Figure 52 for reference.
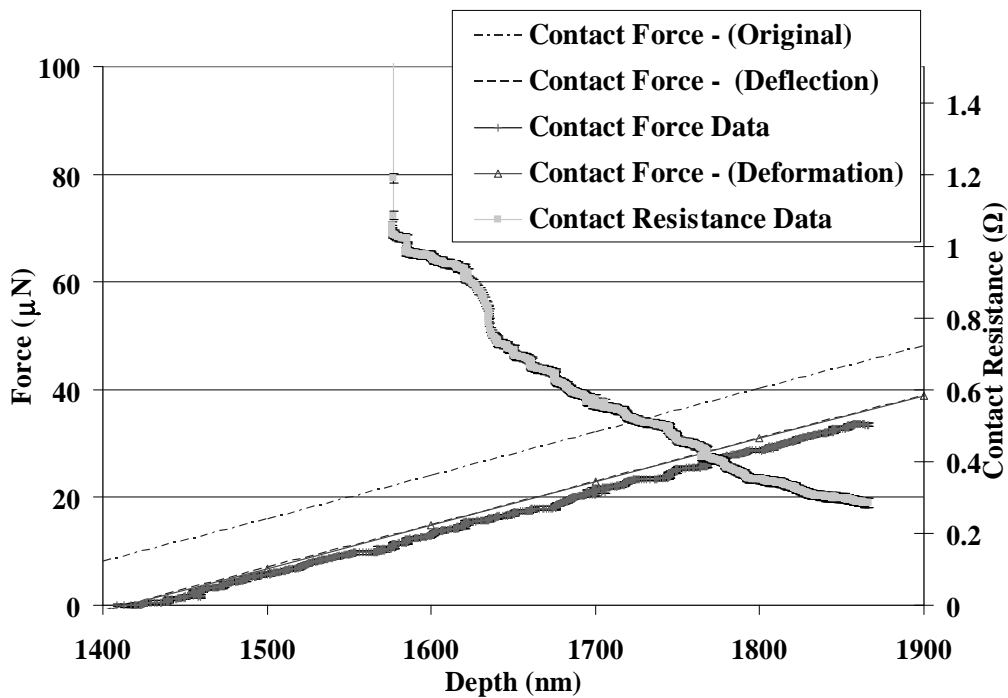
Figure 52   Representative plot of measured and modeled contact force versus indentor tip deflection data for an intermediate load. Contact resistance data is plotted for reference.

Figure 52 shows the modeled and measured contact force data to have the same slope. In addition, the contact force predicted using Equation 22 is shown to

110

overestimate the measured contact force by approximately 45% while the contact force predicted using Equation 43 is within 1% of the measured value. Contact force predictions found using Equation 47 virtually superimpose (percent difference of $\approx 0.11\%$) those found using Equation 43. This indicates that contact material deformation has little effect on micro-switch contact force. Based on this, Equation 43 was used to predict micro-switch contact force needed for modeling contact resistance.

7.1.4 Contact Resistance Model. The analytic micro-switch contact resistance model, presented in Section 3.10, was used to investigate contact resistance data collected while actuating micro-switches with a nanoindentor. Figure 53 is a representative contact force versus contact resistance plot (normalized for two electric contacts) that compares measured data and modeled, using Equation 53 and Equations 59 through 63, results. Indentor tip deflection versus contact force measurements and predictions, found using Equation 43, are also provided on Figure 53 for comparison.

Figure 53 shows good agreement between the modeled and measured contact resistance data. The measured contact resistance, however, does not coincide with micro-switch closure indicated by the slope change on Figures 49 and 50. This may be caused by ohmic contact initially being inhibited due to contaminant film layers present on the contacts [77, 78]. Ohmic contact, however, was observed once the contaminant layers were ruptured, resulting in metal-to-metal contact. The force needed to rupture the contaminant film layers, annotated on Figure 53 as F_{R}, and create ohmic contact was approximately 15 μN. This result agrees with Hyman et al.'s observations [62].

In addition, since the two data sets were collected using the same micro-switch with approximately 45 minutes between experiments, contaminant films of approximately the same thickness (i.e., several monolayers of adsorbed contaminants) were
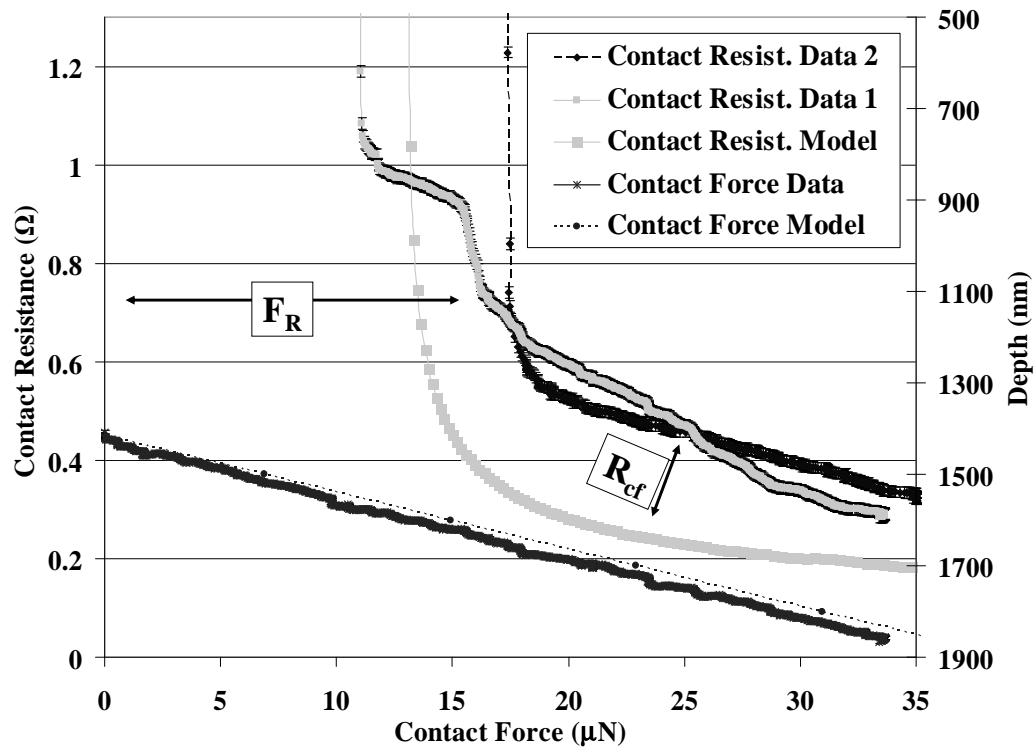
Figure 53   Representative plot of contact resistance versus contact force measurements and modeled data. Contact force versus indentor tip deflection data are plotted for reference.

certainly present during each experiment [59, 62]. This hypothesis is substantiated by F_R being approximately the same for each experiment (i.e., the first experiment did not "clean" the contacts for the second experiment). Once ohmic contact was established, a small contaminant film resistance contributed to the measured contact resistance. As expected, this resistance, annotated on Figure 53 as R_{cf}, decreases as the contact force increases. Next, micro-switch contact resistance, RF, and Lifecycle test results are presented.

7.2   Contact Resistance Tests

A series of 20 SNM01 micro-switches, like that shown in Figure 44, and 20 SNM02 micro-switches, like that shown in Figures 35 and 36 (i.e., 10 of each design), were tested to experimentally characterize the contact resistance for micro-switches

with Au and Au alloy electric contacts. The SNM01 micro-switches were fabricated with sputtered Au, bi-metallic (i.e., Au-on-Au-(6.3at%)Pt), binary alloy (i.e., (Au-(3.7at%)Pd), and ternary alloy (i.e., Au-(5at%)Pt-(0.5at%)Cu) electric contacts while the SNM02 micro-switches were fabricated with sputtered Au and binary alloy (i.e., Au-(6.3at%)Pt and Au-(3.7at%)Pd) electric contacts.

The micro-switches were tested at AFRL/SND by wafer probing using a Alessi Rel-4100A Microprobe Station with standard microprobes. The actuation voltage was applied using an HP 3245A universal source and a Krohn-Hite wideband amplifier. Closed switch resistance was measured using an HP 3458A multimeter in a four-point probe configuration. Contact resistance was determined by subtracting the measured resistance of the cantilever beam from the measured closed switch resistance values. Data were collected each time the actuation voltage was incremented. Figure 54 is a schematic illustration of the experimental setup.
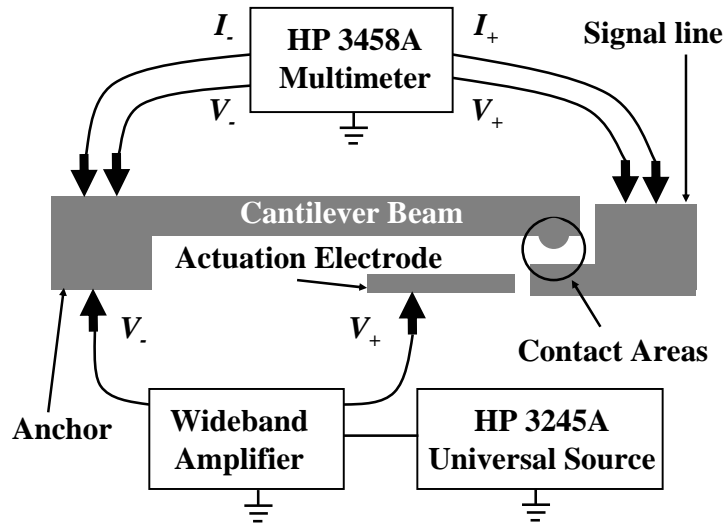
Figure 54   Experimental test set up used to measure contact resistance and collect micro-switch lifecycle data.

During contact resistance testing of the SNM01 micro-switches, a voltage ranging from 0 to 120 V in 0.5 V increments was applied between the cantilever beam and the actuation electrode. The micro-switch closed when the actuation voltage

113

exceeded the pull-in voltage. As the applied voltage was increased, beyond the pull-in voltage, contact force increases and contact resistance decreases. This test was accomplished twice for each micro-switch with approximately 10-15 seconds between the experiments. The average minimum contact resistance data, with 120 V of applied actuation voltage, are summarized in Table 17. Beam collapse was not observed while testing these micro-switches.

Table 17   Average minimum contact resistance measurements for SNM01 micro-switches.

Metal/Alloy	R_c / StdDev Experiment 1	R_c / StdDev Experiment 2
Au	0.94 / 0.20	0.83 / 0.19
Au-(3.7at%)Pd	1.23 / 0.13	1.17 / 0.16
Au-on-Au-(6.3at%)Pt	1.13 / 0.19	0.99 / 0.07
Au-(5at%)Pt-(0.5at%)Cu	0.34 / 0.33	0.33 / 0.30

Table 17 shows that the average minimum contact resistance (for the binary alloy contacts) measured during experiment one was higher than that measured during experiment two. This may be a result of adsorbed contaminant film layers being "wiped" away from the electric contact's surface during the first experiment. Table 17 also shows that the micro-switches with ternary alloy contacts have lower measured average contact resistance with larger standard deviations. This may be an indication that the ternary alloy, deposited during device fabrication, was a two-phase or a three-phase alloy with different micro-switches containing a different percentage of each material phase.

Table 17 also shows the contact resistance standard deviation for micro-switches with Au-(5%)Pt-(0.5%)Cu contacts have the highest standard deviation. This will be address later.

Contact resistance data, from a representative micro-switch with Au electric contacts, and simulated contact resistance, calculated using Equations 60 and 63, and measured material properties, are plotted on Figure 55.

The data presented on Figure 55 shows a sharp decrease in contact resistance at approximately ≈ 93 V for micro-switches tested the first time. This drop in measured contact resistance was consistent and occurred between 90 V and 98 V for all the SNM01 micro-switches tested. This anomaly may have been caused by a difference in upper contact height where only one contact actually conducts (i.e., modeled as a single series resistor) from pull-in to ≈ 90 V and the second contact conducts after the observed sharp decrease in contact resistance (i.e., modeled as a parallel resistor network). Another explanation of this anomaly is the rupturing or fritting of a contaminant film layer [59]. This claim is substantiated by less drastic drops in contact resistance during experiment two where the contaminant film was "cleaned" off during the first experiment. Also, since none of the SNM01 micro-switches exhibited beam collapse mechanical contact cleaning due to contact friction (caused by beam bending) was mostly likely minimal. This device failed due to stiction.
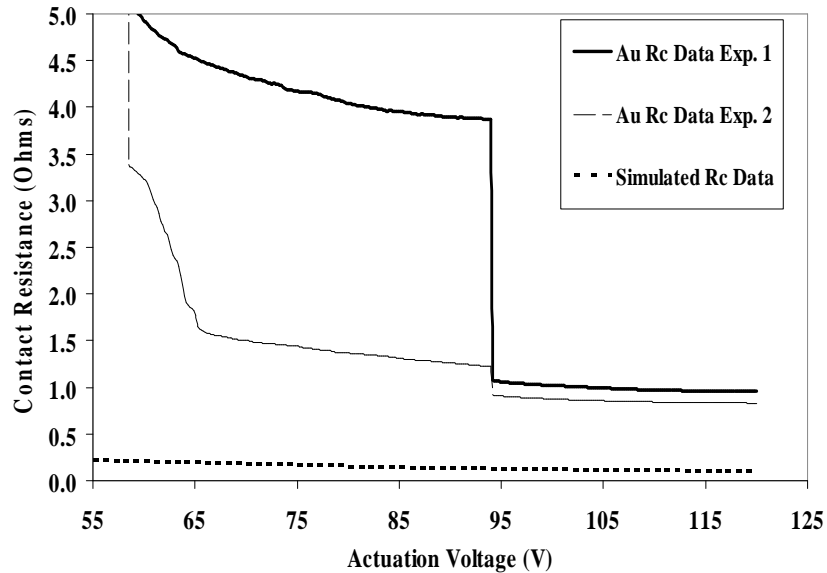
Figure 55   Contact resistance data for a representative SNM01 micro-switch with sputtered Au electric contacts.
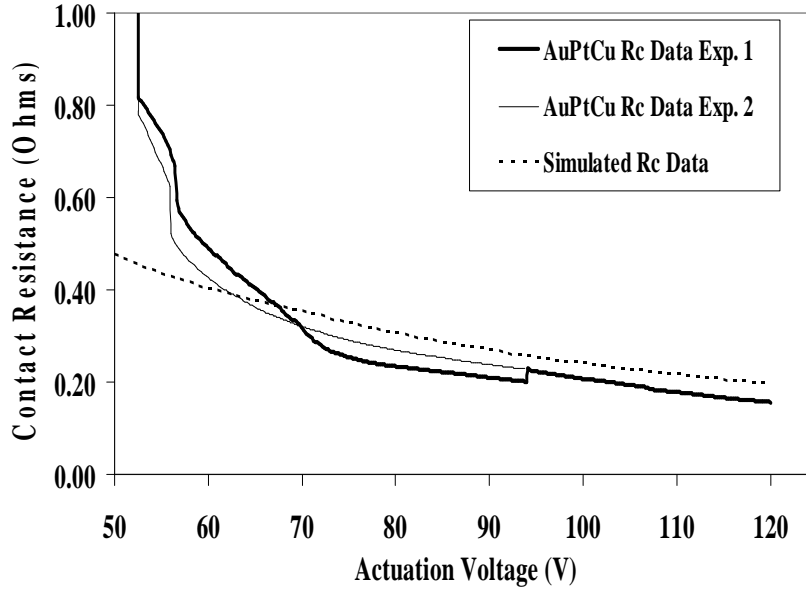
Figure 56   Contact resistance data for a selected SNM01 micro-switch with Au-(5at%)Pt-(0.5at%)Cu electric contacts.

Figure 56 shows measured and simulated contact resistance for micro-switches with Au-(5at%)Pt-(0.5at%)Cu electric contacts. The measurements, shown on Figure 56, are somewhat lower than the simulated values and fritting is less obvious. This may be a result of the single effective asperity model, used in this study, not accurately representing the actual contact area for micro-switches with contact alloy. Recall that Majumder et al. showed a contact resistance lower limit using the multiple asperity-based model and an upper limit using the single effective asperity-based mode.

In addition, during experiment one a resistance increase from 0.20 to 0.22 Ω was measured at $\approx 93\,V$. Localized contact area heating may have caused either a change in ternary alloy phase or the formation of an intermetallic compound resulting in this small resistance increase. This hypothesis is supported by data, collected during the second experiment, that are higher than data collected during the first experiment (i.e., between 70 V and 93 V). For actuation voltages higher than $\approx 93\,V$ the measured resistance values from both experiments agree. This may indicate that

116

the contact material experienced a phase change during experiment one and was in a stable state during experiment two. This anomaly could also be explained by material deformations caused by non-uniform contact pressure or contact surface changes caused by material transfer.

This anomaly was not observed in micro-switches with binary alloy contacts, most likely, because their alloy compositions avoided miscibility gaps and the formation of intermetallic compounds [112].

During contact resistance testing of the SNM02 micro-switches, a voltage ranging from 0 to 110 V in 0.5 V increments was applied between the cantilever beam and the actuation electrode. As the applied bias was increased beyond the pull-in voltage, the contact force was increased until the beam, shown in Figure 35, collapsed onto the drive electrode at the collapse voltage. Once collapsed, the micro-switch shorted out and was no longer operable. Beam collapse was not observed in the micro-switches, shown in Figure 36, due to the mechanical switch design (i.e., the electrostatic and contact forces were co-located in the vicinity of the electric contact bumps). The maximum contact force and minimum contact resistance occurred just prior to the beam collapse voltage or at the maximum applied voltage. As the applied voltage was increased, beyond the pull-in voltage, contact force increased and contact resistance decreased. Table 18 summarizes the minimum average contact resistance measurements.

Contact resistance versus actuation voltage data, for selected micro-switches, are plotted on Figures 57 (SNM02 D77 design) and 58 (SNM02 D20 design).

Figure 57 (SNM02 D77 design) shows that pull-in and beam collapse voltages are located at the lower end of the voltage axis (higher contact resistance values) and the higher end of the voltage axis (lower contact resistance values), respectively. Minimum contact resistance is observed immediately prior to reaching the beam collapse voltage. Once the beam collapses onto the actuation electrode, the D77 micro-switch shorts out and is no longer operable. The pull-in voltage, collapse

117

Table 18　　Average minimum contact resistance measurements for SNM02 micro-switches.

Metal/Alloy	Min Ave R_c (Ω) / StdDev (Ω) Experimental
D77 micro-switch design	
Au	1.20 / 0.04
Au-(6.3at%)Pt	1.59 / 0.40
Au-(3.7at%)Pd	1.75 / 0.27
D20 micro-switch design	
Au	1.53 / 0.50
Au-(6.3at%)Pt	1.74 / 0.17
Au-(3.7at%)Pd	1.82 / 0.25
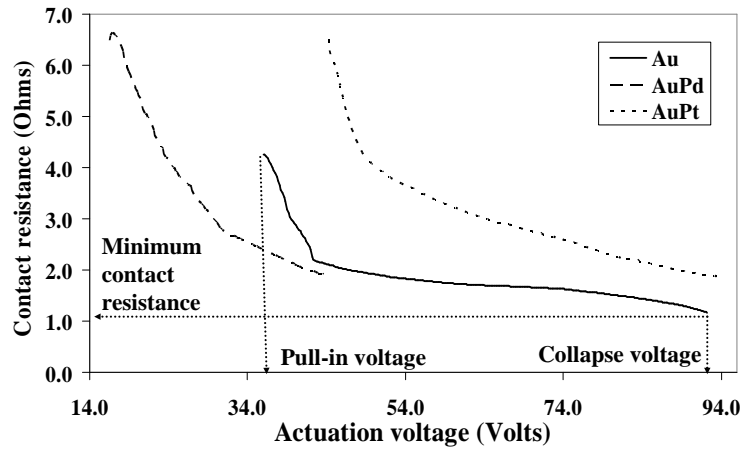
Figure 57　　Contact resistance versus actuation voltage data plots for selected SNM02 D77 design micro-switches. the pull-in voltage, collapse voltage, and minimum contact resistance are labelled for the micro-switch with Au contacts.

voltage, and minimum contact resistance, for a micro-switch with sputtered Au electric contacts, are highlighted on Figure 57.

Figure 58 (SNM02 D20 design) shows pull-in voltages, located at the lower end of the voltage axis, and minimum contact resistance values, located at the higher end of the voltage axis. A sharp decrease in contact resistance, labelled as the "wings" collapse voltage' on Figure 58, was observed. This anomaly may have been caused by a difference in upper contact height where only one contact actually conducts (i.e., modeled as a single series resistor) until the abrupt change and the second contact

118
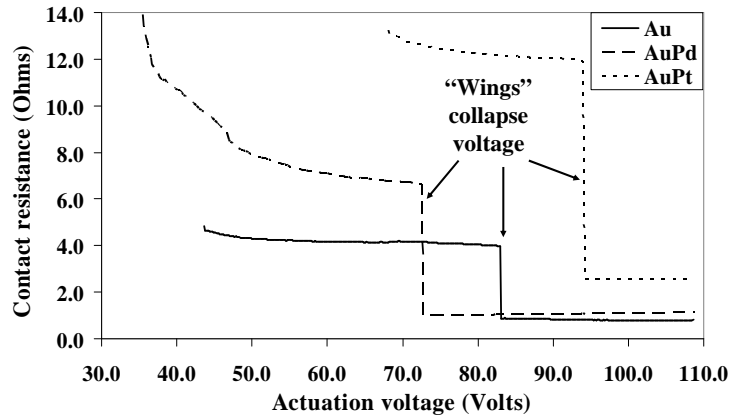
Figure 58   Contact resistance versus actuation voltage data plots for selected SNM02 D20 design micro-switches.

conducts after the sharp decrease in contact resistance (i.e., modeled as a parallel resistor network). This anomaly could also be explained by the SNM02 D20 micro-switch upper contacts impacting the bottom contact "wings" prior to reaching the planar portion of the bottom contact. The height of the "wings," estimated using SEM images, ranged from approximately 0.2-0.5 μm. Figure 59 shows an SNM02 D20 micro-switch electric contact pair from a device with Au-(6.3at%)Pt contacts and $\approx 8.8 \cdot 10^8$ switch cycles. Material transfer, from the lower contact "wing" to the upper contact hemisphere is highlighted.
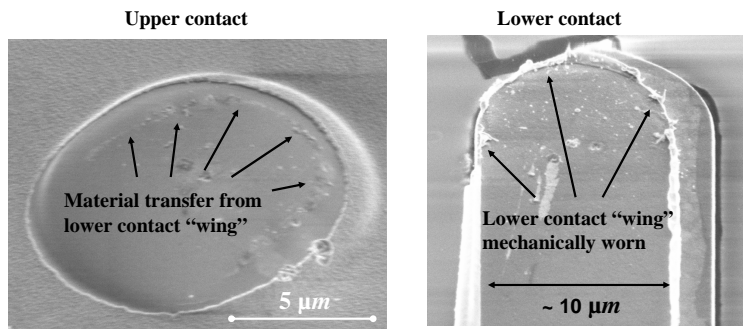
Figure 59   A captured video image illustrating contact wear of an SNM02 D20 Au-(6.3at%)Pt electric contact pair with $\approx 8.8 \cdot 10^8$ switch cycles.

119

The measured contact resistance values for micro-switches with metal alloy electric contacts were higher than for devices with Au electric contacts. In addition, the SNM01 design did not exhibit beam collapse and had the best contact resistance performance. This may be due to the mechanical design of the switch which enabled mechanical contact cleaning (i.e., "wiping") and provided adequate contact force. The SNM02 D77 design exhibited collapse due to mechanical switch design (i.e., the beam was longer and less stiff than the SNM01 devices) and the beam's geometry. The useful voltage range (between the pull-in and collapse voltages) was sufficient, however, for evaluating the contact resistance effects of using alloy electric contacts. The SNM02 D20 designs did not exhibit beam collapse but the contact resistance performance was significantly less than expected until reaching the "wings" collapse voltage. RF data, collected from devices fabricated during this study, is discussed next.

7.3 RF Tests

A limited amount of full wafer, automated RF insertion loss and isolation testing was accomplished at AFRL/SND by probing selected devices with an Electroglas 2001X automatic RF probe station and measuring RF data with an HP8510C network analyzer. The micro-switches were actuated using an Agilent 33250A arbitrary function generator, a wideband amplifier, using a PC connected via an IEEE 488 computer interface. The S-parameters were measured at 10 GHz using a calibrated -10 dBm signal while the micro-switches were open (isolation) and closed (insertion loss) with pull-in voltage applied. Insertion loss data with increased contact force (i.e., actuation voltages greater than the pull-in voltage) were not collected during the full wafer RF tests. Table 19 summarizes the full wafer S-parameter data.

The non-uniform electroplated Au structural layer skewed the full wafer RF data. This is evidenced by the large standard deviation values. The RF data, however, does correspond to the contact resistance values presented in Section 7.2.

Table 19   Full wafer RF insertion loss and isolation measurements collected at 10 GHz.

Metal/Alloy	Pull-in / StdDev (V)	IL / StdDev (dB)	Isolation / StdDev (dB)
SNM02 D77			
Au	53.6 / 14.4	0.8 / 0.3	18.7 / 1.2
Au-(6.3at%)Pt	55.3 / 11.3	0.9 / 0.3	18.8 / 1.2
Au-(3.7at%)Pd	31.6 / 8.9	0.2 / 0.2	13.5 / 2.0
SNM02 D20			
Au	47.0 / 7.5	0.8 / 0.2	23.1 / 0.4
Au-(6.3at%)Pt	60.0 / 8.9	1.1 / 0.3	22.4 / 0.4
Au-(3.7at%)Pd	34.5 / 9.6	0.7 / 0.3	19.3 / 0.7

Additional S-parameter testing on selected micro-switches was accomplished at AFRL/SNH. This testing, with actuation voltages greater than the pull-in voltage, was done using an Agilent network analyzer and Cascade Microtech probes. A Short, Open, Load, Thru (SOLT) calibration was performed using a Cascade Microtech impedance standard substrate. Device actuation voltages were applied using a coaxial needle probe and an Agilent HP3245A Universal Source. Table 20 summarizes the S-parameter data that was collected at AFRL/SNH.

Table 20   RF insertion loss and isolation measurements, from selected micro-switches, collected at 10 GHz.

Design	Actuation (V)	IL (dB)	Isolation (dB)
SNM02 D77 with Au contacts			
	0.0		19.5
	40.0	1.6	
	50.0	0.5	
	60.0	0.4	
	70.0	0.3	
	80.0	0.2	
	90.0	0.1	
SNM02 D20 with Au contacts			
	0.0		22.0
	80.0	0.2	
	90.0	0.2	

The RF insertion loss performance for the SNM02 D77 and D20 designs were similar. With actuation voltages equal to 80.0 V and 90.0 V the insertion loss measurements ranged from approximately 0.1-0.2 dB at 10 GHz for both the D77 and D20 designs. This result was consistent with the contact resistance data presented in Section 7.2 that shows contact resistance measurements between $\approx 1 - 2~\Omega$. In addition, the data in Table 20 shows the same trend as that shown in Section 7.2 where increased actuation voltages resulted in lower insertion loss (or contact resistance). A rule of thumb for comparing RF insertion loss and contact resistance, based on Equations 66 and 67, is that 0.1 dB of IL is $\approx 1~\Omega$ of contact resistance.

7.4   Micro-Switch Lifetime Tests

During lifecycle testing of SNM01 devices with alloy contacts, the micro-switches were actuated with a 50% duty cycle square wave input. The waveform's "on" voltage level was set to the pull-in voltage plus approximately 1-3 V for increased contact force. The input waveform was a square wave with a frequency that was set below the beam's resonant frequency (50 kHz). The micro-switches were cycled continuously until they failed open (i.e., infinite resistance) or closed (i.e., stuck down). Contact resistance data were collected every 30 seconds by increasing the input waveform's duty cycle to 90% and lowering its frequency to 1 Hz for 2 seconds. The multimeter's open circuit voltage ($\approx 8.2~V$ current limited to 10 mA) was present on the electric contacts for all the switching events (i.e., "hot-switching"). The environment was lab ambient with average temperatures and relative humidities ranging from $\approx 68 - 72°$C and 25-35%, respectively. The failure criteria for this testing was measured contact resistance greater than $\approx 2~\Omega$ for closed micro-switches and contact resistance less than $\approx 1~\Omega$ for open micro-switches (i.e., devices that failed due to stiction). The micro-switches with Au, binary alloy (i.e., Au-(3.7at%)Pd), and bi-metallic (i.e., Au-on-(Au-(6.3at%)Pt)) contacts failed closed while the micro-switches with ternary alloy (i.e., Au-(5at%)Pt-(0.5at%)Cu) failed open.

122

Micro-switch contact resistance versus the number of switch cycles is plotted for selected SNM01 devices on Figure 60. The raw data was curve fitted with trendlines for micro-switches with different contact metals.
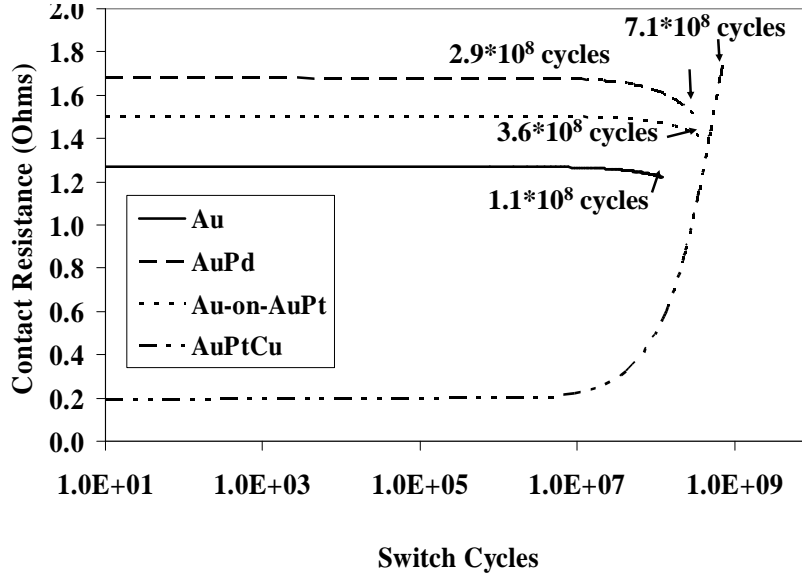
Figure 60   SNM01 micro-switch contact resistance versus switch cycles data plot.

The micro-switches with bi-metallic (Au-on-Au-(6.3at%)Pt) and binary alloy (Au-(3.7at%)Pd) contacts resulted in contact resistance between $1 - 2$ Ω and, when compared to micro-switches with sputtered Au electric contacts, exhibited increased switching lifetimes. The micro-switches with ternary alloy (Au-(5at%)Pt-(0.5at%)Cu) electric contacts resulted in contact resistance ranging from 0.2–1.8 Ω and, when compared to micro-switches with sputtered Au electric contacts, exhibited increased switching lifetimes. This was most likely due to the increased material hardness of the sputtered metal alloys. The measured Meyer hardness of evaporated Au, sputtered Au, Au-(3.7at%)Pd, Au-(6.3at%)Pt, and Au-(5at%)Pt-(0.5at%)Cu thin films were approximately 1.0 GPa, 1.7 GPa, 1.9 GPa, 2.0 GPa, and 2.2 GPa, respectively.

The micro-switch with Au-(5at%)Pt-(0.5at%)Cu contacts exhibited increased contact resistance with increased numbers of switch cycles. The plot on Figure 60

123

shows a steady rise in contact resistance between 10^7 and $7.1 \cdot 10^8$ switch cycles. This may indicate that a carbon-based contaminant film was developing with increased switch cycles or possibly that a material phase change occurred. A detailed investigation of ternary alloys, not accomplished in this study, is recommended in Chapter VIII.

The same procedure was used during the SNM02 micro-switch lifecycle testing. The failure criteria was adjusted to measured contact resistance values greater than approximately 3.5 Ω for closed micro-switches (due to the increased contact resistance exhibited by the D20 designs possibly due to the sputter lift-off "wings") and contact resistance less than ≈ 1 Ω for open micro-switches (i.e., devices that failed due to stiction). Contact resistance versus switch cycle raw data, for selected micro-switches, was curve fitted and the resulting trendlines were plotted on Figure 61. The D77 micro-switch with Au contacts failed closed while the micro-switch with Au-(6.3at%)Pt contacts failed open. The D20 micro-switches, with Au and Au-(6.3at%)Pt contacts, failed closed.
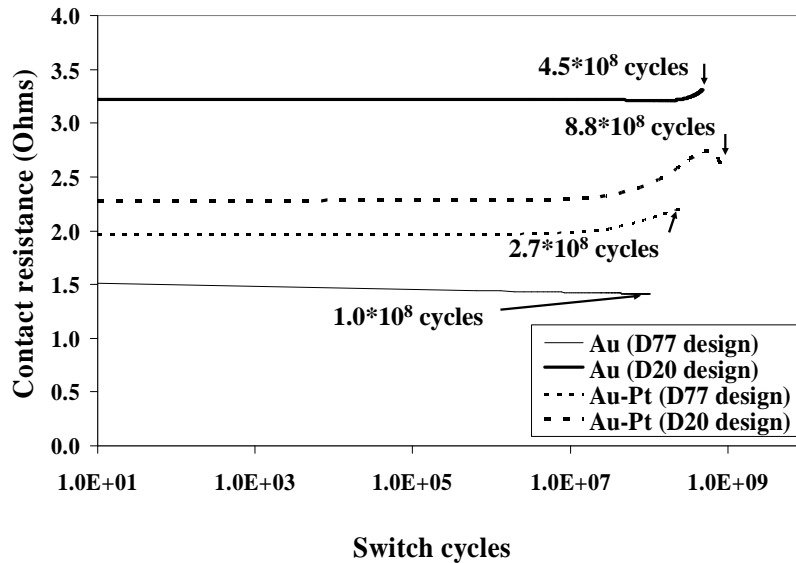

Figure 61   SNM02 micro-switch contact resistance versus switch cycles data plot.

SNM02 micro-switches fabricated with Au-(3.7at%)Pd electric contacts were not effectively lifecycle tested because all of the devices exhibited lower than expected restoring force due to having a thinner than expected (i.e., $\approx 3.2 - 4.2 \ \mu m$ versus $\approx 5 \ \mu m$ for all the other wafers) electroplated Au beam thickness. The low restoring force was evidenced by the lower pull-in voltages ($\approx 15 - 25 \ V$), for micro-switches on the Au-(3.7%)Pd wafer, than for micro-switches ($\approx 40 - 60 \ V$) on the other wafers.

Generally, micro-switches with evaporated Au electric contacts are limited to approximately 10^6 "hot-switched" cycles because evaporated Au is a soft metal and prone to wear [92]. Majumder et al. reports greater than 10^7 "hot-switched" cycles and approximately 10^{11} "cold-switched" cycles for devices with a "platinum group" electric contact metal [92]. The SNM02 (D77 design) micro-switches with Au-(6.3at%)Pt contacts were "hot-switched" and resulted in contact resistance between $1.5 - 2.2 \ \Omega$ and, when compared to micro-switches with sputtered Au electric contacts, increased switching lifetimes. The SNM02 (D20 design) micro-switches with Au-(6.3at%)Pt contacts resulted in contact resistance between $2.2 - 3.3 \ \Omega$ and, when compared to micro-switches with sputtered Au electric contacts, also exhibited increased switching lifetimes. Once again, this was most likely due to the increased material hardness of the sputtered alloy contact films. The measured Meyer hardness of evaporated Au, sputtered Au, and co-sputtered Au-(6.3at%)Pt thin films (500 $\mathring{A}$-thick) were approximately 1 GPa, 1.7 GPa and 2.0 GPa, respectively.

7.5   Wear Assessment

Gold-platinum alloy Au-(6.3at%)Pt electric contact wear was assessed by comparing thin film material properties, micro-switch lifecycle test results, and SEM images (i.e., qualitative analysis) of switched and not yet switched micro-switch contacts. A quantitative contact surface composition analysis was attempted but not successfully completed.

Figure 62 are SEM images of an SNM02 (D77 design) micro-switch showing the structural and electric contact layers.
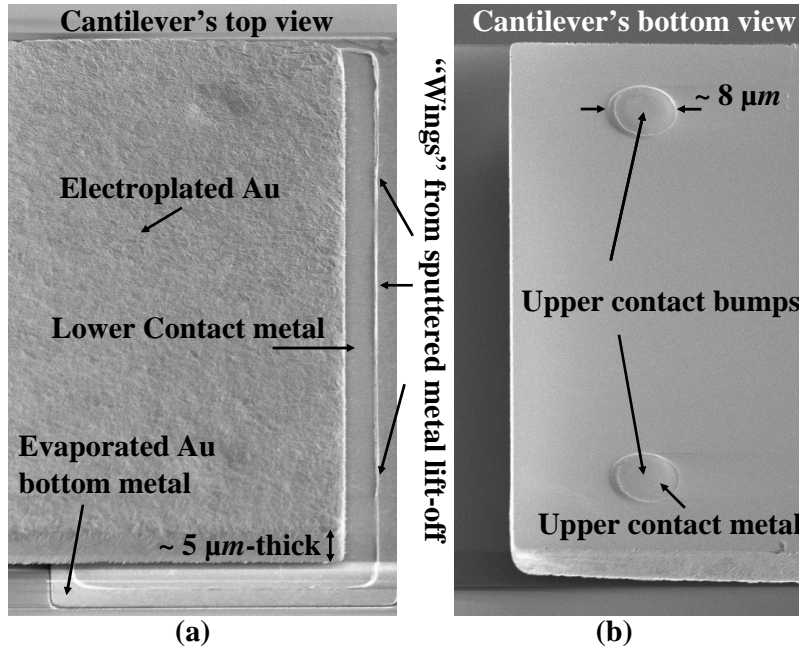
Figure 62   SEM images of an SNM02 micro-switch structural and electric contact layers: (a) Top view of the electroplated Au structural layer with a view of the evaporated adhesion and sputtered lower electric contact layers. (b) View of the underside of a beam revealing sputtered contact metal on top of the un-switched hemisphere-shaped upper contacts.

Figure 62 (a) shows the top view of the electroplated Au structural layer, the evaporated adhesion layer, and the sputtered lower electric contact layer. Sputter lift-off "wings," discussed earlier, are also noted on the image. The sputtered lower contact metal is well adhered to the evaporated Au adhesion layer and shows no signs of delamination. The hemisphere-shaped upper contacts, shown in Figure 62 (b), have not been switched yet and show sputtered contact metal only on the contact bumps. The sputtered contact metal (i.e., alloy) is also well adhered to the seed metal with no indications of delamination. The seed metal, located on the underside of the entire beam, is needed for electroplating the micro-switch's Au structural layer.

Figure 63 are SEM images of an SNM02 micro-switch's upper contacts made from Au-(6.3at%)Pt contact material that has been cycled for $2.7 \cdot 10^8$ "hot-switch" cycles.
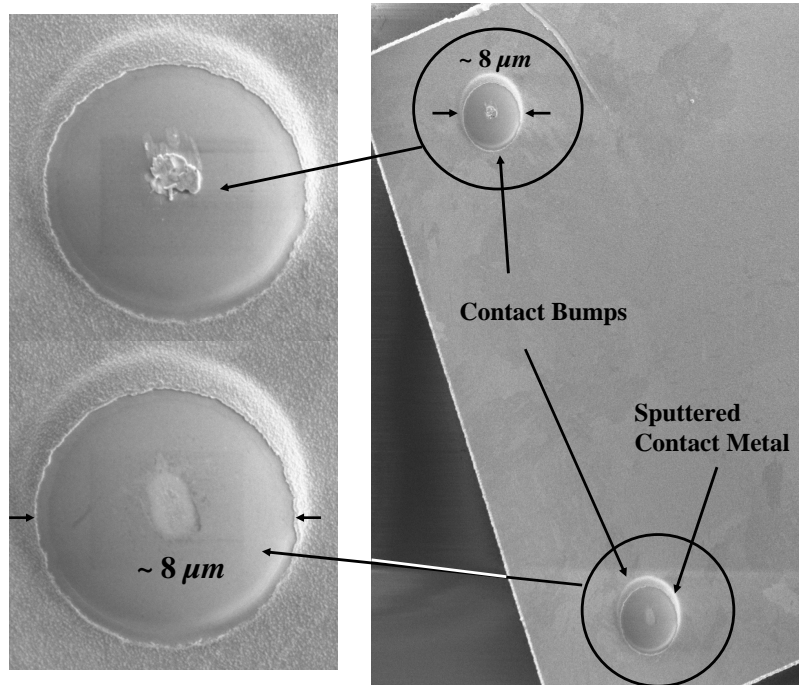
Figure 63   SEM images of an SNM02 micro-switch's underside revealing sputtered contact metal (Au-(6.3at%)Pt) on top of hemisphere-shaped upper contacts. The device has been actuated for $2.7 \cdot 10^8$ "hot-switch" cycles.

Contact wear is clearly noted on both contacts while actual material transfer is only shown on the top contact. Despite this, the contact metal remains well adhered to the contact bump and shows no signs of rubbing off or delamination due to repeated switch cycling.

Figure 64 are SEM images of a matched set of upper and lower electric contacts (Au-(6.3at%)Pt) for an SNM02 micro-switch that has been cycled for $2.7 \cdot 10^8$ "hot-switch" cycles. Material transfer, from lower to upper contact, is clearly noted on Figure 64.

SEM/ energy dispersive x-ray analysis (EDX) data showed evidence of the individual alloy components (i.e., Au and Pt) and the presence of contaminants (i.e., C
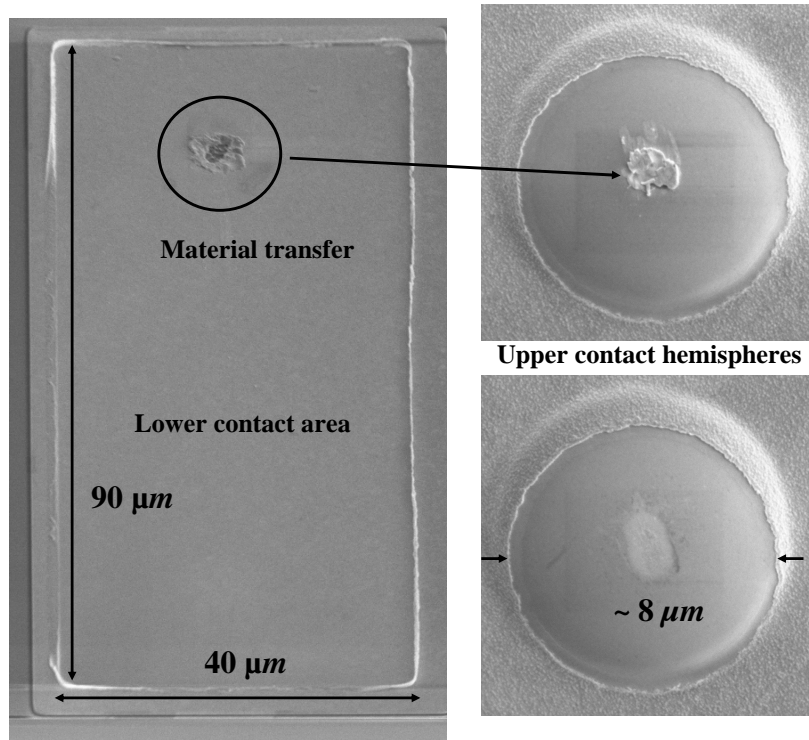
Figure 64   SEM images of a matched set of SNM02 micro-switch Au-(6.3at%)Pt electric contacts that have been actuated for $2.7 \cdot 10^8$ "hot-switch" cycles.

and O) in the contact area. Carbon and oxygen contaminant layers, normally found on test samples exposed to laboratory ambient, are not necessarily indicative of the contaminant films theorized to cause micro-switch failures. XPS analysis, used for evaluating the thin alloy film test specimens in Chapter IV, was planned but the minimum spot size (i.e., 100 μm in diameter) was too big to collect meaningful data from the small (i.e., $\approx 1 - 2$ μm in diameter) contact area. Auger electron spectroscopy (AES) was accomplished using a smaller spot size (i.e 15 μm in diameter) but, unfortunately, substrate charging caused the electron beam to wander. The wandering beam caused significant problems because longer dwell times were required (with the smaller spot size) to achieve an adequate number of counts necessary for a surface composition analysis. Therefore, the precise composition of the worn electric contact material is not known.

Figure 65 are SEM images of SNM02 (design D77) micro-switch lower contacts (Au-(6.3at%)Pt) with increasing numbers of switch cycles.

(a)   **(b)**   **(c)**
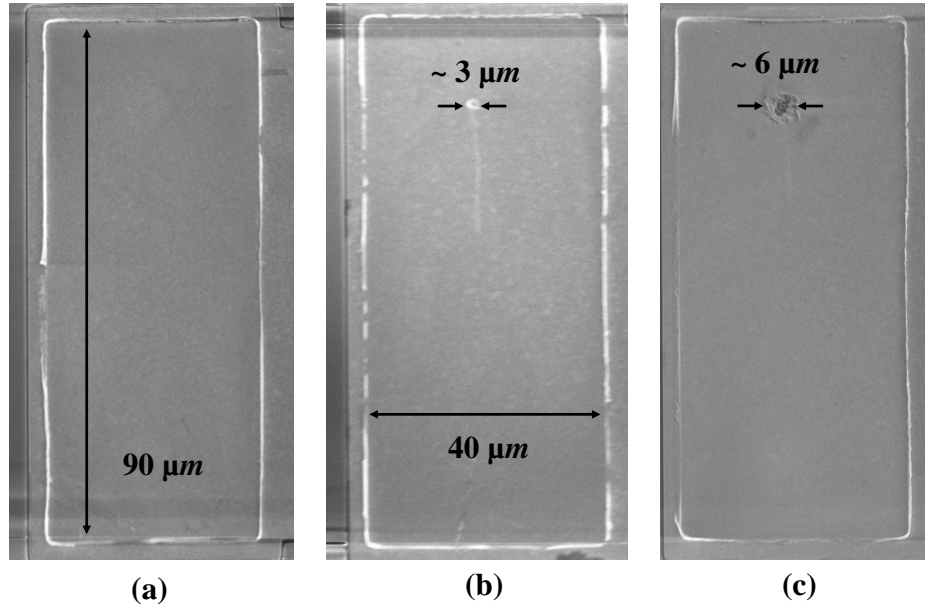
Figure 65   SEM images of SNM02 micro-switch lower contacts (Au-(6.3at%)Pt) with the following numbers of switch cycles: (a) zero switch cycles (b) $1.0 \cdot 10^8$ switch cycles (c) $2.7 \cdot 10^8$ switch cycles.

Figure 65 compares the lower contacts of three different micro-switches with different numbers of cycles. The micro-switch lower contact, shown in Figure 65 (a), was not operated while the micro-switches shown in Figures 65 (b) and 65 (c) were lifecycle tested until achieving $1.0 \cdot 10^8$ (i.e., still operable) and $2.7 \cdot 10^8$ (i.e., failed open with $R_c > 1 \cdot 10^{38}$ Ω)) cycles, respectively. The wear spot on the top lower contact appears to be increasing in diameter with increased numbers of switch cycles while the bottom lower contact shows no visible signs of wear. In addition, the failure that occurred while testing this device in Figure 65 (c) was catastrophic did not show a gradual decline in performance. This seems to indicate that a micro-arc due to "hot-switching", not mechanical wear, caused the failure.

Figure 66 are magnified SEM images of the wear spot from the micro-switch that failed at $2.7 \cdot 10^8$ switch cycles. The flowing material indicates thermal cycling occurred and substantiates the micro-arc failure mechanism hypothesis.
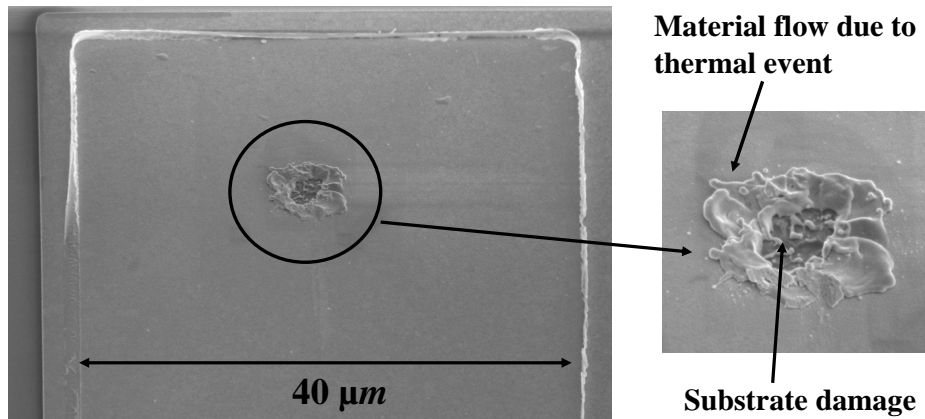

Figure 66   Magnified SEM images of the wear spot for the SNM02 micro-switch with Au-(6.3at%)Pt contacts that failed with $2.7 \cdot 10^8$ switch cycles.

In addition, since the micro-switch was still functioning mechanically (but still failed open with high closed switch resistance) it appears that an organic based surface film was also developing with increasing switch cycles [126] or possibly a highly resistive intermetallic compound or oxide layer formed on the contact's surface due to thermal cycling or material diffusion [146, 147]. This helps explain why the micro-switch failed open after the micro-arc even though the bottom lower contact still appeared useable.

Figures 67 and 68 are SEM images of electric contact pairs from the same SNM02 (design D20) micro-switch with Au-(6.3at%)Pt contact materials that failed due to stiction at $8.8 \cdot 10^8$ switch cycles. The contact pair in Figure 67 shows a catastrophic failure, similar to that shown in Figure 66, while Figure 68 shows mechanical wear due to switch cycling.

Note on Figure 68 that the lower contact "wing," due to sputter lift-off, appears mechanically worn down and a ring of transferred material is shown around

Upper contact **Lower contact**

Material transfer

Material flow due to micro-arc

5 μ*m* 2 μ*m*
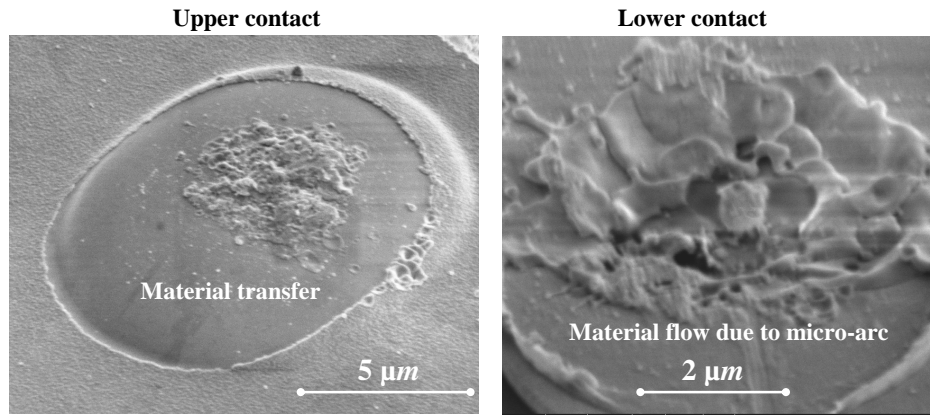
Figure 67   SEM images of an SNM02 (D20 design) micro-switch's upper and lower electric contact pairs (i.e., top). The device failed closed with approximately $8.8 \cdot 10^8$ switch cycles. The catastrophic results of micro-arc damage are highlighted. The contact metals are Au-(6.3at%)Pt.

Upper contact **Lower contact**

Material transfer from lower contact "wing"

Lower contact "wing" mechanically worn

5 μ*m* ~ 10 μ*m*
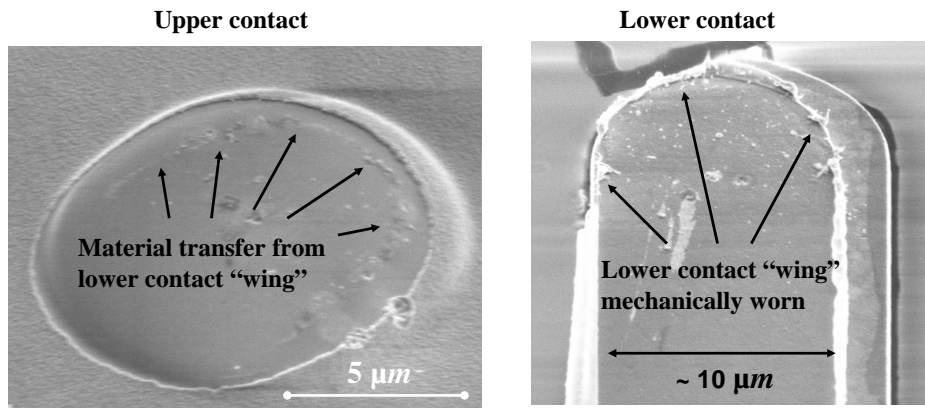
Figure 68   SEM images of an SNM02 (D20 design) micro-switch's upper and lower electric contact pair (i.e., bottom). The device failed closed with approximately $8.8 \cdot 10^8$ switch cycles and mechanical wear due to switch cycling is evident. The contact metals are Au-(6.3at%)Pt.

the perimeter of the upper hemisphere-shaped contact. This indicates that the hemisphere made repeated contact with the "wing" which supports the claim made in section 7.2 about reduced contact resistance performance.

7.6 Summary

In this Chapter micro-switch performance was evaluated by conducting contact resistance, RF (insertion loss and isolation), and lifecycle testing. Contact resistance testing showed that micro-switches with sputtered metal alloy electric contacts result in slightly higher contact resistance values than micro-switches with sputtered Au electric contacts. Lifecycle testing indicates that switching lifetimes, when compared to micro-switches with sputtered Au electric contacts, are increased by a factor of approximately 2-7 times depending on the alloy and the micro-switch's mechanical design. The RF test results corroborated the contact resistance results and observations.

A qualitative electric contact wear assessment was accomplished by comparing thin film material properties, lifecyle test results, and SEM images of worn contacts from failed micro-switches. Although SEM images reveal much about micro-switch operation and electric contact wear, a quantitative surface composition analysis is needed before a complete assessment and thorough evaluation of contact wear can be finalized. This work, however, does indicate that using harder electric contact materials results in longer lived devices. The overall conclusions of this dissertation and some ideas for future research are presented next.

VIII.   Conclusions

8.1   Overall Summary

In this dissertation, the design, fabrication, and testing of RF MEMS contact switches with metal alloy electric contacts was presented. Analytic contact force and contact resistance models were developed and resulted in predictions that agreed with measurements. A binary alloy selection methodology was developed for picking suitable micro-switch electric contact materials. In addition, bi-metallic and ternary alloy electric contacts were briefly investigated. Overall, the results show increased lifetimes at the expense of a small increase in contact resistance for devices with bi-metallic, binary alloy, and ternary alloy contacts. A brief summary of specific results and analysis accomplished is presented next.

    8.1.1   Alloy Selection Methodology.   After reviewing the macro-switch literature, the following hypothesis for incorporating metal alloy micro-switch contacts was developed; use single-phase, miscible binary alloys; avoid intermetallic compounds; avoid materials combinations that tarnish, oxidize, or form robust surface films; and choose an alloy deposition technique compatible with accessible micro-switch fabrication processes. Based on this information, the following alloy selection methodology was developed: 1) utilize equilibrium binary alloy phase diagrams and binary alloy bulk material resistivity data to choose alloy compositions, 2) pick an appropriate thin film deposition method and fabricate test specimens, 3) measure important thin film material properties, and 4) predict contact resistance performance using a suitable model [29]. Using this methodology, micro-switches with Au-(6.3at%)Pt and Au-(3.7at%)Pd electric contact metals were designed, fabricated, and tested [30]. In addition, a brief investigation of micro-switches with bi-metallic (Au-on-Au-(6.3at%)Pt) and ternary alloy (Au-(5at%)Pt-(0.5at%)Cu) electric contacts was accomplished [33].

133

8.1.2 Micro-Switch Modeling and Design. Electrostatic, micro-switch test structures (using the SNM01 mask set) were fabricated and analyzed using analytic equations, a FEM design tool (i.e., Coventorware), and measurements [31, 32, 34]. The results and lessons learned from this analysis were used to design the micro-switch test structures for the SNM02 mask set [30, 166] and helped with developing the SNM02 fabrication process.

After completing the design, fabrication, and some limited testing, the following modeling improvements were investigated: (1) the improved beam model [100], (2) the parallel plate capacitor model that includes a first order fringing fields correction term [113], (3) contact force models [28], and (4) a contact resistance model[33]. Each of the models was validated using measured data. The improved beam and parallel plate capacitor models provided only a small improvement to predictions while the improved contact force and contact resistance models closely matched the micro-switch geometry and resulted in agreement between predicted and measured values.

8.1.3 Device Fabrication. The AFRL/SND baseline fabrication process was a valuable starting point for my this research. From this starting point, process modifications for incorporating sputtered metal alloy electric contacts and hemispherically-shaped upper contacts while using the SNM01 and SNM02 mask sets were developed.

8.1.4 Experiments and Results. Micro-switch performance was evaluated by conducting contact resistance, RF (insertion loss and isolation), and lifecycle testing. Contact resistance and lifecycle testing showed that while micro-switches with sputtered metal alloy electric contacts resulted in slightly higher contact resistance values (than micro-switches with sputtered Au electric contacts) their switching lifetimes were increased by a factor of approximately 2-6 times (than micro-switches with Au electric contacts) depending on the specific alloy and the micro-switch's mechanical design. The RF test results corroborated the contact resistance results

134

and observations. A qualitative electric contact wear assessment was accomplished by comparing thin film material properties, lifecyle test results, and SEM images of worn contacts from failed micro-switches.

The specific contributions of this dissertation to the MEMS field and some opportunities for future research are presented next.

8.2 Contributions

The novel contributions of this work, to the field of MEMS, follow:

1. analytic contact force models for cantilever-style, electrostatic, micro-switches,

2. an analytic micro-switch contact resistance model for devices with sputtered contact metals,

3. a binary metal alloy selection methodology for micro-switch electric contacts,

4. measured thin film metal (i.e Au, Ag, Pd, and Pt) and alloy (i.e., Au-Pd, Au-Pt, and Au-Ag) material properties,

5. co-sputtering fabrication technique for depositing alloy contact metals,

6. an improved hemispherically-shaped upper electric contact geometry,

7. operational RF MEMS metal contact switches with bi-metallic, binary alloy, and ternary alloy electric contacts, and

8. contact resistance, RF measurements, and micro-switch lifecycle test results for the aforementioned micro-switches.

8.3 Ideas for Future Research

The results provided in this dissertation demonstrate that micro-switch lifetime performance is improved when metal alloy electric contact materials are used. This work also serves as a stepping stone for other researchers to build upon. As such, the following ideas for future research are provided.

8.3.1 Electric Contact Materials. The binary alloy compositions studied here were chosen to avoid miscibility gaps, two-phase regions, intermetallic compounds, and be harder that Au. These limitations were put into effect to ensure compatibility with the available micro-switch fabrication process. Shimkat's work with Au-(5%)Ni alloys, however, indicates that a specific two-phase region binary alloys may also be useful for micro-switch electric contacts [135, 136]. In addition, other material combinations, two-phase regions, and intermetallic compounds with unique material properties can be investigated as micro-switch electric contact materials. Additionally, although briefly investigated in this study, bi-metallic and ternary alloy electric contacts still remain largely unexplored as micro-switch electric contact materials.

8.3.2 Fabrication, Modeling, and Design. Although many fabrication process improvements were incorporated into the AFRL/SND baseline process, the process can still be improved. For example, the non-uniform electroplated structural layer needs to be addressed and corrected before a reliable, high yield process is plausible. Further improvements to the sputtered material lift-off process are needed. In this study, the effects of sputter lift-off "wings" were minimized by using oversized lower contacts. An improved sputter lift-off process will allow for more creative mechanical designs like the SNM02 D20 design. Fabrication process improvements will lead to meaningful reliability testing (versus single device lifetime testing) and commercially viable devices [41, 42, 57].

The analytic equations used in this research did not consider contact adhesion or contact friction. Improved models will consider these effects as well as trying to increase contact and restoring forces by using mechanical advantage [40, 60, 71, 74, 98, 101, 114, 159, 152, 161]. RF effects and beam dynamics could also be investigated in future micro-switch modeling efforts [38, 84, 124, 139].

8.3.3 Failure Mechanisms and Wear. The underlying physics of the micro-switch failure mechanisms and wear progression is not well understood [62, 81]. Macro-switch studies have investigated physical wear patterns and contact surface compositional changes [13, 26, 58]. Micro-switch contact surface composition analyses with small spot size are needed to assess metallurgy changes and contaminant film growth that occur during micro-switch lifetime. AES and EDX was attempted, in this study, but substrate charging skewed the data. Specific test structures, that provide a ground for electrons and avoids substrate charging, could be designed and fabricated (along with micro-switches) to allow for more efficient AES analysis.

8.3.4 Testing. Contact resistance, RF insertion loss and isolation, micro-switch force versus deflection/resistance (using a nanoindentor), and lifetime testing was accomplished during this study. Additional testing will reveal more device operating characteristics. For example, switching speed, impact velocity, contact bounce, squeeze film damping tests will shed light onto beam dynamic behavior while hysteresis and contact adhesion tests will uncover additional information about contact metallurgy behavior. In addition, RF test structures for determining parasitic resistance and inductance will result in more efficient RF testing. Additional nanoindentor testing on actual micro-switches will assist in beam, contact force, and contact resistance modeling and design improvements [71, 145].

8.3.5 Systems Approach. The results presented in this study show micro-switch lifetime improvements when using alloy electric contacts. The effects of mechanical micro-switch design and the operating environment (i.e., packaging) were not emphasized in this work. The best results will, most likely, be a result of taking a systems approach to micro-switch design. For example, improved mechanical designs (high restoring and contact force, low insertion loss, and low isolation) [101, 166] with improved contact metallurgies (harder metals with lower adhesion) [29, 30, 33, 136] all packaged (encapsulation and wafer bonding) [19, 138] in a suitable environment

137

are needed before highly reliable and commercially viable RF MEMS metal contacts switches are to be realized. Some groups have taken this approach and show promising results [90, 93]. The ultimate success of RF MEMS metal contact switches, however, will only be demonstrated when reliable RF circuitry and systems are realized [14, 39, 70, 108, 107, 124, 127, 132, 149, 160].

Appendix A.   Modified SNM01 Process Followers

Init.	Process Step	Notes	
	INSPECT WAFER: ❑ Note any defects	**Start Date** **Start Time**	
	SOLVENT CLEAN: ❑ 20 sec acetone rinse at 500 rpm ❑ 20 sec isopropyl rinse at 500 rpm ❑ Dry with nitrogen at 500 rpm ❑ Dry wafer with nitrogen on clean texwipes		
	OXIDE REMOVAL: ❑ 30 sec dip (1:10) BOE:DI Water ❑ 3x DI Water bucket rinse ❑ Dry wafer with nitrogen on clean texwipes		
	DEHYDRATION BAKE: ❑ 1 min 110 ℃ Hot plate bake		
	PMGI COAT : ❑ Flood wafer with SF-11 PMGI ❑ 30 sec spin at 4,000 rpm, ramp=200 ❑ Use edge bead remover (EBR) to remove PMGI on backside (1 min @ 20℃) ❑ 2 min 270 ℃ hot plate bake		
	1813 COAT: ❑ Flood wafer with 1813 ❑ 30 sec spin at 4,000 rpm, ramp=200 ❑ 75 sec 110℃ hot plate bake ❑ Use acetone to remove 1813 on backside		
	EXPOSE 1813 with BOTTOM METAL MASK: ❑ No alignment for first level mask ❑ 3.0 sec exposure, 0 focus on stepper	**SNM01 \DC**	
	1813 DEVELOP: ❑ 30 sec develop with 351:DI Water (1:5) at 500 rpm ❑ 30 sec DI Water rinse at 500 rpm ❑ Dry with nitrogen at 500 rpm ❑ Dry wafer with nitrogen on clean texwipes		
	INSPECT RESIST: ❑ Inspect photoresist under microscope (use yellow filter)		
	DEEP UV EXPOSE: ❑ 600 sec Deep UV exposure @ 35 mW/cm2, 254 nm		
	PMGI DEVELOP ❑ 30 sec SAL 101 spin develop at 500 rpm ❑ 30 sec DI rinse at 500 rpm ❑ Dry wafer with nitrogen on clean texwipes		
	INSPECT RESIST: ❑ Inspect photoresist under microscope		
	ASHER: ❑ 4 min, 200 W, 400 sccm O_2, LFE Barrel Asher		
	PRE-METAL DIP: ❑ 30 sec Dip (1:10) BOE:DI Water ❑ 3x DI Water bucket rinse ❑ Dry wafer with nitrogen on clean texwipes		
	BOTTOM METAL DEPOSITION: ❑ Evaporate 500 Å Cr / 4000 Å Au ❑ Sputter 50 Å Metal/Alloy		
	MEASURE STEP HEIGHT: ❑ Measure step height of sputtered metal/alloy (Si Mech Piece) Mid: _____Top (flat):_____Bot:_____ Lt:_____ Rt:_____		

Figure 69   Modified SNM01 bottom metal process follower (page 1/2).

	LIFT-OFF BOTTOM METAL: ❏ Heat 1165 remover to 90 ℃ ❏ Use tape to remove excess metal with wafer on vacuum chuck (Tape lift-off) ❏ Visually inspect for metal removal ❏ 20 sec spray with acetone gun at 1000 rpm (pressurized @ 40 psi) ❏ 20 sec spray with acetone bottle at 500 rpm ❏ 30 sec spray with isopropyl alcohol at 500 rpm ❏ Dry with nitrogen at 500 rpm ❏ Dry wafer with nitrogen on clean texwipes ❏ Visually inspect for metal removal ❏ Ultrasonic cleaner for 5-15 minutes (acetone) ❏ 20 sec spray with acetone gun at 1000 rpm (pressurized @ 40 psi) ❏ 20 sec spray with acetone bottle at 500 rpm ❏ 30 sec spray with isopropyl alcohol at 500 rpm ❏ Dry with nitrogen at 500 rpm ❏ Dry wafer with nitrogen on clean texwipes ❏ Visually inspect for metal removal		
	1165 STRIP PMGI: ❏ 2 min 90 ℃ 1165 remover ❏ 3x DI water bucket rinse ❏ Dry wafer with nitrogen on clean texwipes		
	INSPECT WAFER: ❏ Inspect for resist removal		
	LIFT-OFF BOTTOM METAL (Cont.): ❏ Ultrasonic cleaner for 5-10 minutes (acetone) ❏ 20 sec spray with acetone gun at 1000 rpm (pressurized @ 40 psi) ❏ 20 sec spray with acetone bottle at 500 rpm ❏ 30 sec spray with isopropyl alcohol at 500 rpm ❏ Dry with nitrogen at 500 rpm ❏ Dry wafer with nitrogen on clean texwipes ❏ Visually inspect for metal removal		
	MEASURE STEP HEIGHT: ❏ Measure step height of DC metal Mid: _____Top (flat):_____Bot:_____ Lt:_____ Rt:_____		
	INSPECT WAFER: ❏ Inspect wafer for stringers	**Stop Date** **Start Time**	

Figure 70   Modified SNM01 bottom metal process follower (page 2/2).

Init.	Process Step	Notes	
	DEHYDRATION BAKE: ❏ 1 min 110℃ Hot plate bake	**Start Date**	
	PMGI COAT #1: ❏ Flood wafer with SF-11 PMGI ❏ 30 sec spin at 4,000 rpm, ramp=200 ❏ Use edge bead remover (EBR) to remove PMGI on backside (1 min @ 20℃) ❏ 2 min 270 ℃ hot plate bake	**Start Time**	
	PMGI COAT #2: ❏ Flood wafer with SF-11 PMGI ❏ 30 sec spin at 4,000 rpm, ramp=200 ❏ Use edge bead remover (EBR) to remove PMGI on backside (1 min @ 20℃) ❏ 2 min 270 ℃ hot plate bake		
	PMGI COAT #3: ❏ Flood wafer with SF-11 PMGI ❏ 30 sec spin at 4,000 rpm, ramp=200 ❏ Use edge bead remover (EBR) to remove PMGI on backside (1 min @ 20℃) ❏ 2 min 270 ℃ hot plate bake		
	1813 COAT: ❏ Flood wafer with 1813 ❏ 30 sec spin at 4000 rpm, ramp=200 ❏ 75 sec 110 ℃ hot plate bake ❏ Use acetone to remove 1813 on backside		
	EXPOSE 1813 with POST MASK: ❏ Align to Bottom Metal alignment mark ❏ 3.0 sec Exposure, 0 Focus on **Stepper**	**SNM01 \PST**	
	1813 DEVELOP: ❏ 30 sec develop with 351:DI (1:5) at 500 rpm ❏ 30 sec DI rinse at 500 rpm ❏ Dry with nitrogen at 500 rpm ❏ Dry wafer with nitrogen on clean texwipes		
	INSPECT LITHOGRAPHY: ❏ Place wafer flat towards top of microscope ❏ Inspect wafer alignment with yellow filter on microscope ❏ Check Lithography : ❏ Open ❏ Clean ❏ Sharp Definition ❏ Measure vernier alignment on edge reticles in center row (Left) Theta (Right) X Alignment (Right) Y Alignment ❏ Rework wafer if alignment is off more than 0.6 µm	Y_{Left} = X_{Right} = Y_{Right} = $\theta = Y_{Right} - Y_{Left}$ =	
	1ST DUV CYCLE (~1.2µm / cycle) ❏ 200 sec Deep UV exposure @ 35 mW/cm^2, 254 nm		
	PMGI DEVELOP: ❏ 30 sec SAL 101 spin develop at 500 rpm ❏ 30 sec DI water rinse at 500 rpm ❏ Dry wafer with nitrogen on clean texwipes		
	INSPECT RESIST: ❏ Inspect photresist		
	2ND DUV CYCLE: ❏ 200 sec Deep UV exposure @ 35 mW/cm^2, 254 nm		
	PMGI DEVELOP: ❏ 30 sec SAL 101 spin develop at 500 rpm ❏ 30 sec DI water rinse at 500 rpm ❏ Dry wafer with nitrogen on clean texwipes		
	INSPECT RESIST: ❏ Inspect photresist		
	3D DUV CYCLE: ❏ 30 sec Deep UV exposure @ 35 mW/cm^2, 254 nm		

Figure 71   Modified SNM01 post and dimple process follower (page 1/3).

Process		
PMGI DEVELOP: ❏ 30 sec SAL 101 spin develop at 500 rpm ❏ 30 sec DI water rinse at 500 rpm ❏ Dry wafer with nitrogen on clean texwipes		
INSPECT RESIST: ❏ Inspect photresist		
STRIP 1813: ❏ 20 sec acetone gun at 1000 rpm ❏ 20 sec acetone rinse at 500 rpm ❏ 20 sec Isopropanol rinse at 500 rpm ❏ 10 sec DI rinse at 500 rpm ❏ Dry with nitrogen at 500 rpm ❏ Dry wafer with Nitrogen on clean texwipes		
INSPECT RESIST: ❏ Inspect photoresist for 1813 removal		
MEASURE STEP HEIGHT: ❏ Measure step height of sputtered metal (Si Mech Piece) Mid: _____Top (flat):_____Bot:_____ Lt:_____ Rt:_____		
ASHER: ❏ 4 min, 200 W, 400 sccm O_2, LFE		
MEASURE STEP HEIGHT: ❏ Measure step height of sputtered metal (Si Mech Piece) Mid: _____Top (flat):_____Bot:_____ Lt:_____ Rt:_____		
DEHYDRATION BAKE (If needed): ❏ 1 min 110℃ Hot plate bake		
1813 COAT: ❏ Flood wafer with 1813 ❏ 30 sec spin at 4000 rpm, ramp=200 ❏ Use acetone to remove 1813 on backside ❏ 75 sec 110 ℃ hot plate bake		
EXPOSE 1813 with DIMPLE MASK: ❏ Align to Bottom Metal alignment mark ❏ 3.0 sec Exposure, 0 Focus on **Stepper**	**SNM01\DMP**	
1813 DEVELOP: ❏ 30 sec develop with 351:DI (1:5) at 500 rpm ❏ 30 sec DI rinse at 500 rpm ❏ Dry with nitrogen at 500 rpm ❏ Dry wafer with nitrogen on clean texwipes		
INSPECT LITHOGRAPHY: ❏ Place wafer flat towards top of microscope ❏ Inspect wafer alignment with yellow filter on microscope ❏ Check Lithography : ❏ Open ❏ Clean ❏ Sharp Definition		
MEASURE STEP HEIGHT: ❏ Measure step height of sputtered metal (Si Mech Piece) Mid: _____Top (flat):_____Bot:_____ Lt:_____ Rt:_____		
1ST PARTIAL DUV EXPOSE ❏ 150 sec Deep UV exposure @ 35 mW/cm^2, 254 nm		
1ST PMGI DEVELOP: ❏ 100 sec SAL 101 immersion develop with agitation ❏ Replace SAL 101 after 2 develop cycles ❏ 3x DI bucket rinse ❏ Dry wafer with nitrogen on clean texwipes		
MEASURE STEP HEIGHT: ❏ Measure resist step height in three locations Top _____ Middle _____ Bottom _____		

Figure 72   Modified SNM01 post and dimple process follower (page 2/3).

	2ND PARTIAL DUV EXPOSE (If needed) ❑ 50 sec Deep UV exposure @ 35 mW/cm^2, 254 nm		
	2ND PMGI DEVELOP: ❑ 100 sec SAL 101 immersion develop with agitation ❑ Replace SAL 101 after 2 develop cycles ❑ 3x DI bucket rinse ❑ Dry wafer with nitrogen on clean texwipes		
	MEASURE STEP HEIGHT: ❑ Measure resist step height in three locations Top _____ Middle _____ Bottom _____		
	STRIP 1813: ❑ 15 sec acetone gun at 1000 rpm ❑ 15 sec acetone bottle at 500 rpm ❑ 20 sec Isopropanol rinse at 500 rpm ❑ 10 sec DI rinse at 500 rpm ❑ Dry with nitrogen at 500 rpm ❑ Dry wafer with Nitrogen on clean texwipes		
	INSPECT RESIST: ❑ Inspect photoresist for 1813 removal		
	MEASURE STEP HEIGHT: ❑ Measure resist step height in three locations Top _____ Middle _____ Bottom _____		
	ASHER: ❑ 4 min, 200 W, 400 sccm O$_2$, LFE		
	MEASURE STEP HEIGHT: ❑ Measure PMGI step height in three locations Top _____ Middle _____ Bottom _____		
	POST REFLOW & INSPECT WAFER: ❑ 3-4 MIN at 250 ℃ oven bake **USE NITROGEN OVEN AND METAL TRAY** Center the oven tray, Start timer after door is closed ❑ Inspect for resist reflow. Reflow again if necessary	**Reflow Time:**	
	MEASURE STEP HEIGHT: ❑ Measure resist step height in three locations Top _____ Middle _____ Bottom _____		
	HARD BAKE: ❑ Place in 90 ℃ hot air oven 60 min before seed la yer deposition ❑ Skip this step if reflow just completed or if seed layer depositon follows.	**Stop Date** **Stop Time**	

Figure 73   Modified SNM01 post and dimple process follower (page 3/3).

Init.	Process Step	Notes	
	ASHER: ❏ 4 min, 200 W, 400 sccm O_2, LFE	**Start Date**	
	PRE-METAL DIP: ❏ 30 sec BOE : DI water (1:10) ❏ 3x bucket DI water rinse ❏ Dry wafer on clean texwipes with Nitrogen	**Start Time**	
	SEED LAYER DEPOSIT ❏ Alloy/ Au / Ti 300Å / 400Å / 200Å		
	DEHYDRATION BAKE: ❏ 1 min 110℃ hot plate bake		
	9260 COAT ❏ Flood wafer with 9260 resist. Cut-off pipette at first indentation ❏ 30 sec spin @ 5000 rpm, Ramp=200 ❏ 2 min 110℃ hot plate bake ❏ Use acetone swab to remove 9260 on backside		
	EXPOSE 9260 TO BRIDGE MASK: ❏ Align to Bottom Metal alignment mark ❏ 15.0 sec Exposure, 0 Focus on stepper	**SNM01_RF_**	
	9260 DEVELOP: ❏ 3.0 min (210 sec) bucket develop in **fresh** AZ400k:DI (1:4) with <u>Hand Agitation</u> ❏ 3x bucket rinse ❏ Dry wafer with nitrogen on Texwipes		

	INSPECT LITHOGRAPHY:
	❏ Place wafer flat towards top of microscope
	❏ Inspect wafer alignment with yellow filter on microscope
	   ❏ Check Lithography : ❏ Open ❏ Clean ❏ Sharp Definition
	❏ Measure vernier alignment on edge reticles in center row
	                (Left) Theta
	                (Right) X Alignment
	                (Right) Y Alignment
	❏ Rework wafer if alignment is off more than 0.6 μm
		Y_{Left} =
		X_{Right} =
		Y_{Right} =
		θ = Y_{Right} - Y_{Left} =	

	CLEAR PLATING CLIP AREA: ❏ Remove four small areas with acetone dampened swab for plating clips		
	1400-27 COAT BACKSIDE: ❏ Coat wafer backside with 1400-27 using large swab. ❏ Dry photoresist with Nitrogen to help coat edges		
	BACKSIDE RESIST BAKE: ❏ 1 min 90℃ Oven Bake (Wafer upside down in Fluo roware container)		
	ASHER: ❏ 4 min, 200 W, 400 sccm O_2, LFE		
	TITANIUM ETCH: ❏ 90 sec 1:10 BOE:DI (until clear) ❏ 10 sec DI bucket rinse ❏ 10 sec 1:10 BOE:DI ❏ 4X DI bucket rinse ❏ Dry with nitrogen on clean texwipes		
	INSPECT WAFER: ❏ Make sure Ti layer is completely removed.		
	MEASURE RESIST STEP HEIGHT: ❏ Measure step height and record in table		
	ELECTROPLATE STRUCTURAL LAYER: ❏ Power on the plating bath and wait for temp to rise ❏ Power on the Dynacomm controller and start the software ❏ Set current density (mA/cm^2), average current (mA), and Amin in software ❏ Load wafer and immerse into the plating bath solution ❏ _____ min plate time at at _____mA to give about ___ **μm** total thickness ❏ 2X DI bucket rinse ❏ Dry wafer with nitrogen on clean Texwipes ❏ Turn off plating system (if finished plating)		
	MEASURE STEP HEIGHT: ❏ Measure step height and record in table		

Figure 74   Modified SNM01 structural layer process follower (page 1/2).

REMOVE 9260 ❑ Remove 1400-27 from wafer backside with acetone soaked swap. Wipe thoroughly so all resist is removed. ❑ 30 sec spray with acetone bottle at 500 rpm ❑ 30 sec isopropyl alcohol at 500 rpm ❑ 10 sec DI bottle ❑ Dry with nitrogen at 500 rpm ❑ Dry wafer with nitrogen on clean Texwipes	
INSPECT WAFER: ❑ Make sure resist is completely removed.	
MEASURE STEP HEIGHT: ❑ Measure metal height and record in table ❑ Record result in plating log book	
TITANIUM LAYER ETCH: ❑ 45–90 sec 1:10 BOE:DI (Etch until clear + 5-10 sec longer) ❑ 10 sec DI bucket rinse ❑ 10 sec 1:10 BOE:DI ❑ 3X DI bucket rinse ❑ Dry with nitrogen on clean Texwipes	
INSPECT WAFER: ❑ Make sure Ti layer is completely removed.	
SEED LAYER ETCH: ❑ Immerse in Technistrip (Etch until clear + 30 sec longer) ❑ 3x DI bucket rinse ❑ Dry with nitrogen on clean Texwipes	
INSPECT WAFER: ❑ Make sure seed layer is completely removed.	
MEASURE STEP HEIGHT: ❑ Measure metal height and record in table	
ALLOY LAYER ETCH: ❑ Immerse in Aqua Regus (HCL:HNO3) (30 sec) ❑ 3x DI bucket rinse ❑ Dry with nitrogen on clean Texwipes	
INSPECT WAFER: ❑ Make sure alloy layer is completely removed.	
MEASURE STEP HEIGHT: ❑ Measure metal height and record in table	**Finish Date** **Finish Time**

ETCH TABLE	Center	Top	Bottom	Left	Right
PR Ht Before Plating					
PR Ht After Plating					
Au Ht After PR strip					
Au Ht After Seed Etch					
Au Ht After Alloy Etch					

Figure 75   Modified SNM01 structural layer process follower (page 2/2).

Init.	Process Step	Notes
	REMOVE PMGI (Release): ❑ Place sample in room temp 1165, cover beaker with foil, place on hot plate. Set hot plate to 125°C (150 ml of 1165, 1000 ml beaker. 30 minute 1165 strip. ❑ Wet transfer from 1165 beaker to 1st IPA in Petri dish, 30 s soak ❑ Wet transfer to 2nd IPA in Petri dish, 30 s soak ❑ Wet transfer to 3rd IPA in Petri dish, 30 s soak ❑ Wet transfer to 4th IPA in Petri dish, 30 s soak ❑ Wet transfer to 1st methanol in Petri dish, 30 s soak ❑ Wet transfer to 2nd methanol in Petri dish, 30 s soak ❑ Wet transfer to 3rd methanol in Petri dish, 30 s soak ❑ Wet transfer to 4th methanol in Petri dish, 30 s soak ❑ Remove wafer from 4th methanol dish and place in CO2 dryer. Fill chamber with methanol to cover the wafer. Immediately cover CO2 dryer and start process.	**Start Date** **Start Time**
	❑ CO2 critical point dryer.	
	INSPECT WAFER:	
	ASHER: ❑ 4 min, 200W, 500 sccm, O_2, LFE	**Finish Date** **Finish Time**

Figure 76   Modified SNM01 release process follower (page 1/1).

Init.	Process Step	Notes	
	INSPECT WAFER: ❏ Note any defects	**Start Date**	
	SOLVENT CLEAN: ❏ 20 sec acetone rinse at 500 rpm ❏ 20 sec isopropyl rinse at 500 rpm ❏ Dry with nitrogen at 500 rpm ❏ Dry wafer with nitrogen on clean texwipes	**Start Time**	
	OXIDE REMOVAL: ❏ 30 sec dip (1:10) BOE:DI Water ❏ 3x DI Water bucket rinse ❏ Dry wafer with nitrogen on clean texwipes		
	DEHYDRATION BAKE: ❏ 1 min 110 ℃ Hot plate bake		
	PMGI COAT : ❏ Flood wafer with SF-11 PMGI ❏ 30 sec spin at 4,000 rpm, ramp=200 ❏ Use edge bead remover (EBR) to remove PMGI on backside (1 min @ 20℃) ❏ 2 min 270 ℃ hot plate bake		
	1813 COAT: ❏ Flood wafer with 1813 ❏ 30 sec spin at 4,000 rpm, ramp=200 ❏ 75 sec 110℃ hot plate bake ❏ Use acetone to remove 1813 on backside		
	EXPOSE 1813 with BOTTOM METAL MASK: ❏ No alignment for first level mask ❏ 3.0 sec exposure, 0 focus on stepper		
	1813 DEVELOP: ❏ 30 sec develop with 351:DI Water (1:5) at 500 rpm ❏ 30 sec DI Water rinse at 500 rpm ❏ Dry with nitrogen at 500 rpm ❏ Dry wafer with nitrogen on clean texwipes	**SNM02 \DC**	
	INSPECT RESIST: ❏ Inspect photoresist under microscope (use yellow filter)		
	1ST DEEP UV EXPOSE: ❏ 200 sec Deep UV exposure @ 35 mW/cm2, 254 nm		
	1ST PMGI DEVELOP ❏ 30 sec SAL 101 spin develop at 500 rpm ❏ 30 sec DI rinse at 500 rpm ❏ Dry wafer with nitrogen on clean texwipes		
	2ND DEEP UV EXPOSE: ❏ 200 sec Deep UV exposure @ 35 mW/cm2, 254 nm		
	2ND PMGI DEVELOP ❏ 30 sec SAL 101 spin develop at 500 rpm ❏ 30 sec DI rinse at 500 rpm ❏ Dry wafer with nitrogen on clean texwipes		
	DEEP UV EXPOSE: ❏ 600 sec Deep UV exposure @ 35 mW/cm2, 254 nm		
	PMGI DEVELOP ❏ 30 sec SAL 101 spin develop at 500 rpm ❏ 30 sec DI rinse at 500 rpm ❏ Dry wafer with nitrogen on clean texwipes		
	INSPECT RESIST: ❏ Inspect photoresist under microscope		
	ASHER: ❏ 4 min, 200 W, 400 sccm O_2, LFE Barrel Asher		
	PRE-METAL DIP: ❏ 30 sec Dip (1:10) BOE:DI Water ❏ 3x DI Water bucket rinse ❏ Dry wafer with nitrogen on clean texwipes		
	BOTTOM METAL DEPOSITION: ❏ Evaporate 500 Å Cr / 4000 Å Au		

Figure 77   SNM02 bottom metal process follower (page 1/2).

	BOTTOM METAL LIFT-OFF: ❏ Heat 1165 remover to 90 ℃ ❏ Use tape to remove excess metal with wafer on vacuum chuck (Tape lift-off) ❏ Visually inspect for metal removal ❏ 20 sec spray with acetone gun at 1000 rpm (pressurized @ 40 psi) ❏ 20 sec spray with acetone bottle at 500 rpm ❏ 30 sec spray with isopropyl alcohol at 500 rpm ❏ Dry with nitrogen at 500 rpm ❏ Dry wafer with nitrogen on clean texwipes ❏ Visually inspect for metal removal		
	1165 STRIP PMGI: ❏ 2 min 90 ℃ 1165 remover ❏ 3x DI water bucket rinse ❏ Dry wafer with nitrogen on clean texwipes	**Stop Date** **Start Time**	
	INSPECT WAFER: ❏ Inspect for resist removal		

Figure 78   SNM02 bottom metal process follower (page 2/2).

Init.	Process Step	Notes	
	DEHYDRATION BAKE: ❑ 1 min 110 ℃ Hot plate bake	**Start Date**	
	PMGI COAT : ❑ Flood wafer with SF-11 PMGI ❑ 30 sec spin at 4,000 rpm, ramp=200 ❑ Use edge bead remover (EBR) to remove PMGI on backside (1 min @ 20℃) ❑ 2 min 270 ℃ hot plate bake	**Start Time**	
	1813 COAT: ❑ Flood wafer with 1813 ❑ 30 sec spin at 4,000 rpm, ramp=200 ❑ 75 sec 110℃ hot plate bake ❑ Use acetone to remove 1813 on backside		
	EXPOSE 1813 with CONTACT METAL MASK: ❑ No alignment for first level mask ❑ 3.0 sec exposure, 0 focus on stepper	**SNM02 \RF**	
	1813 DEVELOP: ❑ 30 sec develop with 351:DI Water (1:5) at 500 rpm ❑ 30 sec DI Water rinse at 500 rpm ❑ Dry with nitrogen at 500 rpm ❑ Dry wafer with nitrogen on clean texwipes		
	INSPECT LITHOGRAPHY: ❑ Place wafer flat towards top of microscope ❑ Inspect wafer alignment with yellow filter on microscope ❑ Check Lithography : ❑ Open ❑ Clean ❑ Sharp Definition ❑ Measure vernier alignment on edge reticles in center row (Left) Theta (Right) X Alignment (Right) Y Alignment ❑ Rework wafer if alignment is off more than 0.6 µm	Y_{Left} = X_{Right} = Y_{Right} = $\theta = Y_{Right}$ - Y_{Left} =	
	1ST DEEP UV EXPOSE: ❑ 200 sec Deep UV exposure @ 35 mW/cm2, 254 nm		
	1ST PMGI DEVELOP ❑ 30 sec SAL 101 spin develop at 500 rpm ❑ 30 sec DI rinse at 500 rpm ❑ Dry wafer with nitrogen on clean texwipes		
	2ND DEEP UV EXPOSE: ❑ 200 sec Deep UV exposure @ 35 mW/cm2, 254 nm		
	2ND PMGI DEVELOP ❑ 30 sec SAL 101 spin develop at 500 rpm ❑ 30 sec DI rinse at 500 rpm ❑ Dry wafer with nitrogen on clean texwipes		
	INSPECT RESIST: ❑ Inspect photoresist under microscope		
	ASHER: ❑ 4 min, 200 W, 400 sccm O$_2$, LFE Barrel Asher		
	PRE-METAL DIP: ❑ 30 sec Dip (1:10) BOE:DI Water ❑ 3x DI Water bucket rinse ❑ Dry wafer with nitrogen on clean texwipes		
	CONTACT METAL DEPOSITION: ❑ Sputter ____ Å of ____		

Figure 79   SNM02 contact metal process follower (page 1/2).

	CONTACT METAL LIFT-OFF: ❑ Heat 1165 remover to 90 ℃ ❑ Use tape to remove excess metal with wafer on vacuum chuck (Tape lift-off) ❑ Visually inspect for metal removal ❑ 20 sec spray with acetone gun at 1000 rpm (pressurized @ 40 psi) ❑ 20 sec spray with acetone bottle at 500 rpm ❑ 30 sec spray with isopropyl alcohol at 500 rpm ❑ Dry with nitrogen at 500 rpm ❑ Dry wafer with nitrogen on clean texwipes ❑ Visually inspect for metal removal ❑ Ultrasonic cleaner for 5-15 minutes (acetone) ❑ 20 sec spray with acetone gun at 1000 rpm (pressurized @ 40 psi) ❑ 20 sec spray with acetone bottle at 500 rpm ❑ 30 sec spray with isopropyl alcohol at 500 rpm ❑ Dry with nitrogen at 500 rpm ❑ Dry wafer with nitrogen on clean texwipes ❑ Visually inspect for metal removal		
	1165 STRIP PMGI: ❑ 2 min 90 ℃ 1165 remover ❑ 3x DI water bucket rinse ❑ Dry wafer with nitrogen on clean texwipes		
	INSPECT WAFER: ❑ Inspect for resist removal		
	CONTACT METAL LIFT-OFF (Cont.): ❑ Ultrasonic cleaner for 5-10 minutes (acetone) ❑ 20 sec spray with acetone gun at 1000 rpm (pressurized @ 40 psi) ❑ 20 sec spray with acetone bottle at 500 rpm ❑ 30 sec spray with isopropyl alcohol at 500 rpm ❑ Dry with nitrogen at 500 rpm ❑ Dry wafer with nitrogen on clean texwipes ❑ Visually inspect for metal removal		
	MEASURE STEP HEIGHT: ❑ Measure step height of contact metal Mid: _____Top (flat):_____Bot:_____ Lt:_____ Rt:_____	**Stop Date** **Start Time**	
	INSPECT WAFER: ❑ Inspect for stringers		

Figure 80   SNM02 contact metal process follower (page 2/2).

Init.	Process Step	Notes	
	DEHYDRATION BAKE: ❏ 1 min 110℃ Hot plate bake	**Start Date**	
	PMGI COAT #1: ❏ Flood wafer with SF-11 PMGI ❏ 30 sec spin at 4,000 rpm, ramp=200 ❏ Use edge bead remover (EBR) to remove PMGI on backside (1 min @ 20℃) ❏ 2 min 270 ℃ hot plate bake	**Start Time**	
	PMGI COAT #2: ❏ Flood wafer with SF-11 PMGI ❏ 30 sec spin at 4,000 rpm, ramp=200 ❏ Use edge bead remover (EBR) to remove PMGI on backside (1 min @ 20℃) ❏ 2 min 270 ℃ hot plate bake		
	PMGI COAT #3: ❏ Flood wafer with SF-11 PMGI ❏ 30 sec spin at 4,000 rpm, ramp=200 ❏ Use edge bead remover (EBR) to remove PMGI on backside (1 min @ 20℃) ❏ 2 min 270 ℃ hot plate bake		
	1813 COAT: ❏ Flood wafer with 1813 ❏ 30 sec spin at 4000 rpm, ramp=200 ❏ 75 sec 110 ℃ hot plate bake ❏ Use acetone to remove 1813 on backside		
	EXPOSE 1813 with POST MASK: ❏ Align to Bottom Metal alignment mark ❏ 3.0 sec Exposure, 0 Focus on **Stepper**	**SNM02 \PO**	
	1813 DEVELOP: ❏ 30 sec develop with 351:DI (1:5) at 500 rpm ❏ 30 sec DI rinse at 500 rpm ❏ Dry with nitrogen at 500 rpm ❏ Dry wafer with nitrogen on clean texwipes		

	INSPECT LITHOGRAPHY:
	❏ Place wafer flat towards top of microscope
	❏ Inspect wafer alignment with yellow filter on microscope
	  ❏ Check Lithography : ❏ Open ❏ Clean ❏ Sharp Definition
	❏ Measure vernier alignment on edge reticles in center row
	              (Left) Theta
	          (Right) X Alignment
	          (Right) Y Alignment
	❏ Rework wafer if alignment is off more than 0.6 μm
		Y_{Left} =
		X_{Right} =
		Y_{Right} =
		$\theta = Y_{Right} - Y_{Left}$ =	

	1ST DUV CYCLE (~1.2μm / cycle) ❏ 200 sec Deep UV exposure @ 35 mW/cm^2, 254 nm		
	PMGI DEVELOP: ❏ 30 sec SAL 101 spin develop at 500 rpm ❏ 30 sec DI water rinse at 500 rpm ❏ Dry wafer with nitrogen on clean texwipes		
	INSPECT RESIST: ❏ Inspect photresist		
	2ND DUV CYCLE: ❏ 200 sec Deep UV exposure @ 35 mW/cm^2, 254 nm		
	PMGI DEVELOP: ❏ 30 sec SAL 101 spin develop at 500 rpm ❏ 30 sec DI water rinse at 500 rpm ❏ Dry wafer with nitrogen on clean texwipes		
	INSPECT RESIST: ❏ Inspect photresist		
	3D DUV CYCLE: ❏ 30 sec Deep UV exposure @ 35 mW/cm^2, 254 nm		
	PMGI DEVELOP: ❏ 30 sec SAL 101 spin develop at 500 rpm ❏ 30 sec DI water rinse at 500 rpm ❏ Dry wafer with nitrogen on clean texwipes		

Figure 81   SNM02 post and dimple process follower (page 1/3).

Init.	Process Step	Notes	
	DEHYDRATION BAKE: ❏ 1 min 110℃ Hot plate bake	**Start Date**	
	PMGI COAT #1: ❏ Flood wafer with SF-11 PMGI ❏ 30 sec spin at 4,000 rpm, ramp=200 ❏ Use edge bead remover (EBR) to remove PMGI on backside (1 min @ 20℃) ❏ 2 min 270 ℃ hot plate bake	**Start Time**	
	PMGI COAT #2: ❏ Flood wafer with SF-11 PMGI ❏ 30 sec spin at 4,000 rpm, ramp=200 ❏ Use edge bead remover (EBR) to remove PMGI on backside (1 min @ 20℃) ❏ 2 min 270 ℃ hot plate bake		
	PMGI COAT #3: ❏ Flood wafer with SF-11 PMGI ❏ 30 sec spin at 4,000 rpm, ramp=200 ❏ Use edge bead remover (EBR) to remove PMGI on backside (1 min @ 20℃) ❏ 2 min 270 ℃ hot plate bake		
	1813 COAT: ❏ Flood wafer with 1813 ❏ 30 sec spin at 4000 rpm, ramp=200 ❏ 75 sec 110 ℃ hot plate bake ❏ Use acetone to remove 1813 on backside		
	EXPOSE 1813 with POST MASK: ❏ Align to Bottom Metal alignment mark ❏ 3.0 sec Exposure, 0 Focus on **Stepper**	**SNM02 \PO**	
	1813 DEVELOP: ❏ 30 sec develop with 351:DI (1:5) at 500 rpm ❏ 30 sec DI rinse at 500 rpm ❏ Dry with nitrogen at 500 rpm ❏ Dry wafer with nitrogen on clean texwipes		

	INSPECT LITHOGRAPHY:
	❏ Place wafer flat towards top of microscope
	❏ Inspect wafer alignment with yellow filter on microscope
	  ❏ Check Lithography : ❏ Open ❏ Clean ❏ Sharp Definition
	❏ Measure vernier alignment on edge reticles in center row
	   (Left) Theta
	   (Right) X Alignment
	   (Right) Y Alignment
	❏ Rework wafer if alignment is off more than 0.6 µm
		Y_{Left} =
		X_{Right} =
		Y_{Right} =
		$\theta = Y_{Right} - Y_{Left}$ =	

	1ST DUV CYCLE (~1.2µm / cycle) ❏ 200 sec Deep UV exposure @ 35 mW/cm^2, 254 nm		
	PMGI DEVELOP: ❏ 30 sec SAL 101 spin develop at 500 rpm ❏ 30 sec DI water rinse at 500 rpm ❏ Dry wafer with nitrogen on clean texwipes		
	INSPECT RESIST: ❏ Inspect photresist		
	2ND DUV CYCLE: ❏ 200 sec Deep UV exposure @ 35 mW/cm^2, 254 nm		
	PMGI DEVELOP: ❏ 30 sec SAL 101 spin develop at 500 rpm ❏ 30 sec DI water rinse at 500 rpm ❏ Dry wafer with nitrogen on clean texwipes		
	INSPECT RESIST: ❏ Inspect photresist		
	3D DUV CYCLE: ❏ 30 sec Deep UV exposure @ 35 mW/cm^2, 254 nm		
	PMGI DEVELOP: ❏ 30 sec SAL 101 spin develop at 500 rpm ❏ 30 sec DI water rinse at 500 rpm		

Figure 82   SNM02 post and dimple process follower (page 2/3).

	2ND PMGI DEVELOP: ❏ 100 sec SAL 101 immersion develop with agitation ❏ Replace SAL 101 after 2 develop cycles ❏ 3x DI bucket rinse ❏ Dry wafer with nitrogen on clean texwipes			
	MEASURE STEP HEIGHT: ❏ Measure resist step height in three locations Top _____ Middle _____ Bottom _____			
	STRIP 1813: ❏ 15 sec acetone gun at 1000 rpm ❏ 15 sec acetone bottle at 500 rpm ❏ 20 sec Isopropanol rinse at 500 rpm ❏ 10 sec DI rinse at 500 rpm ❏ Dry with nitrogen at 500 rpm ❏ Dry wafer with Nitrogen on clean texwipes			
	INSPECT RESIST: ❏ Inspect photoresist for 1813 removal			
	MEASURE STEP HEIGHT: ❏ Measure resist step height in three locations Top _____ Middle _____ Bottom _____			
	ASHER: ❏ 4 min, 200 W, 400 sccm O_2, LFE			
	MEASURE STEP HEIGHT: ❏ Measure PMGI step height in three locations Top _____ Middle _____ Bottom _____			
	POST REFLOW & INSPECT WAFER: ❏ 3-4 MIN at 250 ℃ oven bake **USE NITROGEN OVEN AND METAL TRAY** Center the oven tray, Start timer after door is closed ❏ Inspect for resist reflow. Reflow again if necessary	**Reflow Time:**		
	MEASURE STEP HEIGHT: ❏ Measure resist step height in three locations Top _____ Middle _____ Bottom _____			

	HARD BAKE:
	   ❏ Place in 90 ℃ hot air oven 60 min before seed la yer deposition
	   ❏ Skip this step if reflow just completed or if seed layer depositon follows.
		Stop Date
		
		Stop Time		

Figure 83   SNM02 post and dimple process follower (page 3/3).

Init.	Process Step	Notes	Date Time
	HARD BAKE: ❑ Place in 90 ℃ hot air oven 60 min before seed la yer deposition ❑ Skip this step if reflow just completed or if seed layer depositon follows.	**Start Date**	
	CONTACT METAL DEPOSITION: ❑ Sputter ____ Å of ____	**Start Time**	
	1813 COAT: ❑ Flood wafer with 1813 ❑ 30 sec spin at 4000 rpm, ramp=200 ❑ Use acetone to remove 1813 on backside ❑ 75 sec 110 ℃ hot plate bake		
	EXPOSE 1813 with REVERSE DIMPLE MASK: ❑ Align to Bottom Metal alignment mark ❑ 3.0 sec Exposure, 15 Focus on **Stepper**	**SNM02 \RDMP**	
	1813 DEVELOP: ❑ 30 sec develop with 351:DI (1:5) at 500 rpm ❑ 30 sec DI rinse at 500 rpm ❑ Dry with nitrogen at 500 rpm ❑ Dry wafer with nitrogen on clean texwipes		

	INSPECT LITHOGRAPHY:
	❑ Place wafer flat towards top of microscope
	❑ Inspect wafer alignment with yellow filter on microscope
	❑ Check Lithography : ❑ Open ❑ Clean ❑ Sharp Definition
	❑ Measure vernier alignment on edge reticles in center row (Left) Theta
	        (Right) X Alignment
	        (Right) Y Alignment
	❑ Rework wafer if alignment is off more than 0.6 µm
		Y_{Left} =
		X_{Right} =
		Y_{Right} =
		$\theta = Y_{Right} - Y_{Left}$ =	

	MEASURE STEP HEIGHT: ❑ Measure step height in three locations Mid: _____Top (flat):_____Bot:_____ Lt:_____ Rt:_____		
	INSPECT RESIST: ❑ Inspect photoresist under microscope (use yellow filter)		
	CONTACT METAL ETCH BACK: ❑ 1–2 min immersion etch in Technistrip (Etch until clear + 30 sec longer) ❑ **or** 30 sec immersion etch in Aqua Regus (Etch until clear) ❑ 3x DI bucket rinse ❑ Dry with nitrogen on clean Texwipes		
	INSPECT WAFER: ❑ Make sure seed layer is completely removed.		
	STRIP 1813: ❑ 20 sec acetone gun at 1000 rpm ❑ 20 sec acetone bottle at 500 rpm ❑ 20 sec Isopropanol rinse at 500 rpm ❑ 10 sec DI rinse at 500 rpm ❑ Dry with nitrogen at 500 rpm ❑ Dry wafer with Nitrogen on clean texwipes		
	INSPECT RESIST: ❑ Inspect photoresist for 1813 removal		
	MEASURE STEP HEIGHT: ❑ Measure contact metal step height in three locations Top _____ Middle _____ Bottom _____	**Finish Date** **Finish Time**	

Figure 84   SNM02 dimple etch back process follower (page 1/1).

154

Init.	Process Step	Notes	
	ASHER: ❏ 4 min, 200 W, 400 sccm O_2, LFE	**Start Date**	
	PRE-METAL DIP: ❏ 30 sec BOE : DI water (1:10) ❏ 3x bucket DI water rinse ❏ Dry wafer on clean texwipes with Nitrogen	**Start Time**	
	SEED LAYER DEPOSIT ❏ Sputter Au / Ti 700Å / 200Å		
	DEHYDRATION BAKE: ❏ 1 min 110℃ hot plate bake		
	9260 COAT ❏ Flood wafer with 9260 resist. Cut-off pipette at first indentation ❏ 30 sec spin @ 5000 rpm, Ramp=200 ❏ 2 min 110℃ hot plate bake ❏ Use acetone swab to remove 9260 on backside		
	EXPOSE 9260 TO BRIDGE MASK: ❏ Align to Bottom Metal alignment mark ❏ 15.0 sec Exposure, 0 Focus on stepper	**SNM02 \BR**	
	9260 DEVELOP: ❏ 3.0 min (210 sec) bucket develop in **fresh** AZ400k:DI (1:4) with <u>Hand Agitation</u> ❏ 3x bucket rinse ❏ Dry wafer with nitrogen on Texwipes		

	INSPECT LITHOGRAPHY:
	❏ Place wafer flat towards top of microscope
	❏ Inspect wafer alignment with yellow filter on microscope
	    ❏ Check Lithography : ❏ Open ❏ Clean ❏ Sharp Definition
	❏ Measure vernier alignment on edge reticles in center row (Left) Theta
	                        (Right) X Alignment
	                        (Right) Y Alignment
	
	❏ Rework wafer if alignment is off more than 0.6 µm
		Y_{Left} =
		X_{Right} =
		Y_{Right} =
		θ = Y_{Right} - Y_{Left}
		=	

	CLEAR PLATING CLIP AREA: ❏ Remove four small areas with acetone dampened swab for plating clips		
	1400-27 COAT BACKSIDE: ❏ Coat wafer backside with 1400-27 using large swab. ❏ Dry photoresist with Nitrogen to help coat edges		
	BACKSIDE RESIST BAKE: ❏ 1 min 90℃ Oven Bake (Wafer upside down in Fluo roware container)		
	ASHER: ❏ 4 min, 200 W, 400 sccm O_2, LFE		
	TITANIUM ETCH: ❏ 90 sec 1:10 BOE:DI (until clear) ❏ 10 sec DI bucket rinse ❏ 10 sec 1:10 BOE:DI ❏ 4X DI bucket rinse ❏ Dry with nitrogen on clean texwipes		
	INSPECT WAFER: ❏ Make sure Ti layer is completely removed.		
	MEASURE RESIST STEP HEIGHT: ❏ Measure step height and record in table		

Figure 85   SNM02 structural layer process follower (page 1/2).

	ELECTROPLATE STRUCTURAL LAYER: ❏ Power on the plating bath and wait for temp to rise ❏ Power on the Dynacomm controller and start the software ❏ Set current density (mA/cm^2), average current (mA), and Amin in software ❏ Load wafer and immerse into the plating bath solution ❏ _____ min plate time at at _____mA to give about ___ **μm** total thickness ❏ 2X DI bucket rinse ❏ Dry wafer with nitrogen on clean Texwipes ❏ Turn off plating system (if finished plating)				
	MEASURE STEP HEIGHT: ❏ Measure step height and record in table				
	REMOVE 9260 ❏ Remove 1400-27 from wafer backside with acetone soaked swap. Wipe thoroughly so all resist is removed. ❏ 30 sec spray with acetone bottle at 500 rpm ❏ 30 sec isopropyl alcohol at 500 rpm ❏ 10 sec DI bottle ❏ Dry with nitrogen at 500 rpm ❏ Dry wafer with nitrogen on clean Texwipes				
	INSPECT WAFER: ❏ Make sure resist is completely removed.				
	MEASURE STEP HEIGHT: ❏ Measure metal height and record in table ❏ Record result in plating log book				
	TITANIUM LAYER ETCH: ❏ 45–90 sec 1:10 BOE:DI (Etch until clear + 5-10 sec longer) ❏ 10 sec DI bucket rinse ❏ 10 sec 1:10 BOE:DI ❏ 3X DI bucket rinse ❏ Dry with nitrogen on clean Texwipes				
	INSPECT WAFER: ❏ Make sure Ti layer is completely removed.				
	SEED LAYER ETCH: ❏ Immerse in Technistrip (Etch until clear + 30 sec longer) ❏ 3x DI bucket rinse ❏ Dry with nitrogen on clean Texwipes				
	INSPECT WAFER: ❏ Make sure seed layer is completely removed.				
	MEASURE STEP HEIGHT: ❏ Measure metal height and record in table		**Finish Date** **Finish Time**		

ETCH TABLE	Center	Top	Bottom	Left	Right
PR Ht Before Plating					
PR Ht After Plating					
Au Ht After PR strip					
Au Ht After Seed Etch					
Au Ht After Alloy Etch					

Figure 86   SNM02 structural layer process follower (page 2/2).

Init.	Process Step	Notes
	REMOVE PMGI (Release): ❏ Place sample in room temp 1165, cover beaker with foil, place on hot plate. Set hot plate to 125°C (150 ml of 1165, 1000 ml beaker . 30 minute 1165 strip. ❏ Wet transfer from 1165 beaker to 1st IPA in Petri dish, 30 s soak ❏ Wet transfer to 2nd IPA in Petri dish, 30 s soak ❏ Wet transfer to 3rd IPA in Petri dish, 30 s soak ❏ Wet transfer to 4th IPA in Petri dish, 30 s soak ❏ Wet transfer to 1st methanol in Petri dish, 30 s soak ❏ Wet transfer to 2nd methanol in Petri dish, 30 s soak ❏ Wet transfer to 3rd methanol in Petri dish, 30 s soak ❏ Wet transfer to 4th methanol in Petri dish, 30 s soak ❏ Remove wafer from 4th methanol dish and place in CO2 dryer. Fill chamber with methanol to cover the wafer. Immediately cover CO2 dryer and start process.	**<u>Start Date</u>** **<u>Start Time</u>**
	❏ CO2 critical point dryer.	
	INSPECT WAFER:	
	ASHER: ❏ 4 min, 200W, 500 sccm, O$_2$, LFE	**<u>Finish Date</u>** **<u>Finish Time</u>**

Figure 87   SNM02 release process follower (page 1/1).

Bibliography

1. Abbot, E.J. and F.A. Firestone. "Specifying surface quantity - a method based on the accurate measurement and comparison," *ASME Mechanical Engineers*, *55*:569 (1933).

2. Adams, G.G. and M. Nosonovshy. "Contact Modeling - forces," *Tribology International*, *33*:431–442 (2000).

3. Agraït, Nicolás, Alfredo Levy Yehati, and Jan M. van Ruitenbeek. "Quantum properties of atomic-sized conductors," *Physics Reports*, *377*:81–279 (2003).

4. Ando, Yasuhisa and Jiro Ino. "Friction and pull-off forces on submicron-size asperities," *Wear*, *216*:115–122 (1998).

5. Anner, George E. *Planar Processing Primer*. New York: Van Nostrand Reinhold, 1990.

6. Attia, P., G. Tremblay, P. Laval, and P. Hesto. "Characterisation of a Low-Voltage Actuated Gold Microswitch," *Mat. Sci. and Eng.*, *B51*:263–266 (1998).

7. Barber, J.R. and M. Ciavarella. "Contact Mechanics," *Int. J. of Solids and Structures*, *37*:29–43 (2000).

8. Beale, John and Fabian R. Pease. "Apparatus for Studying Ultrasmall Contacts," *Proc. 38th IEEE Holm Conference on Electrical Contacts*, 45–49 (1992).

9. Beale, John and Fabian R. Pease. "Limits of High-Density, Low-Force Pressure Contacts," *IEEE Trans. of CPMT - Part A.*, *17*(2):257–262 (June 1994).

10. Becher, David, Richard Chan, Michael Hattendorf, and Milton Feng. "Reliabiltiy Study of Low-Voltage RF MEMS Switches," *Proc. GaAsMANTECH Conf.*, 03e (April 2002).

11. Bhushan, Bharat. "Contact Mechanics of Rough Surfaces in Tribology: Single Asperity Contact," *ASME*, *49*(5):275–298 (1996).

12. Bhushan, Bharat. "Contact Mechanics of Rough Surfaces in Tribology: Multiple Asperity Contact," *Tribology Letters*, *4*:1–35 (1998).

13. Bikulčius, G., T. Juodienė, and V. Šukienė. "Investigation of Wear of Alloys Based on Gold," *Surf. and Coat. Tech.*, *64*:149–154 (1994).

14. Bowick, Chris. *RF Circuit Design*. USA: Newnes - Elsevier Science, 1982.

15. Bridge, Technology www.four-point-probes.com/short.html, 2003.

16. Bromley, Susan C. and Braley J. Nelson. "Performance of Microcontacts Tested with a Novel MEMS Device," *Proc. 47th IEEE Holm Conference on Electrical Contacts*, 122–127 (2001).

17. Brown, Elliot R. "RF MEMS Switches for Reconfigurable Integrated Circuits," *IEEE Trans. on MTT*, *46*(11):1868–1880 (November 1998).

18. Burnham, N.A., A.J. Kulik, F. Oulevey, C. Mayencourt, E. Gourdon, E. Dupas, and G. Gremaud.

19. Butler, Jeffrey T. *Development and Packaging of Microsystems using Foundry Services*. Ph.D. Dissertation, Air Force Institute of Technology, WrightPatterson AFB, OH, 1998.

20. Cai, Yongming and Linda P.B. Katehi. "Series Switch Compatible with CMOS Technology," *Proc. IEEE MTT-S*, 1221–1224 (2002).

21. Calladine, C.R. *Plasticity for Engineers*. Chichester: Ellis Horwood Limited, 1985.

22. Chan, Richard, Robert Lesnick, David Becher, and Miton Feng. "Low-Actuation Voltage RF MEMS Shunt Switch with Cold Switching Lifetime of Seven Billion Cycles," *J. or MEMS*, *12*(5):713–719 (October 2003).

23. Chang, Chienliu and Peizen Chang. "Innovative micromachined microwave switch with very low insertion loss," *Sensors and Actuators A.*, *79*:71–75 (2000).

24. Chang, W.R. "An elastic-plastic model for a rough surface with an ion-plated soft metallic coating," *Journal of Wear*, *212*:229–237 (1997).

25. Chang, W.R., I. Etison, and D.B. Bogy. "An elastic-plastic model for the contact of rough surfaces," *ASME Journal of Tribology*, *109*:257–263 (1987).

26. Chen, Zhuan-Ke. "Wear and Contamination of Electroplated Gold Films in Line Contact," *IEEE Trans. on Comp., Hybrids, and Manufact. Tech.*, *15*(3):378–385 (1992).

27. Chial, Jung-Chih. "MEMS for High-Frequency Applications," *Proc. 8th Annual Int. Symp. on Smart Mat.*, 1–10 (March 2001).

28. Coutu, Jr. Ronald A. and Paul E. Kladitis. "Contact Force Models, Including Electric Contact Deformation, for Electrostatically Actuated, Cantilever-Style, RF MEMS Switches," *Proc. NSTI 2004 Nanotechnology Conference and Trade Show*, *2, 219-223* (March 2004).

29. Coutu, Jr. Ronald A., Paul E. Kladitis, Kevin D. Leedy, and Robert L. Crane. "Selecting Metal Alloy Electric Contact Materials for MEMS Switches," *J. of Micromech. and Microeng.*, *14*(8):1157–1164 (2004).

30. Coutu, Jr. Ronald A., Paul E. Kladitis, LaVern A. Starman, and Robert L. Crane. "RF MEMS Switches with Metal Alloy Electric Contacts," *Proc. 2004 Solid-State Sensor, Actuator, and Microsystems Workshop at Hilton Head*, 188–191 (June 2004).

31. Coutu, Jr. Ronald A., Paul E. Kladitis, LaVern A. Starman, and J. Robert Reid. "Finite Element Modeling and Simulation of Micro-Switch Pull-in Voltage and Contact Force," *Proc. Eurosensors XVII*, 64–67 (September 2003).

32. Coutu, Jr. Ronald A., Paul E. Kladitis, LaVern A. Starman, and J. Robert Reid. "A Comparison of Micro-Switch Analytic, Finite Element, and Experimental Results," *Sensors and Actuators A., Accepted on 17 March, 2004* (June 2004).

33. Coutu, Jr. Ronald A., Paul E. Kladitis, Rebecca Cortez, Richard E. Strawser, and Robert L. Crane. "Micro-Switches with Sputtered Au, AuPd,Au-on-AuPt, and AuPtCu Alloy Electric Contacts," *To be presented at the 50th IEEE Holm Conference on Electrical Contacts* (September 2004).

34. Coutu, Jr., Ronald A. "Modeling and Simulation of Classical Micro-Electro-Mechanical Systems (MEMS) Actuators," *AIAA Student Journal*, 46–54 (Spring 2002).

35. CoventorWare, Inc. "Analyzer Ref. Guide, Rev A.." www.coventor.com, 2001.

36. Cowan, William D. *Foundry Microfabrication of Deformable Mirrors for Adaptive Optics*. Ph.D. Dissertation, Air Force Institute of Technology, WrightPatterson AFB, OH, 1998.

37. Crinon, E. and J.T. Evans. "The effect of surface roughness, oxide film thickness, and interfacial sliding on the electrical contact resistance in aluminium," *Mat. Sci. and Eng. A, 242*:121–128 (1998).

38. De Los Santos, Héctor J. *Microwave and Mechanical Considerations in the Design of MEM Switches for Aerospace Applications, 3*. 1997.

39. De Los Santos, Héctor J. *RF MEMS Circuit Design for Wireless Communications*. Boston: Artech House, 2002.

40. Decuzzi, Paolo and David J. Scrolvitz. "Scaling Laws for Opening Partially Adhered Contacts in MEMS," *IEEE/ASME J. of MEMS, 13*(2):377–385 (April 2004).

41. DeNatale, Jeffrey and Robert Mihailovich. "RF MEMS Reliability," *Proc. Transducers '03 Conf.*, 943–946 (June 2003).

42. DeNatale, Jeffrey, Robert Mihailovich, and James Waldrop. "Techniques for Reliability Analysis of MEMS RF Switch," *Proc. 40th Annual Int. Rel. Phy. Symp.*, 116–117 (2002).

43. Dervos, Constantine T. and Joseph M. Michaelides. "The Effect of Contact Capacitance on Current-Voltage Characteristics of Stationary Metal Contacts," *IEEE Trans. on CPMT - Part A, 21*(4):530–540 (December 1998).

44. Duffy, Sean, Carl Bozler, Steven Rabe, Jeffrey Knecht, Lauren Travis, Peter Wyatt, Craig Keast, and Mark Gouker. "MEMS Microswitches for Recon-

figurable Microwave Circuitry," *IEEE Microwave and Wireless Components Letters*, *11*(3):106–108 (March 2001).

45. Dyck, Christopher W., Thomas A. Plut, Christopher D. Nordquist, Garth Kraus, Gary D. Schmidt, Karl Gass, Patrick S. Finnegan, Isak Reines, and Charles Sullivan. "A Compact MMIC-compatible RF MEMS Switch," *Proc. SPIE Conf.* (January 2003).

46. Ertl, S., M. Adamschick, P. Schmid, P. Gluche, A. Flöter, and E. Kohn. "Surface Micromachined Diamond Microswitch," *Diamond and Related Materials*, *9*:970–974 (2000).

47. Gad-el-Hak, Mohamed. *The MEMS Handbook*. Boca Raton: CRC Press, 2002.

48. Gho, C.-H., J.M. Wallace, R.W. New, and D.L. McDowell. "Polycrystal plasticity simulations of fretting fatigue," *International Journal of Fatigue*, *23*:S423–S435 (2001).

49. Grant, P.D., R.R. Mansour, and M.W. Denhoff. "A Comparison Between RF MEMS Switches and Semiconductor Switches," *Can. J. Elect. and Comput. Eng.*, *27*(1):1–9 (January 2002).

50. Greenwood, J.A. and J.H. Tripp. "The contact of two nominally flat rough surfaces," *Proc. Institute of Mechanical Engineers*, *185*:625–633 (1971).

51. Greenwood, J.A. and J.B.P. Williamson. "Contact of nominally flat surfaces," *Proc. Royal Soc. A.*, *295*:257–263 (1966).

52. Grètillat, M-A, F. Grètilla, and N.F. de Rooij. "Micromechanical Relay with Electrostatic and Metallic Contacts," *J. of Micromech. and Microeng.*, *9*:324–331 (1999).

53. Hacker, Jonathan B., Robert E. Mihailovich, Moonil Kim, and Jeffrey F. DeNatale. "A Ka-Band 3-Bit RF MEMS True-Time Delay Network," *IEEE Trans. on MTT.*, *51*(1):305–308 (January 2003).

54. Handbook, Committee. *Metals Handbook; Volume 2* (Tenth Edition). USA: ASM International, 1990.

55. Hiltmann, K., K. Keller, and W. Lang. "Micromachined Switches for Low Electric Loads," *Sensors and Actuators A.*, 117–121), (2001).

56. Hiltmann, Kai, Axel Schumacher, Kai Guttmanc Kai, Engelbert Lemp, Hermann Sandmaier, and Walter Lang. "New Micromachined Membrane Switches in Silicon Technology," *Proc. 47th IEEE Holm Conference on Electrical Contacts*, 117–121), (2001).

57. Hiltmann, Kai, Bertram Schmidt, Hermann Sandmaier, and Walter Lang. "Development of Micromachined Switches with Increased Reliability," *Proc. Transducers '97 Conf.*, 1157–1160), (June 1997).

58. Hinohara, K., K. Nakamura, T. Kobayashi, and T. Miyata. "Relationship Between Applied Voltage to Cause Discharge and Movement of Carriers for Rhodium-Plated Contact Reed Switches," *IEEE Trans. on CPMT - Part A*, *17*(1):58–60 (March 1994).

59. Holm, R. *Electric Contacts: Theory and Applications*. Berlin: Springer, 1969.

60. Hong-ming, Gu, Lu Miao, Zhou Xue-feng, Liang Chun-guang, and Gao Bao-xin. "Transient Response Characterization of Ohmic Contact RF MEMS Switches," *Proc. 3^d Int. Conf. on Microwave and Millimeter wave Tech. Rel. Phy. Symp.*, 271–274 (2002).

61. Hyman, D., A. Schmitz, B. Warneke, T.Y. Hsu, J. Lam, J. Brown, J. Schaffner, A. Walston, R.Y. Loo, G.L Tangonan, M. Mehregany, and J. Lee. "GaAs-Compatible Surface-Micromachined RF MEMS Switches," *Electronics Letters*, *35*(3):224–226 (1999).

62. Hyman, Daniel and Mehran Mehregany. "Contact Pysics of Gold Microcontacts for MEMS Switches," *IEEE Trans. on CPMT*, *22*(3):357–364 (September 1999).

63. Hyman, Daniel, Juan Lam, Brett Warneke, Adele Schmitz, T.Y. Hsu, Julia Brown, James Schaffner, Andy Walston, Robert Y. Loo, Mehran Mehregany, and Jae Lee. "Surface-Micromachined RF MEMS Switches on GaAs Substrates," *Int. J. RF and Microwave CAE*, *9*:348–361 (1999).

64. Jaeger, Richard C. *Introduction to Microelectronic Fabrication*. California: Addison-Wesley Publishing Company, 1993.

65. Jahn, Wilhelm. "Contact Materials for Reed Switches," *Proc. 36th IEEE Holm Conference on Electrical Contacts*, 53–58 (1990).

66. Jensen, Brian D., John L. Volakis, Kazuhiro Saitou, and Katsuo Kurabayashi. "Impact of Skin Effect on Thermal Behavior of RF MEMS Switches," *Proc. 6th ASME/JSME Therm. Eng. Joint Conf.*, 421–427 (March 2003).

67. Johnson, K.L. "Contact Mechanics and the Wear of Metals," *Wear*, *190*:162–170 (1995).

68. Kading, Glen A. *Micro-Electromechanical Switches for Micro-Satellite Power Transfer*. MS Thesis, Air Force Institute of Technology, WrightPatterson AFB, OH, 1997.

69. Kim, Hong-Teuk., Jae-Hyoung Park, Jounghwa Yim, Yong-Kweon Kim, and Youngwoo Kwon. "A Compact V-Band 2-bit Reflection-Type MEMS Phase Shifter," *IEEE Microwave and Wireless Compon. Lett.*, *11*(2):56–58 (February 2001).

70. Kim, M., J.B. Hacker, R.E. Mihailovich, and J.F. DeNatale. "A DC-to-40 GHz Four-Bit RF MEMS True-Time Delay Network," *IEEE Microwave and Wireless Compon. Lett.*, *11*(2):56–58 (February 2001).

71. Knapp, James A. and Maarten P. de Boer. "Mechanics of Microcantilever Beams Subject to Combined Electrostatic and Adhesive Forces," *IEEE/ASME J. of MEMS*, *11*(6):754–764 (December 2002).

72. Kogut, L. and I. Etison. "Elastic-Plastic Contact Analysis of a Sphere and a Rigid Flat," *J. of App. Mech.*, *69*:657–662 (2002).

73. Kogut, L. and I. Etison. "A Finite Element Based Elastic-Plastic Model for the Contact of Rough Surfaces," *Tribology Transactions*, *46*(3):383–390 (2003).

74. Kogut, L. and K. Komvopoulos. "Analysis of Interfacial Adhesion Based on Electrical Contact Resistance Measurements," *J. of Applied Phys.*, *94*(10):6386–6390 (November 2003).

75. Kogut, L. and K. Komvopoulos. "Electrical Contact Resistance Theory for Conductive Rough Surfaces," *J. of Applied Phys.*, *94*(5):3153–3162 (September 2003).

76. Kogut, L. and K. Komvopoulos. "Electrical Contact Resistance Theory for Conductive Rough Surfaces Separated by a Thin Insulating Film," *J. of Applied Phys.*, *95*(2):576–585 (January 2004).

77. Kogut, L. and K. Komvopoulos. "Electromechanically Induced Transistion from Nonohmic to Ohmic Behavior at Contact Interfaces," *Applied Phys. Lett.*, *84*(24):4842–4844 (November 2004).

78. Kogut, L., A. Lumbantobing, and K. Komvopoulos. "In-Situ Monitoring of Native Oxide Film Behavior at MEMS Contact Interfaces Through Basic Electrical Measurements," *Proc. 2004 Solid-State Sensor, Actuator, and Microsystems Workshop at Hilton Head*, 210–315 (June 2004).

79. Konchits, V.V. and C.K. Kim. "Electric current passage and interface heating," *Wear*, *232*:31–40 (1999).

80. Kovacs, Gregory T.A. *Micromachined Transducers Sourcebook*. New York: McGraw-Hill, 1998.

81. Kruglick, Ezekiel J.J. and Kristofer S.J. Pister. "Lateral MEMS Microcontact Considerations," *IEEE/ASME J. of MEMS*, *8*(3):264–271 (September 1999).

82. Kwiatkowski, Regina, Mihai Vladimirescu, André Zybura, and Savio Choi. "Scattering Parameter Model of Low Level Electrical Contacts in Electromechanical Microwave Switches - A Switch Manufacturers Approach," *Proc. 48th IEEE Holm Conference on Electrical Contacts*, 221–230 (2002).

83. Larsson, Joachim, Biwa Shiro, and Bertil Storåkers. "Inelastic flattening of rough surfaces," *Mechanics of Materials*, *31*:29–41 (1999).

84. Lavers, J.D. and R.S. Timsit. "Constriction Resistance at High Frequencies," *Proc. 47th IEEE Holm Conference on Electrical Contacts*, 167–174), (2001).

85. Lee, Han-Sheng, Chi H. Leung, Jenny Shi, and Shih-Chia Chang. "Electrostatically Actuated Copper-Blade Microrelays," *Sensors and Acutators A.*, *100*:105–113 (2002).

86. Lee, Han-Sheng, Chi H. Leung, Jenny Shi, Shih-Chia Chang, Samuel Lorincz, and Iulian Nedelescu. "Integrated Microrelays: Concepts and Initial Results," *IEEE/ASME J. of MEMS*, *11*(2):147–153 (April 2002).

87. Lee, J.J., C. Wuan, R. Allison, A. Reinehr, and B. Peirce. "Array Antennas Using Low Loss MEMS Phase Shifters," *Proc. Ant. and Prop. Soc. Int. Sym.*, *2*:14–17 (June 2002).

88. Li, Zhihong, Dacheng Zhang, Ting Li, Wei Wang, and Guoying Wu. "Bulk Micromachined Relay with Lateral Contact," *J. of Micromech. and Microeng.*, *10*:329–333 (2000).

89. Lindegurn, M.R., P.E. *Engineer-in-Training Reference Manual* (Eighth Edition). CA: Professional Publications, Inc., 1992.

90. Maciel, J., S. Majumder, R. Morrison, and J. Lamden. "Lifetime Characteristics of Ohmic MEMS RF Switches," *Proc. SPIE Conf.* (April 2004).

91. Madou, Mark J. *Fundamentals of Microfabrication* (Second Edition). Boca Raton: CRC Press, 2002.

92. Majumder, S., J. Lamden, R. Morrison, and J. Maciel. "MEMS Switches," *IEEE Instrumentation* & *Measurement Magazine*, 12–15 (March 2003).

93. Majumder, S., J. Lamden, R. Morrison, and J. Maciel. "A Packaged, High-Lifetime Ohmic MEMS RF Switch," *IEEE MTT-S*, 1935–1938 (April 2003).

94. Majumder, S., N.E. McGruer, and P.M. Zavracky. "Electrostatically actuated micromechanical switches," *J. Vac. Sci. Technol. A.*, *15*:1246–1249 (May/June 1997).

95. Majumder, S., N.E. McGruer, George G. Adams, P.M. Zavracky, Richard H. Morrison, and Jacqueline Krim. "Study of contacts in electrostatically actuated microswitch," *Sensors and Actuators A.*, *93*:19–26 (2001).

96. Majumder, Sumit, N.E. McGruer, Paul M. Zavracky, George G. Adams, Richard H. Morrison, and Jacqueline Krim. "Measurement and Modeling of Surface Micromachined, Electrostatically Actuated Microswitches," *IEEE Transducers '97*, 1145–1148 (June 1997).

97. Malucci, Robert D. "High Frequency Considerations for Multi-Point Contact Interfaces," *Proc. 47th IEEE Holm Conference on Electrical Contacts*, 175–185), (2001).

98. McCarthy, Brian, George G. Adams, Nicol E. McGruer, and David Potter. "A Dynamic Model, Including Contact Bounce, of an Electrostatically Actuated Microswitch," *IEEE/ASME J. of MEMS*, *11*(3):276–283 (June 2002).

99. McCool, J.I. "Predicting microfracture in ceramics via a microcontact model," *ASME Journal of Tribology*, *108*:380–386 (1986).

100. Meng, Qingyuan, Mehran Mehregany, and Robert L. Mullen. "Theoretical Modeling of Microfabricated Beams with Elastically Restrained Supports," *IEEE/ASME J. of MEMS*, *2*(3):128–137 (September 1993).

101. Mercado, Lei L., Shun-Meen Kuo, Lien-Yu T. Lee, and Lianjun Liu. "A Mechanical Approach to Overcome RF MEMS Switch Stiction Problems," *IEEE Elect. Compon. and Tech. Conf.*, 377–384 (2003).

102. MicroChem, Corp. www.microchem.com, 2003.

103. Mihailovich, R.E., M. Kim, J.B. Hacker, E.A. Sovero, J. Studer, J.A. Higgins, and J.F. DeNatale. "MEM Relay for Reconfigurable RF Circuits," *IEEE Microwave and Wireless Compon. Letters*, *11*(2):53–55 (February 2001).

104. Mikrajuddin, A., Frank G. Shi, H.K. Kim, and Kikuo Okuyama. "Size-dependent electrical constriction resistance for contacts of arbitrary size: from Sharvin to Holm limits," *Mat. Sci. in Semi. Proc.*, *2*:321–327 (1999).

105. Mozetic, M., M. Murko-Jezovsek, M. Bizjak, F. Brecelj, and K. Zupan. "Low Current Arc Characteristics of Au and W-Co Reed Switches," *Proc. 36th IEEE Holm Conference on Electrical Contacts*, 59–62 (1990).

106. Muldavin, Jeremy B. *Design and Analysis of Series and Shunt MEMS Switches*. Ph.D. Dissertation, University of Michigan, Ann Arbor, MI, 2001.

107. Muldavin, Jeremy B. and Gabriel M. Rebeiz. "All-Metal High-Isolation Series and Series/Shunt MEMS Switches," *IEEE Microwave and Wireless Compon. Lett.*, *11*(9):373–375 (September 2001).

108. Muldavin, Jeremy B. and Gabriel M. Rebeiz. "Inline Capacitive and DC-Contact MEMS Shunt Switches," *IEEE Microwave and Wireless Compon. Lett.*, *11*(8):334–336 (August 2001).

109. Newman, Harvey S. "RF MEMS Switches and Applications," *Proc. 40th Annual Int. Rel. Phy. Symp.*, 111–115 (April 2002).

110. Oberhammer, Joachim and Stemme Göran. "Low-Voltage High-Isolation DC-to-RF MEMS Switch Based on an S-shapted Film Actuator," *IEEE Trans. on Elec. Dev.*, *51*(1):149–154 (January 2004).

111. Oberhammer, Joachim, Björn Lindmark, and Göran Stemme. "RF Characterization of Low-Voltage High-Isolation MEMS Series Switch Based on an S-shaped Film Actuator," *Proc. SBMO/IEEE MTT-S IMOC*, 537–540 (September 2003).

112. Okamato, H., et al. *Binary Alloy Phase Diagrams* (Second Edition). Ohio: ASM International, 1992.

113. Osterber, Peter M. and Stephen M. Senturia. "M-Test: A Test Chip for MEMS Material Property Measurement Using Electrostatically Actuated Test Structures," *IEEE/ASME J. of MEMS*, *6*(2):107–118 (June 1997).

114. Ouyang, Q., R. Ishida, and K. Okada. "Investigation of Micro-Adhesion by Atomic Force Microscopy," *J. of App. Surf. Sci.*, *169*:644–648 (2001).

115. Peroulis, Dimitrios and Linda P.B. Katehi. "A Novel Device for In-Situ Experimental Characterization and Reliability Analysis of DC-Contact RF MEMS Switches," *Proc. Transducers '03*, 867–870 (June 2003).

116. Peroulis, Dimitrios, Sergio P. Pacheco, Kamal Sarabandi, and Linda P.B. Katehi. "Electromechanical Considerations in Developing Low-Voltage RF MEMS Switches," *IEEE Trans. on MTT*, *51*(1):259–270 (January 2003).

117. Peroulis, Dimitrios, Kamal Sarabandi, and Linda P.B. Katehi. "Low Contact Resistance Series MEMS Switches," *Proc. IEEE MTT-S*, 223–226 (2002).

118. Peterson, Kurt E. "Silicon as a Mechanical Material." *Proc. of the 1982 IEEE 70*. 420–457. Piscataway, NJ: IEEE Service Center.

119. Plötz, F., S. Michaelis, H.-J. Timme, J. Binder, and R. Noé. "Surface-micromachined electrostatic microrelay," *Sensors and Actuators A.*, *66*:345–354 (1998).

120. Pozar, David M. *Microwave Engineering* (Second Edition). New York: John Wiley & Sons, Inc., 1998.

121. Pozar, David M. *Microwave and RF Design of Wireless Systems*. New York: John Wiley & Sons, Inc., 2001.

122. Pruitt, Beth, L. and Thomas W. Kenny. "Piezoresistive cantilevers and measurement system for characterizing low force electrical contacts," *Sensors and Actuators A.*, *104*:68–77 (2003).

123. Rebeiz, Gabriel M. "RF MEMS Switches: Status of the Technology," *Proc. 12th Int. Conf. on Solid State Sensors, Actuators, and Microsystems - Transducers 2003*, 1726–1729 (June 2003).

124. Rebeiz, Gabriel M. *RF MEMS THEORY, DESIGN, AND TECHNOLOGY*. New Jersey: John Wiley & Sons, Inc., 2003.

125. Rebeiz, Gabriel M. and Jeremy B. Muldavin. "RF MEMS Switches and Switch Circuits," *IEEE Microwaves Magazine*, 59–71 (December 2001).

126. Rieder, Werner F. and Quido R. Salzmann. "A Two-Step Procedure to Evaluate Contact Compatibility of Organic Materials," *IEEE Trans. on CPMT - Part A.*, *19*(3):339–345 (September 1996).

127. Rizk, Jad B. and Gabriel M. Rebeiz. "Digital-Type RF MEMS Switched Capacitors," *Proc. IEEE MTT-S*, 1217–1220 (2002).

128. Rointan F. Bunshah, et al. *Deposition Technologies for films and coatings; Developments and Applications*. New Jersey: Noyes Publications, 1982.

129. Roth, S., C. Marxer, G. Feusier, and N.F. de Rooij. "One Mask Nickel Micro-Fabricated Reed Relay," *Proc. 13th Annual Internat. Conf. on MEMS 2000*, 176–179 (January 2000).

130. Sattler, R., P. Voigt, H. Pradel, and G. Wachutka. "Innovative Design and Modelling of a Micromechanical Relay with Electrostatic Actuation," *J. of Micromech. and Microeng.*, *11*:428–433 (2001).

131. Schaffner, James H., Adele E. Schmitz, Tsung-Yuan Hsu, David T. Chang, Robert Y. Loo, and Daniel F. Sievenpiper. "Metal Contact RF MEMS Switch Elements for Ultra Wideband RF Front-End Systems," *Proc. Ultra Wideband Sys. and Tech.*, 32–36 (November 2003).

132. Schauwecker, B., K.M. Strohm, T. Mack, W. Simon, and J.-F. Luy. "Serial Combination of Ohmic and Capacitive RF MEMS Switches for Large Broadband Applications," *IEEE Elect. Lett.*, *40*(1):44–46 (January 2004).

133. Schiele, Ignaz and Bernd Hillerich. "Comparison of Lateral and Vertical Switches for Applications as Microrelays," *J. of Micromech. and Microeng.*, *9*:146–150 (1999).

134. Schiele, Ignaz, Jörg Huber, Bernd Hillerìch, and Frank Kozlowski. "Surface-micromachined electrostatic microrelay," *Sensors and Actuators A.*, *66*:345–354 (1998).

135. Schimkat, J. "Contact Materials for Microrelays," *Proc. IEEE 11th Int. Workshop on MEMS*, 190–194 (1998).

136. Schimkat, J. "Contact Measurements Providing Basic Design Data for Microrelay Actuators," *Sensors and Actuators A.*, *73*:138–143 (1999).

137. Schroder, K. *CRC Handbook of Electrical Resistivities of Binary Metallic Alloys*. Florida: CRC Press, Inc., 1983.

138. Seki, T., S. Sato, T. Masuda, I. Mimura, and K. Imanaka. "Low-Loss RF MEMS Metal-to-Metal Contact Switch with CSP Structure," *Proc. 12th Int.*

Conf. on Solid State Sensors, Actuators, and Microsystems - Transducers 2003, 340–341 (June 2003).

139. Senturia, Stephen D. *Microsystem Design*. Boston: Kluwer Academic Publishers, 2001.

140. Serway, Raymond A. *Physics for Scientists and Engineers*. New York: Saunders College Publishing, 1986.

141. Sharvin, Y.V. *Sov. Phys. JETP*, *21*:655 (1965).

142. Shigley, Joseph Edward and Charles R. Mischke. *Mechanical Engineering Design* (Fifth Edition). New York: McGraw-Hill, Inc., 1990.

143. Simon, Jonathan, Scott Saffer, Sherman Faiz, and Chang-Jin Kim. "Lateral Polysilicon Microrelays with a Mercury Microdrop Contact," *IEEE Trans. on Indus. Elec.*, *45*(6):854–860 (December 1998).

144. Slade, P.G. *Electric Contacts: Principles and Applications*. New York: Marcel Dekker, Inc., 1999.

145. Stronge, W.J. *Impact Mechanics*. United Kingdom: Cambridge University Press, 2000.

146. Sun, M. and R. Martens. "A Kinetic Model For Noble Plated Electrical Contact Behavior," *Scripta Materialia*, *42*:1–8 (2000).

147. Sun, Ming, Michael G. Pecht, Marjorie Ann E. Natishan, and Rodney I. Martens. "Lifetime Resistance Model of Bare Metal Electrical Contacts," *IEEE Transactions on Advanced Packaging*, *22*(1):60–67 (February 1999).

148. Sze, S.M. *Semiconductor Devices; Physics and Technology*. New York: John Wiley & Sons, 1985.

149. Tan, Guan-Leng and Gabriel M. Rebeiz. "DC-26 GHz MEMS Series-Shunt Absorptive Switches," *IEEE Microwave and Wireless Compon. Lett.*, *12*(6):212–214 (June 2002).

150. Tan, Guan-Leng and Gabriel M. Rebeiz. "A DC-Contact MEMS Shunt Switch," *IEEE Microwave and Wireless Compon. Lett.*, *12*(6):212–214 (June 2002).

151. Tanner Research, Inc. www.tanner.com, 2003.

152. Tas, N.R., C. Gui, and M. Elwenspoek. "Static Friction in Elastic Adhesion MEMS Contacts," *J. of Adhesion Sci. and Tech.*, *17*(4):754–764 (May 2003).

153. Taylor, William P., Oliver Brand, and Mark G. Allen. "Fully Integrated Magnetically Actuated Micromachined Relays," *IEEE/ASME J. of MEMS*, *7*(2):181–191 (June 1997).

154. Thiel, Wener, Kelly Tornquist, Ron Reanotou, and Linda P.B. Katehi. "A Study of Thermal Effects in RF-MEMS-Switches using a Time Domain Approach," *Proc. MTT-S*, *1*:235–238 (June 2002).

155. Timoshenko, Stephen P. *Mechanics of Materials* (Fourth Edition). Boston,MA: PWS Publishing Company, 1990.

156. Timsit, R.S. "Course notes: Intensive Course on Electrical Connections for Electronics and Microelectronics Applications." Mar 2003.

157. Tringe, J.W., T.A. Uhlman, A.C. Oliver, and J.E. Houston. "A single aspertiy study of Au/Au electrical contacts," *J. of App. Phys.*, *93*(8):4661–4669 (April 2003).

158. Tsui, T.Y.,, C.A. Ross, and G.M. Pharr. "Nanoindentation Hardness of Soft Films on Hard Substrates: Effects of the Substrate," *Proc. of Mat. Res. Soc. Symp.*, *473*:57–62 (1997).

159. van Spengen, W. Merlijn, Robert Puers, and Ingrid De Wolf. "A Physical Model to Predict Stiction in MEMS," *J. of Micromech. and Microeng.*, *12*:702–713 (August 2002).

160. Varadan, Vijay K., K.J. Vinoy, and K.A. Jose. *RF MEMS and Their Applications*. England: John Wiley & Sons, Ltd., 2003.

161. Veijola, Timo, Taisto Tinttune, Hiekki Nieminen, Vladimir Ermolov, and Tapani Ryhänen. "Gas Damping Model for a RF MEMS Switch and Its Dynamic Characteristics," *Proc. IMS Conf.*, 1213–1216 (June 2002).

162. Vinci, R.P. and J.C. Bravman. "Mechanical Testing of Thin Films," *Proc. Transducers 1991*, 943–948 (1991).

163. Wang, Bor-Jenq, Nannaji Saka, and Ernest Rabinowicz. "The Failure Mechanism of Low-Voltage Electrical Relays," *Proc. 38th IEEE Holm Conference on Electrical Contacts*, 191–202 (1992).

164. Wang, Bor-Jenq, Nannaji Saka, and Ernest Rabinowicz. "Au-Sb and Au-Ag-Sb Alloys as Low-Voltage Contact Metals," *IEEE Trans. on CPMT - Part A*, *17*(2):295–302 (June 1994).

165. Wang, Ye, Zhihong Li, Daniel T. McCormick, and Norman C. Tien. "A Micro-machined RF Microrelay with Electrothermal Actuation," *Sensors and Actuators A.*, *103*:231–236 (2003).

166. Webster, Richard T., J. Robert Reid, and LaVern A. Starman. "RF MEMS Metal Contact Switch: Design, Measurement, and Modeling," *Proc. IEEE Wireless and Microwave Technology Conference (WAMI)* (April 2004).

167. Wexler, G. "The size effect and the non-local Boltzmann transport equation in orifice and disk geometry," *Proc. Phys. Soc.*, *89*:927 (1966).

168. Wood, Robert, Raaswamy Mahadevan, Vijay Dhuler, Bruce Dudley, Allen Cowen, Ed Hill, and Karen Markus. "MEMS Microrelays," *Mechatronics*, *8*:535–547 (1998).

169. Yan, Xiaomin, N.E. McGruer, G.G. Adams, and S. Majumder. "Finite Element Analysis of the Thermal Characteristics of MEMS Switches," *Proc. Transducers '03*, 412–415 (June 2003).

170. Yao, J. Jason. "Topical Review: RF MEMS from a Device Perspective," *J. of Micromech. and Microeng.*, *10*:9–38 (2000).

171. Yarborough, R.B., P.E. *Electrical Engineer Reference Manual* (Fifth Edition). CA: Professional Publications, Inc., 1990.

172. Zavracky, Paul M., Nicol E. McGruer, Richard H. Morrison, and David Potter. "Microswitches and Microrelays with a View Toward Microwave Applications," *Int. J. RF and Microwave CAE*, *9*:338–347 (1999).

173. Zavracky, Paul M., Sumit Majumder, and Nicol E. McGruer. "Micromechanical Switches Fabricated Using Nickel Surface Micromachining," *IEEE/ASME J. of MEMS*, *6*(1):3–9 (March 1997).

Vita

Major Ronald A. Coutu, Jr. enlisted in the Marine Corps in June 1984 as an RF-4B and F/A-18 avionics technician and was honorably discharged in October 1988. Major Coutu earned a bachelors degree in electrical engineering from the University of Massachusetts at Amherst and was commissioned through the Air Force ROTC program in May 1993. He was assigned to Vandenberg AFB, CA in September 1993. While at Vandenberg AFB, Major Coutu worked as an inter-continental ballistic missile test engineer and analyst for the Air Force Operational Test and Evaluation Center's Rapid Execution and Combat Targeting Test Team and as a missile test engineer for the Space and Missile System Center's Minuteman III Guidance Replacement Program. In addition, Major Coutu completed his masters degree in electrical engineering at the California Polytechnic (CalPoly) State University in San Luis Obispo and earned his professional engineer license. Following his assignment to Vandenberg AFB, Major Coutu was selected for the Air Force Test Pilot School's (TPS) experimental flight test engineer (FTE) course at Edwards AFB, CA. After completing TPS, he was assigned to the 416th Flight Test Squadron as an F-16 FTE where he worked as a foreign military sales project manager and as a section leader for USAF and European F-16 projects. While at Edwards AFB, Major Coutu completed Squadron Officers School (correspondence and in-residence), the USMC Amphibious Warfare School (correspondence), and earned an acquisitions level III certification in test and evaluation. In 2001, Major Coutu was selected for the Air Force Institute of Technology (AFIT) electrical engineering doctoral program where he studied microelectromechanical systems (MEMS) and stochastic modeling, estimation, and control. While at AFIT, Major Coutu completed Air Command and Staff College (correspondence) and was selected for the in-residence Intermediate Developmental Education (IDE) program. After completing the Ph.D. and IDE programs, Major Coutu will be assigned to the Air Force Research Laboratory.

REPORT DOCUMENTATION PAGE

Form Approved
OMB No. 074-0188

1. REPORT DATE *(DD-MM-YYYY)*	2. REPORT TYPE	3. DATES COVERED *(From – To)*
14-09-2004	**Doctoral Dissertation**	Sep 2001 – Sep 2004

4. TITLE AND SUBTITLE		5a. CONTRACT NUMBER
Electrostatic Radio Frequency (RF) Microelectromechanical Systems (MEMS) Switches with Metal Alloy Electric Contacts		5b. GRANT NUMBER
		5c. PROGRAM ELEMENT NUMBER
6. AUTHOR(S)		5d. PROJECT NUMBER QGWSML02722002
Coutu, Jr., Ronald A., Major, USAF		5e. TASK NUMBER
		5f. WORK UNIT NUMBER

7. PERFORMING ORGANIZATION NAMES(S) AND ADDRESS(S)	8. PERFORMING ORGANIZATION REPORT NUMBER
Air Force Institute of Technology Graduate School of Engineering and Management (AFIT/EN) 2950 Hobson Street, Building 642 WPAFB OH 45433-7765	AFIT/DS/ENG/04-05

9. SPONSORING/MONITORING AGENCY NAME(S) AND ADDRESS(ES)	10. SPONSOR/MONITOR'S ACRONYM(S)
Air Force Research Laboratory – Materials and Manufacturing Directorate (AFRL/MLB) Attn: Dr. Robert L. Crane 2941 Hobson Way. Suite I Wright Patterson AFB OH 45433 DSN: 785-9143	11. SPONSOR/MONITOR'S REPORT NUMBER(S)

12. DISTRIBUTION/AVAILABILITY STATEMENT

APPROVED FOR PUBLIC RELEASE; DISTRIBUTION UNLIMITED.

13. SUPPLEMENTARY NOTES

14. ABSTRACT

Radio frequency (RF) microelectromechanical systems (MEMS) switches are paramount in importance for improving current and enabling future USAF RF systems. Electrostatic micro-switches are ideal for RF applications because of their superior performance and low power consumption. The primary failure mechanisms for micro-switches with gold contacts are becoming stuck closed and increased contact resistance with increasing switch cycles.

This dissertation reports on the design, fabrication, and testing of micro-switches with sputtered bi-metallic (i.e., gold (Au)-on-Au-(6.3at%)platinum (Pt)), binary alloy (i.e., Au-(3.7at%)palladium (Pd) and Au-(6.3at%)Pt), and ternary alloy (i.e., Au-(5at%)Pt-(0.5at%)copper (Cu)) contact metals. Performance was evaluated, in-part, using measured contact resistance and lifetime results. The micro-switches with bi-metallic and binary alloy contacts exhibited contact resistance between 1 - 2 ohms and, when compared to micro-switches with sputtered gold contacts, showed an increase in lifetime. The micro-switches with tertiary alloy contacts showed contact resistance between 0.2-1.8 - and also showed increased lifetime. Overall, the results presented in this dissertation indicate that micro-switches with gold alloy electric contacts exhibit increased lifetimes in exchange for a small increase in contact resistance.

15. SUBJECT TERMS
Microelectromechanical Systems, Micro-switch, Electric Contacts, Alloys, Radio Frequency

16. SECURITY CLASSIFICATION OF:			17. LIMITATION OF ABSTRACT	18. NUMBER OF PAGES	19a. NAME OF RESPONSIBLE PERSON Paul E. Kladitis, Capt, USAF (ENG)
a. REPORT	b. ABSTRACT	c. THIS PAGE			19b. TELEPHONE NUMBER *(Include area code)* (937) 255-3636, ext 4595; e-mail: Paul.Kladitis@afit.edu
U	U	U	UU	197	

Standard Form 298 (Rev. 8-98)
Prescribed by ANSI Std. Z39-18